On ferroelectricity of magnets

Scaramucci, Andrea

rijksuniversiteit
groningen

On ferroelectricity of magnets

Proefschrift

ter verkrijging van het doctoraat in de
Wiskunde en Natuurwetenschappen
aan de Rijksuniversiteit Groningen
op gezag van de
Rector Magnificus, dr. F. Zwarts,
in het openbaar te verdedigen op
maandag 29 november 2010
om 11.00 uur

door

Andrea Scaramucci

geboren op 2 september 1980
te Urbino, Italië

Promotores	:	Prof. dr. M. Mostovoy Prof. dr. J. Knoester
Beoordelingscommissie	:	Prof. dr. N. Nagaosa Prof. dr. J. van den Brink Prof. dr. T. T. M. Palstra

University of Groningen
Zernike Institute
for Advanced Materials

Zernike Institute PhD thesis series 2010-19
ISSN 1570-1530
ISBN 978-90-367-4659-5 (printed version)
ISBN 978-90-367-4658-8 (electronic version)

The work presented in this thesis was performed in the research group Theory of Condensed Matter of the Zernike Institute for Advanced Material.

Cover design by Andrea Scaramucci.
Printed by Ipskamp Drukkers.

To the light that shines on my path

Contents

1 Introduction **1**
- 1.1 Magnetoelectric effect . . . 1
- 1.2 Multiferroics . . . 6
- 1.3 Breaking of inversion symmetry by magnetic ordering . . . 9
  - 1.3.1 Polarization induced by non-collinear magnetic order . . . 10
  - 1.3.2 Ferroelectricity induced by collinear orders . . . 11
- 1.4 Microscopic mechanisms . . . 12
  - 1.4.1 Magnetoelectric coupling in collinear magnets . . . 13
  - 1.4.2 Magnetoelectric coupling in spiral magnets . . . 14
- 1.5 Methods . . . 17
  - 1.5.1 A rigorous technique: the generalized Luttinger-Tizsa method . . . 17
  - 1.5.2 The Monte Carlo algorithm . . . 19
  - 1.5.3 Parallel tempering . . . 20
- 1.6 Outline . . . 21

2 Clamping of ferroelectric and ferromagnetic domain walls in conical spiral magnets **25**
- 2.1 Introduction: . . . 25
- 2.2 The model . . . 26
- 2.3 Phase diagram . . . 28
- 2.4 Structure of ferromagnetic domain walls in conical spirals . . . 29
- 2.5 Ferroelectric domain walls . . . 32
- 2.6 Concluding remarks . . . 33
- 2.A Appendix A: Conical spiral ground state . . . 34
- 2.B Appendix B: Isotropic phase diagram . . . 35
- 2.C Appendix C: Correction due to magnetocrystalline anisotropy to the circular spiral state . . . 36

2.D Appendix D: Domain walls in the strong $|J_F|$ limit . . . 37
2.E Appendix E: The $|S_\parallel| \ll 1$ limit . . . 38

3 Manipulating electric polarization by magnetic field in spiral magnets 43
3.1 Introduction . . . 43
3.2 Evolution of electric polarization in $ZnCr_2Se_4$ under magnetic field... . 45
3.2.1 Magnetic field in the spiral plane . . . 47
3.2.2 Magnetic field rotation . . . 48
3.3 Rotating electric polarization in $Eu_{0.55}Y_{0.45}MnO_3$ by rotating magnetic fields . . . 50
3.4 General rules of magnetic manipulation of electric polarization in spirals 53
3.5 Conclusions . . . 55
3.A Appendix A: Correction to the circular spiral state . . . 57

4 Microscopic theory of temperature-dependent magnetoelectric effect in Cr_2O_3 61
4.1 Introduction . . . 61
4.2 Microscopic model . . . 62
4.2.1 Magnetoelectric coupling . . . 63
4.2.2 Exchange Hamiltonian . . . 65
4.3 Mean-field calculation of $\alpha_\parallel(T)$ . . . 66
4.4 Monte Carlo calculation of $\alpha_\parallel(T)$ . . . 69
4.5 Conclusions and remarks . . . 71

5 High-Tc magnetoelectric effect in ferromagnetic thin films 75
5.1 Introduction . . . 75
5.2 Striped phase of ferromagnetic thin films . . . 77
5.3 Monte Carlo simulation . . . 81
5.3.1 The model . . . 81
5.3.2 Stripe domain phase in absence of electric field . . . 84
5.4 Polarization flip . . . 85
5.5 Conclusions . . . 86
5.A Appendix A: Magnetostatic interaction in ferromagnetic thin-films . . 88

6 Magnetic Polarons 93
6.1 Introduction . . . 93
6.2 Size and geometry of a single magnetic polaron . . . 95
6.3 Interaction between polarons . . . 98
6.4 Monte Carlo simulations . . . 100
6.5 Super-paramagnetism . . . 102
6.6 Comments and conclusions . . . 104
6.A Appendix A: Considerations on the shape of an isolated magnetic polaron . . . 105

7 Characterizing the low energy magnetic excitations of YMn_2O_5 109
7.1 Introduction . . . 109
7.2 Crystal and magnetic structure . . . 111
7.3 Spin model and magnetoelectric coupling . . . 112
7.4 Magnetic excitations . . . 114
7.4.1 Acoustic and optical low energy magnons . . . 116
7.4.2 Inelastic neutron scattering intensities . . . 117
7.5 Electromagnons . . . 118
7.6 Conclusions . . . 120
7.A Appendix A: Linearized equations of motion and generalized susceptibility . . . 121

8 Samenvatting 125

9 Acknowledgments 129

1

Introduction

This chapter introduces magnetoelectric and multiferroic phenomena. The origin of interactions between electron spins and polar lattice distortions in crystals is discussed from both microscopic and phenomenological points of view. In particular, the concepts of frustrated magnetism and the origin of periodically modulated magnetic orders are reviewed. Furthermore, some of the analytical and numerical techniques used to obtain the results of this study are explained. Finally, an outline of the following chapters is given.

Electric dipoles in insulating compounds are generated by displacements of positive and negative ions, while magnetic moments are induced by electron spins. Although at a first sight the origins of ferroelectricity and magnetism seem to be strikingly different, in principle, nothing prevents their mutual interactions. Indeed, the pioneering works of Landau, Lifshitz [1] and Dzyaloshinskii [2] (discussed in the next section) showed that from the phenomenological point of view such interactions may be allowed by symmetry. The microscopic origins of the magnetoelectric coupling involve physics of dielectrics with strongly correlated electrons. Thus, Mott insulators and, in particular, transition metals oxides offer a beautiful playground where a large number of effects resulting from this coupling have been observed during the past fifty years.

1.1 Magnetoelectric effect

By magnetoelectric effect one means the induction of static electric fields by applied static magnetic fields or *vice versa*. The possibility to observe such phenomena and,

after their observation in 1960, the challenge to find *strong* magnetoelectric effects interested many great physicists of the past and present century. The term "magnetoelectric" was coined by Peter Debye [3] in 1926, while the effect itself was conjectured by Pierre Curie [4] in 1894. Curie's idea followed the discovery by Röntgen (in 1888) that a dielectric moving in an electric field acquires a magnetization. Using symmetry arguments Curie argued that the same effect could happen intrinsically for non-moving crystals. More than half a century later Landau and Lifshitz [1] described briefly in one of the books of their famous series the symmetry requirements for a linear magnetoelectric effect.

Despite different origins of electric and magnetic dipoles, there is a formal equivalence of equations describing the behavior of polarizable media. The electric polarization **P** couples linearly to the applied electric field **E**, in the same way the magnetization **M** couples to the magnetic field **H**. Furthermore, equations of electrostatics and magnetostatics are identical if one replaces **E** by **H** and **P** by **M**. The only crucial difference is in the symmetries of **P** and **M**: electric polarization **P** together with the electric field **E** changes sign under space inversion transformation $\mathcal{I}$ and is invariant under time reversal $\mathcal{T}$, while the opposite holds for the magnetization **M** and the magnetic field **H** [see Table 1.1].

Consider the dependence of the free energy $F(\mathbf{E},\mathbf{H})$ of a dielectric in external magnetic and electric fields:

$$\begin{aligned} F(\mathbf{E},\mathbf{H}) = & - P_i^{(s)}E_i - H_iM_i^{(s)} - \frac{\chi_{ij}^{(E)}}{2}E_iE_j - \frac{\chi_{ij}^{(M)}}{2}H_iH_j \\ & - \alpha_{ij}E_iH_j - \frac{\beta_{ijk}}{2}E_iH_jH_k - \frac{\gamma_{ijk}}{2}E_iE_jH_k + \dots . \end{aligned} \tag{1.1}$$

where i,j,k label the spatial coordinates, $\chi_{ij}^{(E)}$ and $\chi_{ij}^{(M)}$ are respectively the electric and magnetic susceptibilities and the summation over repeated indexes is assumed[1]. The first two terms of Eq.(1.1) can be nonzero only in the so-called *primary ferroics* with a spontaneous polarization $\mathbf{P}^{(s)}$ and magnetization $\mathbf{M}^{(s)}$ [2]. These as well as the third and fourth terms do not involve any coupling between electric and magnetic field. The remaining three terms couple **H** and **E** and to fullfill the invariance of Eq.(1.1) under $\mathcal{I}$ and $\mathcal{T}$, the coupling constants α_{ij}, β_{ijk} and γ_{ijk} have to transform according to Table 1.1. This imposes strict symmetry requirements on states that give rise to magnetoelectric effects. For example, magnetoelectric effects originating from the last term in the r.h.s of Eq.(1.1) appear only in states that are odd under $\mathcal{T}$ and even under $\mathcal{I}$. Differentiating Eq.(1.1) with respect to the external fields and using $\beta_{ijk} = \beta_{ikj}$,

[1] We note that the terms $\eta_{ijkl}P_i^{(s)}M_j^{(s)}E_kH_l$ are also allowed by $\mathcal{I}$ and $\mathcal{T}$ symmetries. However they can be included in the term $\alpha_{ij}E_iH_j$.

[2] Primary ferroics include also ferroelastic materials displaying spontaneous strain and, according to Ref.[5], ferrotoroidics displaying spontaneous toroidal moment.

	E	**P**	**H**	**M**	**L**	α_{ij}	β_{ijk}	γ_{ijk}
$\mathcal{I}$	$-\mathbf{E}$	$-\mathbf{P}$	**H**	**M**	$\pm\mathbf{L}$[3]	$-\alpha_{ij}$	$-\beta_{ijk}$	γ_{ijk}
$\mathcal{T}$	**E**	**P**	$-\mathbf{H}$	$-\mathbf{M}$	$-\mathbf{L}$	$-\alpha_{ij}$	β_{ijk}	$-\gamma_{ijk}$

Table 1.1: Transformation of the fields and coupling constants discussed in the text under inversion $\mathcal{I}$ and time reversal $\mathcal{T}$. The vector **L** stands for an antiferromagnetic order parameter.

$\gamma_{ijk} = \gamma_{jik}$, we obtain:

$$P_i \equiv -\frac{\partial F(\mathbf{E},\mathbf{H})}{\partial E_i} = P_i^{(s)} + \chi_{(M)ij}E_j + \alpha_{ij}H_j + \frac{\beta_{ijk}}{2}H_jH_k + \gamma_{jik}E_jH_k \quad (1.2)$$

$$M_i \equiv -\frac{\partial F(\mathbf{E},\mathbf{H})}{\partial H_i} = M_i^{(s)} + \chi_{(M)ij}H_j + \alpha_{ji}E_j + \beta_{jik}E_jH_k + \frac{\gamma_{ijk}}{2}E_iE_j, \quad (1.3)$$

At low fields the main magnetic contribution to polarization (or vice versa) in Eqs.(1.2) and (1.3) comes from the magnetoelectric tensor α_{ij}. This tensor describes the induction of polarization by a magnetic field (or magnetization by an electric field) linear in the strength of the applied field. These phenomena are named *linear magnetoelectric effects*. Higher-order effects (described by the couplings β_{ijk} and γ_{ijk}) can play an important role only at relatively high fields or if $\alpha_{ij} = 0$.
As shown in Table 1.1, the magnetoelectric tensor is odd under $\mathcal{I}$ and $\mathcal{T}$. Therefore the linear magnetoelectric effect can only be observed in states where both time reversal and space inversion simmetries are broken. In particular, the requirement of spontaneous breaking of time reversal symmetry implies that a linear magnetoelectric effect only occurs in bodies with a long-range magnetic order. In 1960 Dzyaloshinskii [2] showed that the symmetries of the magnetically-ordered Cr_2O_3 allow for a nonzero magnetoelectric tensor α_{ij}. As a good example that what is not forbidden by symmetry tends to be welcome in nature, one year after the theoretical prediction Astrov measured the electric polarization induced by magnetic field in Cr_2O_3 below its magnetic transition temperature ($T_N = 307$ K) [6].
The crystallographic unit cell of Cr_2O_3 and the ordering of magnetic moments of Cr^{3+} ions below T_N are depicted in Fig. 1.1. The antiferromagnetic order parameter can be defined as $\mathbf{G} = \mathbf{M}_1 - \mathbf{M}_2 + \mathbf{M}_3 - \mathbf{M}_4$, where $\mathbf{M}_i$ ($i = 1, 2, 3, 4$) is the magnetic moment of the i-th Cr ion in the unit cell [see Fig. 1.1(b)]. The generators of the $R\bar{3}c$ space group describing the symmetry of the paramagnetic state are: the space inversion $\mathcal{I}$, the two-fold rotation around the x axis (2_x) at the points indicated in the picture and the three-fold rotation around the trigonal z axis (3_z) on which the Cr ions in the unit cell lie. In the antiferromagnetic state, where spins are oriented along z, 2_x and 3_z are preserved while inversion $\mathcal{I}$ and time reversal $\mathcal{T}$ are broken. Indeed, as shown in Fig. 1.1(b), the order parameter oriented along the z axis changes sign under inversion. Thus inversion symmetry is broken by magnetic ordering down to its composition with time reversal: $\mathcal{T}\mathcal{I}(G^z) = G^z$. Since G_z changes sign under

[3] The sign depends on the type of antiferromagnetic order parameter and on the transformation of the magnetic sublattices under inversion.

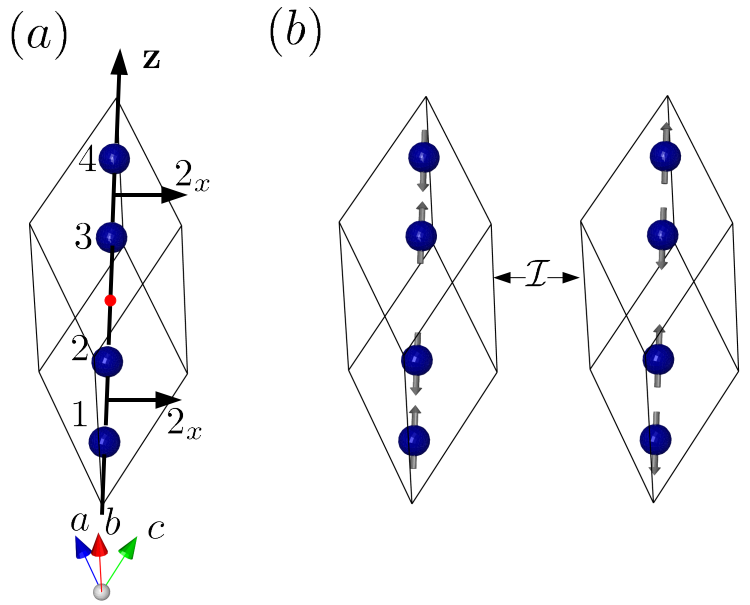

Figure 1.1: (a) Above the Neél temperature the rombohedral unit cell of Cr_2O_3 has a center of inversion (represented by the red dots at the center of the unit cell). In the magnetically ordered state inversion symmetry is lost: the two magnetic states (b) and (c) transform one into another under inversion. The trigonal axis is indicated by z. The arrows labeled by 2_x denote the axes relative to the two-fold rotation symmetry which are centered between the Cr ions 1 and 2 (or 3 and 4).

$\mathcal{T}$ and $\mathcal{I}$, magnetoelectric coupling terms of the form $g_i G_z H_i E_i$ are invariant under inversion and time reversal.

The transformation properties of the fields and the order parameter under the crystal symmetries are shown in Table 1.2. They impose further constraints on the form of the magnetoelectric coupling. The most general form bilinear in **E** and **H** and invariant under those transformations is [2]:

$$F_{me} = -g_{\parallel} G_z E_z H_z - g_{\perp} G_z (E_x H_x + E_y H_y). \tag{1.4}$$

Comparison with Eq.(1.1) gives the non-vanishing components of the magnetoelectric tensor: $\alpha_{zz} = -g_{\parallel} G_z$ and $\alpha_{xx} = \alpha_{yy} = -g_{\perp} G_z$.
This phenomenological description of the linear magnetoelectric effect in Cr_2O_3 does not allow to calculate the strength of these couplings. However, as shown in Chapter 4, an accuratate estimate of the coupling strength can be obtained from *ab initio* calculations.

The general excitement that followed Astrov's breakthrough experiment led to the search for other materials displaying linear magnetoelectric effect. In 1963 mag-

	2_x	3_z	$\mathcal{I}$	$\mathcal{T}$
G^z	1	1	-1	-1
$\mathbf{E}_\perp \equiv \begin{pmatrix} E^x \\ E^y \end{pmatrix}$	$\begin{pmatrix} 1 & 0 \\ 0 & -1 \end{pmatrix}$	$\mathcal{R}_z\left(\frac{2\pi}{3}\right)$	$\begin{pmatrix} -1 & 0 \\ 0 & -1 \end{pmatrix}$	$\begin{pmatrix} 1 & 0 \\ 0 & 1 \end{pmatrix}$
E^z	-1	1	-1	$+1$
$\mathbf{H}_\perp \equiv \begin{pmatrix} H^x \\ H^y \end{pmatrix}$	$\begin{pmatrix} 1 & 0 \\ 0 & -1 \end{pmatrix}$	$\mathcal{R}_z\left(\frac{2\pi}{3}\right)$	$\begin{pmatrix} 1 & 0 \\ 0 & 1 \end{pmatrix}$	$\begin{pmatrix} -1 & 0 \\ 0 & -1 \end{pmatrix}$
H^z	-1	1	1	-1

Table 1.2: Transformation of the order parameter, electric and magnetic field under the $R\bar{3}c$ symmetry group and $\mathcal{T}$. From the transformation properties it follows that the only invariants in the antiferromagnetic phase are $G_z E_z H_z$ and $G_z \mathbf{E}_\perp \cdot \mathbf{H}_\perp$.

netoelectric responses were measured in magnetic materials with composition and magnetic point group similar to those of Cr_2O_3. A magnetoelectric effect was observed in Ti_2O_3 by Al'shin *et al.* [7], while it was not found in V_2O_3 which has a somewhat different symmetry. In 1973, when the first MEIPIC-1 (Magnetoelectric Interaction Phenomena in Crystals) conference was organized, up to 80 magnetoelectric compounds were known [8].

The discussion of the linear magnetoelectric effect in Cr_2O_3 shows that the magnetic point group of a material restricts independent components of the magnetoelectric tensor. There are 58 point groups allowing for the appearance of a linear magnetoelectric effect, and the forms of the magnetoelectric tensor for each group are listed in Appendix A of Ref.[5] and in Fig. 3 of Ref.[9]. It is worth to notice that not all the point groups require the tensor α_{ij} to be symmetric under the exchange of the indexes i and j (as is the case for Cr_2O_3). An example is ferromagnetic $Ga_{2-x}Fe_xO_3$, where the point group $2'm'm$ allows for the magnetoelectric coupling, $F_{me} = \alpha_{yz} E_y H_z + \alpha_{zy} E_y H_z$. The magnetoelectric effect related to the first term was observed by Rado [10] in 1964. A similar coupling is also allowed for the nickel iodine boracide $Ni_3B_7O_{13}I$ [11].

The linear magnetoelectric effect is usually weak. In Cr_2O_3 the maximal value of α_{zz} is 4.13 ps m^{-1} ($\approx 10^{-4}$ in rationalized Gaussian units). For electric fields of 10^6 V cm^{-1} this would correspond to the flip of five spins on 10^4 magnetic ions in the antiferromagnetic lattice. Stronger couplings were found in phosphates: $TbPO_4$, $DyPO_4$ and $HoPO_4$, where the magnetic point group ($4'/m'm'm$) allows for the term $F_{me} = \alpha_{xx}(E_x H_x - E_y H_y)$. Among the phosphates, $TbPO_4$ has the strongest coupling: $\alpha_{xx} \approx 10^{-2}$ in Gaussian units. Other magnetoelectric materials are the orthoalluminates: $GdAlO_3$, $TbAlO_3$ and $DyAlO_3$ with magnetic point group ($m'm'm'$), which allows for a diagonal magnetoelectric tensor. At the present stage, the largest magnetoelectric effect has been measured on $DyFeO_3$, where the three two-fold symmetry axes in the magnetic point group allow, as in orthoalluminates, for the interaction, $F_{me} = \alpha_{xx} E_x H_x + \alpha_{yy} E_y H_y + \alpha_{zz} E_z H_z$, where $\alpha_{ii} \sim 2.4 \cdot 10^{-2}$ [12].

An upper bound on the magnitude of the linear magnetoelectric tensor, $\alpha_{ij}^2 < \frac{\epsilon_{ii}\mu_{jj}}{16\pi^2}$, comes from the stability requirement: free energy as a function of electric and magnetic fields must have a minimum at $\mathbf{E} = \mathbf{H} = 0$ (in absence of spontaneous polariza-

Type	Origin of **P**	Materials	Magnetic ordering	Coupling between **P** and magnetic order
Proper	Covalent bonding	$BaTiO_3$, PZT	No	No
	Lone Pair	$BiMnO_3$, $BiFeO_3$	Yes	No
Improper	Structural transition	h-$RMnO_3$	Yes	at domain walls
	Magnetic ordering	o-$RMnO_3$, $MnWO_4$	Yes	Weak

Table 1.3: Classification of ferroelectrics.

tion and magnetization) so that the Hessian matrix of Eq.(1.1) at $E = 0$ and $H = 0$ has positive eigenvalues. In fact, it was shown in [13] that if one neglects relatively weak diamagnetic response, a more severe restriction applies:

$$\alpha_{ij}^2 < \chi_{ii}^e \chi_{jj}^\mu. \tag{1.5}$$

According to Eq.(1.5), linear magnetoelectric effects are more likely to be large in materials that are close to a ferroelectric and/or ferromagnetic transition, which explains the interest in multiferroic materials discussed in the following section.
The bilinear magnetoelectric effects described by the tensors β and γ have a less important role in the playground of magnetoelectrics. The properties listed in Table 1.1 show that β can be nonzero in materials with no center of inversion. Effects related to the tensor β in Eq.(1.1) were first observed in the noncentrosymmetric paramagnetic crystal $NiSO_4 \cdot 6\ H_2O$ and were called paramagnetoelectric effects [14]. The tensor γ is nonzero in bodies were time reversal symmetry is broken by a magnetic order. Nonlinear magnetoelectric effects described by this tensor were observed in in ferrite garnets [15].

1.2 Multiferroics

Large magnetic and dielectric susceptibilities are found in materials with, respectively, ferromagnetic and ferroelectric order. As follows from Eq.(1.5), good candidates for materials with large magnetoelectric response are ferromagnetic ferroelectric compounds. Such systems represent a particular class of the so-called multiferroics materials, in which two (or more) *primary ferroic* orders coexist in the same phase [4]. However, the coexistence of a spontaneous **P** and **M** does not imply their cross-coupling. Indeed, as Eq.(1.5) gives only an upper limit to the magnetoelectric tensor, there are multiferroics where the magnetoelectric effect is very small or even entirely absent.
The current interest in multiferroics goes far beyond the pursuit of large magnetoelec-

[4]This definition, coined by Schmid [16], later has been extended to generic magnetic orders.

tric effects. The presence of both spontaneous magnetization and electric polarization potentially allows to make four-state memories [17], while the cross-coupling between **P** and magnetic orders can be used to write magnetic bits applying an external voltage (MERAM) instead of large currents (MRAM) [18]. In this way, the dissipation of energy in the writing process of magnetic memories can be drastically reduced.
Ferroelectrics can be divided in two main classes independently on whether they are magnetic or not: proper and improper. In *proper ferroelectric* the driving force of the transition is the structural instability associated with changes in the chemical bonding. Proper ferroelectrics have relativelly large polarization and very often their ferroelectric transitions occur above room temperature. However, they are usually non-magnetic. The reason for "Why there are so few magnetic (proper) ferroelectrics?" was clearly explained in Ref.[19] for the most widely known and used ferroelectric transition metal oxides with the perovskite structure. In these compounds the main driving force to polar distortion is the virtual hopping of electrons between the filled oxygen shell and the empty *d* shell of a transition metal. This explains why many perovskite ferroelectrics, as $BaTiO_3$ and $Pb(Zr_xTi_{1-x})O_3$ ($0 < x < 1$), contain ions with the d^0 electronic configuration (as Ti^{4+} or Zr^{4+}). Moreover, cations with nonzero *d* occupancies (d^1, d^2, d^4, d^5, d^6, d^7, d^9) are likely to favor non-polar Jahn-Teller distortion that might lower the tendency to an off-center displacement. Since magnetism requires a partial filling of the *d* shells of a transition metal, it is difficult to find magnetoelectric multiferroics among proper ferroelectrics.
However, there are some exceptions, such as $BiMnO_3$, $BiFeO_3$ and $PbVO_3$. In these compounds, called *lone pair* multiferroics, the major role in the appearance of ferroelectricity is played by the Bi^{3+} and Pb^{2+} ions, where two electrons occupy the 6*s* orbital, while the magnetic ordering is related to the ions with partially filled *d* orbitals. In these materials, the magnetic and ferroelectric transitions are well-separated ($T_{FE} = 800$ K and $T_{FM} = 110$ K, for $BiMnO_3$) and the interaction between the two orders is extremely weak.
On the other hand, in some materials a spontaneous electric polarization can appear as a "side effect" of another ordering. These compounds form the class of the so-called *improper ferroelectrics*. A good example is hexagonal manganites $RMnO_3$ (R=Ho-Lu,Y), where in the ferroelectric state the magnetic Mn ions remain at the center of the MnO_5 bi-pyramide and the spontaneous polarization appears due to the coupling of a polar mode to the buckling of the oxygen bipyramids. This was shown by van Aken *et al.* [20] for the case of $YMnO_3$. In the high-temperature paraelectric phase the crystal structure (symmetry group $P6_3/mmc$) consists of alternate non connected layers of corner-shared MnO_5 bipyramids separated by Y^{3+} ions lying on the *ab* planes. In the ferroelectric phase (symmetry group $P6_3cm$) the buckling of the MnO_5 blocks occurs due to the relatively small size of the Y^{3+} ions. Together with the buckling the Y^{3+} ions shift along the *c* axis in an alternate way, thus breaking the *ab* mirror plane symmetry. The shifts of the Y ions are such that the distance to the apical oxygens remains unchanged, while the lenght of the bonds with one of the in-plane oxygen is reduced or enlarged in an alternate fashion along the *c* axis. This collective distortion in which the long and short bonds alternate gives rise to a net polarization through the lattice anharmonicity. In such improper ferroelectrics, known as *geometric ferroelectrics*,

ferroelectricity can coexist with magnetic order although the electric polarization and magnetism are not necessarily coupled in the bulk. However, the domain imaging done in $YMnO_3$ by Fiebig *et al.* [21] using second harmonic generation technique, reveals that ferroelectric and antiferromagnetic domain walls are coupled in this material.

There are also improper ferroelectrics where electric polarization is induced by charge ordering. As discussed by Efremov *et al.* in Ref.[22] for $R_{1-x}Ca_xMnO_3$ (R=La,Pr), bond-centered and site-centered charge orderings can coexist in a certain range of doping concentration x. The resulting charge distribution is non-centrosymmetric and leads to a net polarization.

The best candidates for useful multiferroics are, arguably, improper ferroelectrics where ferroelectricity is induced by magnetic ordering. In those compounds, named magnetic ferroelectrics, the magnetic ordering (usually some complex antiferromagnetic ordering) breaks inversion symmetry and induces spontaneous polarization. Magnetic ferroelectrics can be further divided in two sub-classes depending on whether the spin ordering is collinear or not. Some non-collinear magnetic ferroelectrics are: orthorhombic rare earth manganites o-$RMnO_3$ (R=Tb,Dy), $MnWO_4$ and $CoCr_2O_4$, where the ferroelectric transition clearly correlates with the onset of a spiral spin ordering. The polarization in these compounds is rather small ($P \approx 10^2\ \mu C/m^2$), but it is extremely sensitive to an applied magnetic field. Indeed, the current revolution in the field of multiferroics started with the discovery of the high tuneability of dielectric constant by applied magnetic fields (Giant Magnetocapacitance) in $DyMnO_3$. There, an applied magnetic field causes a spin-flop transition [2], at which polarization changes direction and dielectric constant increases by 600%. One of the few collinear magnetic ferroelectrics discovered up to now is $Ca_3Co_{2-x}Mn_xO_6$ ($x \approx 0.96$) [24]. In this material inversion symmetry is broken by the onset of antiferromagnetic order of the type up-up-down-down ($\uparrow\uparrow\downarrow\downarrow$) in chains where two types of ions with different charges (Mn^{4+} and Co^{2+}) alternate. Although this compound displays a small polarization ($P \approx 90\ \mu C/m^2$), the mechanism inducing ferroelectricity (explained in the next section) allows for couplings between **P** and antiferromagnetism larger than the ones found in non-collinear magnets. It is worth to notice that although RMn_2O_5 (R=Tb, Dy, Y) display a non-collinear magnetic order, the approximate collinearity of spins allows for ferroelectricity induced by the same mechanism.

An important issue concerning magnetic ferroelectrics, is whether the spontaneous electric polarization in these materials can be reversed by applying magnetic fields. This phenomenon has been observed in the ferrimagnetic spiral compound $CoCr_2O_4$ [25; 26], where by reversing an applied magnetic field one can simultaneously change of **M** and **P**. The theoretical explanation of this phenomenon is based on the structure of magnetic domain walls in this compound is discussed in Chapter 2. The rotation of electric polarization by rotating magnetic field, which also has been observed [27; 28], is the topic of Chapter 3.

[2] As recently reported by Kagawa *et al.* in Ref.[23] Giant Magnetocapacitance in $DyMnO_3$ is due to the electric-field-driven motion of multiferroic domain walls.

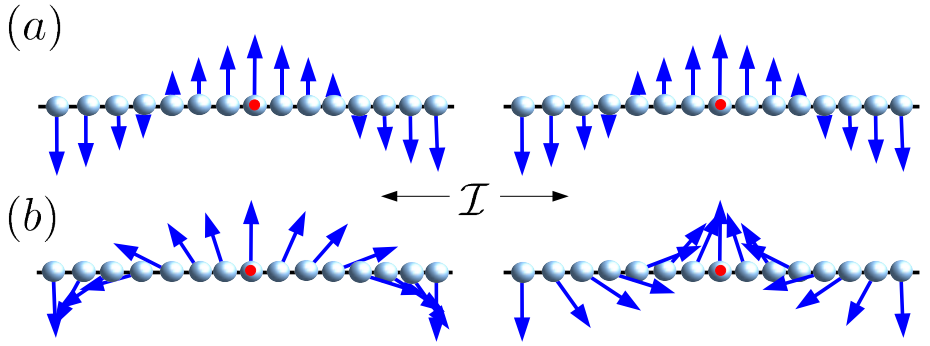

Figure 1.2: (a) The sinusoidal spin density wave state has a center of inversion (represented by the red point) and does not induce electric polarization. (b) A cycloidal spiral state is transformed by inversion into a spiral with an opposite direction of spin rotation.

1.3 Breaking of inversion symmetry by magnetic ordering

The beauty of Landau theory is that it can describe behavior of a system only using the knowledge of its symmetry properties. As we already mentioned, magnetic order can induce electric polarization only if it breaks inversion symmetry. In this section we discuss the form of phenomenological couplings between electric polarization and magnetic orders in magnetic ferroelectrics. We consider two examples: the first one concerns spiral states found in many frustrated magnets, while the second one pertains collinear magnetic states.

The coupling between the static spontaneous polarization **P** and the magnetic order parameter **L** can only contain even powers of **L**. This is due to the odd parity of magnetic order parameters under time reversal. On the other hand, the change of sign of **P** under inversion can be compensated by its product with another polar vector, e.g. gradient, with a function of **L** that changes sign[5] under $\mathcal{I}$. The observation that couplings linear in **P** are allowed in some magnetic compounds was crucial for understanding their multiferroic behavior [29; 30; 31]. Since the energy cost of polar lattice distortions is quadratic in P,

$$\Phi_E = \frac{P^2}{2\chi^{(E)}} + \dots, \tag{1.6}$$

arbitrarily small terms linear in **P** give rise to a polarization.

[5]It is worth to notice that the opposite does not hold. In the static regime spontaneous electric polarization does not break time-reversal. Thus linear couplings in **L** are not allowed.

	1	2	3	4
$\tilde{m}_x$	2	$1+\mathbf{b}$	4	$3+\mathbf{b}$
$\tilde{m}_y$	$4+\mathbf{a}$	**3**	$2+\mathbf{a}+\mathbf{c}$	$1+\mathbf{c}$
$\tilde{m}_z$	3	4	1	2

	$\tilde{m}_x$	$\tilde{m}_y$	m_z
$P_x(\partial_x)$	-1	1	1
$P_y(\partial_y)$	1	-1	1
$P_z(\partial_z)$	1	1	-1

	$\tilde{m}_x$	$\tilde{m}_y$	m_z
A_x	1	1	1
A_y	-1	-1	1
A_z	-1	1	-1

Table 1.4: Transformation of the four different Mn sites in the unit cell of $RMnO_3$ (upper panel), polar vectors (bottom left panel) and the magnetic order parameter (bottom right panel) under the generators of the symmetry group *Pbnm*.

1.3.1 Polarization induced by non-collinear magnetic order

Free energy terms linear in the gradient of an order parameter are called Lifshitz invariants. As pointed out in Refs.[29; 30], since the gradient transforms as a polar vector under inversion (see Table 1.1) terms of the kind $\Gamma_{\alpha,\beta,\varrho,\delta}P_\alpha M_\beta \partial_\varrho M_\delta$ [6] can be invariant under inversion. Such terms, are nonzero only if the magnetization $\mathbf{M}(\mathbf{r})$ varies in space. Being linear in $\mathbf{P}$ such terms induce polarization for arbitrarily weak couplings $\Gamma_{\alpha,\beta,\varrho,\delta}$. The structure of the tensor Γ is constrained by crystal symmetries. For cubic symmetry (see Ref.[30]) the Lifshitz invariant has the form:

$$\Phi_{ME} = \gamma P_\mu [M_\mu(\partial_\nu M_\nu) - M_\nu \partial_\nu M_\mu], \tag{1.7}$$

where γ is the strength of the coupling. For magnetic states, which have a center of inversion, such as a sinusoidal spin density wave [see Fig. 1.2(a)], the coupling Eq.(1.7) vanishes. The coupling is nonzero for the circular cycloidal spiral [see Fig. 1.2(b)], which breaks inversion symmetry, since the latter changes the direction of rotation of spins in the spiral. Minimizing the sum of Eq.(1.6) and Eq.(1.7) we find:

$$P_\mu = \frac{\gamma \chi_e}{V} \int d^3x [M_\mu(\partial_\nu M_\nu) - M_\nu \partial_\nu M_\mu], \tag{1.8}$$

where V is the system volume. A simple way to relate the average polarization to the magnetic order is given by the rule of thumb: $\mathbf{P} \propto \mathbf{e} \times \mathbf{Q}$, where $\mathbf{e}$ is the axis around which the magnetic moments rotate and $\mathbf{Q}$ is the wave vector of the spiral.

Similar Lifshitz invariants can be constructed for systems with more complex order parameters. Let us consider, for example, the case of o-$RMnO_3$, where the Mn_i ions labelled by the index $i = 1,2,3,4$ are located on the B sites of the perovskite structure [see Fig. 1.3]. The generators of the crystal symmetry group (*Pbnm*) are: $\tilde{m}_x, \tilde{m}_y, m_z$, where the x, y and z axes are shown in Fig. 1.3. Let us consider the case where the antiferromagnetic order parameter is $\mathbf{A} = \mathbf{S}_1 + \mathbf{S}_2 - \mathbf{S}_3 - \mathbf{S}_4$, $\mathbf{S}_i$ being the magnetic moment of the Mn ion at the site i. The sites of different magnetic sublattices, $\mathbf{P}$, ∇ and $\mathbf{A}$ transform under the generators of the symmetry group

[6] The summation over multiple indexes is assumed

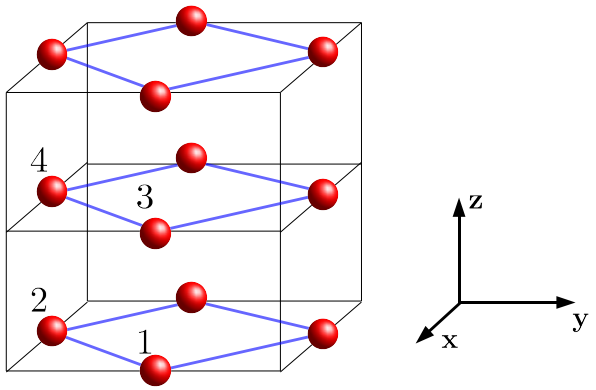

Figure 1.3: Positions of the Mn ions in orthorhombic $RMnO_3$. The numbers indicate the four ions in the unit cell.

according to Tab.1.4. Assuming that the order parameter varies along the y axis (as is the case for $RMnO_3$), the possible Lifshitz invariants terms are: $P_z A_z \partial_y A_y$, $P_z A_y \partial_y A_z$, $P_x A_x \partial_y A_y$ and $P_x A_y \partial_y A_x$. The sum $A_z \partial_y A_y + A_y \partial A_z$ is a total derivative and does not contribute to net polarization. Thus, the relevant interaction terms in the free energy couplings are:

$$\Phi_{ME} = \gamma_a P_z (A_z \partial_y A_y - A_y \partial_y A_z) + \gamma_c P_x (A_x \partial_y A_y - A_y \partial_y A_x). \tag{1.9}$$

In this case the crystal symmetries allow the magnetic order parameter to have different couplings with different directions of **P**. However, as in the previous case, only a cycloidal modulation of **A** induces ferroelectricity. In general, an helicoidal spiral cannot induce polarization if the system is symmetric under the two-fold rotation around an axis perpendicular to the wave vector. Indeed, the rotation around that axis, at the point where the magnetic order parameter is parallel to it, leaves the magnetic structure invariant, while under **P** is inverted.
It is worthwhile to notice that the same coupling can lead to the converse effect. In compounds where the inversion symmetry is broken by the onset of a ferroelectric state, the magnetic order parameter can become modulated in space due to the Lifshitz invariants. This happens, as pointed out by Kadomtseva *et al.* in Ref.[32], in the lone pair multiferroic $BiFeO_3$. This compound has a ferroelectric transition at $T_{FE} \approx 1100$ K, while antiferromagnetic order sets in below $T_N \approx 640$ K. The Lifshitz coupling of the magnetic order parameter **L** to the spontaneous polarization causes the spiral modulation of **L** with a large wavelength ($\lambda \approx 620$ Å). The large periodicity of such a spiral is indicative of the weakness of the coupling.

1.3.2 Ferroelectricity induced by collinear orders

A collinear magnetic ordering in Cr_2O_3 breaks inversion symmetry and gives rise to a linear magnetoelectric effect (see Sec. 1.1). In this section we consider collinear spin states that induce spontaneous electric polarization.

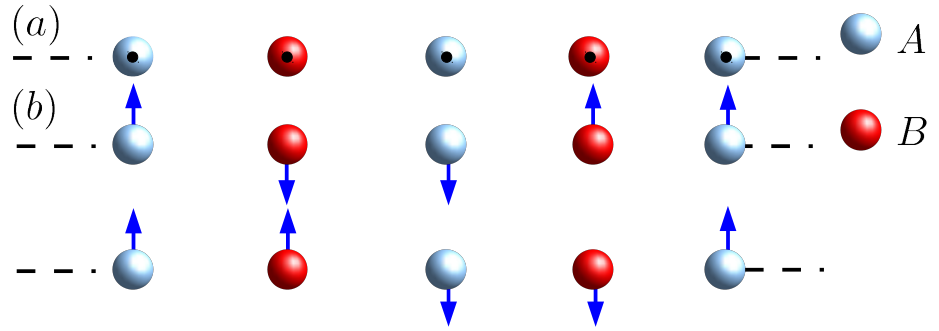

Figure 1.4: (a) A chain of A and B ions with different charges, which has a center of inversion on each site (represented by the black dots). The $(\uparrow\uparrow\downarrow\downarrow)$ antiferromagnetic order (here the spins are represented by blue arrows) breaks inversion symmetry and induces electric polarization. (b) Two of the four inequivalent states transforming into each other under inversion .

An example is shown in Fig. 1.4 [31]. Let us assume that the ions labelled by A and B are different and have different charges. Each ion in the paramagnetic phase Fig. 1.4(a) is a center of inversion. However, when a magnetic order of the type $\uparrow\uparrow\downarrow\downarrow$ sets in, inversion symmetry becomes broken (see Fig. 1.4(b)). Introducing the two-component order parameters $\mathbf{L}^{(1)} = \mathbf{S}_1 + \mathbf{S}_2 - \mathbf{S}_3 - \mathbf{S}_4$ and $\mathbf{L}^{(2)} = \mathbf{S}_1 - \mathbf{S}_2 - \mathbf{S}_3 + \mathbf{S}_4$ and assuming both vectors to be aligned along the z axes, we find that inversion transformation acts on these order parameters as:

$$\begin{pmatrix} L_z^{(1)} \\ L_z^{(2)} \end{pmatrix} = \begin{pmatrix} 0 & -1 \\ -1 & 0 \end{pmatrix} \begin{pmatrix} L_z^{(1)} \\ L_z^{(2)} \end{pmatrix}. \tag{1.10}$$

This implies that the coupling term $\Phi_{ME} = \gamma P_z \left[(L_z^{(1)})^2 - (L_z^{(2)})^2 \right]$ is invariant under both inversion and time reversal. By adding Eq.(1.6) to Φ_{ME} and minimizing:

$$P_z = \gamma \chi^{(E)} \left[\left(L_z^{(1)} \right)^2 - \left(L_z^{(2)} \right)^2 \right]. \tag{1.11}$$

Below Néel temperature the system chooses one of the four degenerate states: $L_1^z = \pm L$ or $L_2^z = \pm L$, which according to Eq.(1.11) induces a polarization $\pm\gamma\chi^{(E)}L^2$. This type of phenomenological coupling, discussed in Ref.[31] explains how magnetic ferroelectricity appears in the already mentioned $Ca_3Co_{2-x}Mn_xO_6$ ($x \approx 0.96$).

1.4 Microscopic mechanisms

In the previous section we obtained an expression of electric polarization induced by a cycloidal spin ordering and collinear magnetic states using symmetry arguments. Here, we discuss the microscopic mechanism responsible for the appearance of

magnetically-induced ferroelectricity and show that the polarization given by Eq.(1.8) is, in general, small compared to the polarization in multiferroics with collinear spin orders.

1.4.1 Magnetoelectric coupling in collinear magnets

The dominant interaction between spins in Mott insulators is the so-called Heisenberg exchange interaction, which has its origin in quantum statistics of electrons and the Coulomb interaction. The Hamiltonian describing this interaction has the form,

$$H = \sum_{<ij>} J_{i,j} \mathbf{S}_i \cdot \mathbf{S}_j \tag{1.12}$$

where $\mathbf{S}_i$ and $\mathbf{S}_j$ are spins at the lattice sites i and j. The main mechanism that generates the spin coupling in insulators is the so-called super-exchange. This type of exchange originates from the covalent mixing of d orbital states of two transition metal ions and the p states of a ligand ion located between them. The mixing of the d and p orbitals depends not only on their overlap but also on the relative orientation of the spins of the electrons of the transition metal ions. The super-exchange coupling constants J_{ij} are positive (corresponding to antiferromagnetic interaction) except for the case when the angle θ between lines connecting the magnetic ions ij with the ligand is close to 90°, in which case the exchange constant is negative (ferromagnetic interaction). The expansion of the coupling constant J in powers of the displacement $\mathbf{x}$ of two magnetic ions from their equilibrium positions: $J_x = J^0 + xJ' + \ldots$. contains terms linear in x. The elastic energy of the displacement, $\Delta x^2/2$, is quadratic in x. Thus considering only two magnetic ions (1 and 2), the displacement x minimizing the energy,

$$H = (J^0 + xJ')\mathbf{S}_1 \cdot \mathbf{S}_2 + \Delta \frac{x^2}{2}, \tag{1.13}$$

is non-zero, $x = -\frac{J'}{\Delta}(\mathbf{S_1} \cdot \mathbf{S}_2)$, and its sign depends on the sign of J' and on the relative orientations of $\mathbf{S}_1$ and $\mathbf{S}_2$. This phenomenon, called exchange striction, is the microscopic mechanism related to the phenomenological description of magnetoelectric coupling in collinear magnets [33]. It is worth to notice that this collective displacements can lead to a microscopic polarization only if inversion symmetry is broken. Consider the system described in the previous section and depicted in Fig.1.4. In the case of $J' < 0$, when an order of the type $\uparrow\uparrow\downarrow\downarrow$ sets in the exchange striction shortens the bond between parallel spins and stretches those between antiparallel spins giving rise to a net polarization.
Exchange striction mechanisms are also responsible for ferroelectricity in RMn_2O_5, where as it will be discussed in Chapter 7, three neighboring Mn ions with different charges (Mn^{3+}-Mn^{3+}-Mn^{4+}) show the approximately collinear ordering of the type $\uparrow\uparrow\downarrow$.

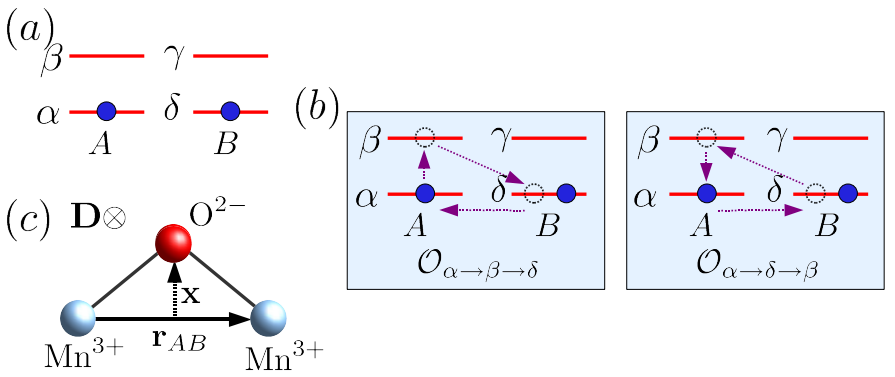

Figure 1.5: (a) Schematic representation of two electrons sitting in the orbital states α and γ of ion A and B. The orbital states β and δ represent the lowest excited state for respectivelly in ion A and B. (b) The processes giving the first order correction to superexchange due to the spin orbit coupling. (c) Sketch showing the orientation of the Dzyaloshinskii vector **D**.

1.4.2 Magnetoelectric coupling in spiral magnets

The Heisenberg exchange Eq.(1.12) is isotropic in the spin space, *i.e.*, it is invariant under an arbitrary rotation of all the spins by the same angle. One might argue that the symmetry that becomes broken spontaneously in magnets is then the rotational symmetry together with time reversal. This is not true: global rotations are not symmetries of the systems because spins interact with the crystal lattice that is not isotropic. All anisotropic interactions result from relativistic effects and, in particular, from the spin-orbit interaction,

$$H_{so} = \lambda \mathbf{l} \cdot \mathbf{S}, \tag{1.14}$$

where **S** is the spin operator of the electron, **l** is the angular momentum operator and $\lambda = \frac{e\hbar^2}{2m_e^2c^2r}\frac{\partial V}{\partial r}$ with $V(r)$ denoting the spherically symmetric ionic potential. Since the crystal field removes the rotational degeneracy of the orbitals, the interaction of the spin with the orbital momentum also removes the global rotational symmetry of the spin interactions giving rise to anisotropic terms. We consider now the first-order corrections due to the term Eq.(1.14) to the superexchange mechanism [34].
Let us consider the electron hopping process between the two sites depicted in Fig. 1.5(b). In the unperturbed state, the two electrons are in the lowest energy orbital states α and δ described, respectively, by the wave functions ψ_α (localized around site A) and ψ_δ (localized around site B). The higher-energy states β and γ are described by ψ_β (localized around site A) and ψ_γ (localized around site B) and they are empty. The first-order correction due to H_{so} mixes the orbital states in site A,

$$\psi^{(1)} = \psi_\alpha + \lambda\psi_\beta \frac{\mathbf{l}_{\alpha\beta}\cdot\mathbf{S}_A}{\epsilon_\beta - \epsilon_\alpha}, \tag{1.15}$$

where $\mathbf{l}_{\alpha\beta}$ is the matrix element of the angular momentum between the two orbital states, ϵ_i is the energy of the state i for the unperturbed Hamiltonian and $\mathbf{S}_A$, is the spin operator of the electron on the site A. Let us consider now the exchange process, where electron on the site A is first promoted to the level β and then is exchanged with the electron occupying site B. The operator describing this process is,

$$\mathcal{O}^A_{\alpha\to\beta\to\delta} = \lambda \mathcal{S}_{AB} \frac{t_{\alpha,\beta} t_{\beta,\delta}}{U} \frac{\mathbf{l}_{\alpha\beta} \cdot \mathbf{S}_A}{\epsilon_\beta - \epsilon_\alpha}, \tag{1.16}$$

where $\mathcal{S}_{AB}$ is the spin-exchange operator ($\mathcal{S}_{AB} = 1/2 + 2\mathbf{S}_A \cdot \mathbf{S}_B$) and $t_{\mu,\nu}$ are the amplitudes describing the hopping between the orbitals μ and ν. The operator describing the correction due to the process where the electron on the site A is first exchanged and then excited is:

$$\mathcal{O}^A_{\alpha\to\delta\to\beta} = \lambda \frac{\mathbf{l}_{\beta\alpha} \cdot \mathbf{S}_A}{\epsilon_\beta - \epsilon_\alpha} \mathcal{S}_{AB} \frac{t_{\beta,\alpha} t_{\delta,\beta}}{U}. \tag{1.17}$$

In absence of orbital degeneracy, the orbital part of the state of d electrons can always be chosen real. In that case the matrix elements $\mathbf{l}_{\alpha\beta}$ are purely imaginary and since $\mathbf{l}$ is an hermitian operator: $\mathbf{l}_{\beta\alpha} \equiv \mathbf{l}^*_{\alpha\beta} = -\mathbf{l}_{\alpha\beta}$. Using this relation, the sum of the contribution of $\mathcal{O}^A_{\alpha\to\beta\to\delta}$ and $\mathcal{O}^A_{\alpha\to\delta\to\beta}$ gives rise to the correction to the exchange Hamiltonian,

$$\delta H^{(1)A}_{ex} \propto \lambda [\mathcal{S}_{AB}, \mathbf{S}_A] \propto \lambda (\mathbf{S}_A \times \mathbf{S}_B) \cdot \mathbf{l}_{\alpha\beta}. \tag{1.18}$$

The correction to the exchange Hamiltonian coming from the analogous process involving the electron on site B gives: $\delta H^{(1)B}_{ex} \propto \lambda (\mathbf{S}_B \times \mathbf{S}_A) \mathbf{l}_{\delta\gamma}$. Therefore, the total correction can be written as,

$$\delta H^{(1)}_{ex} = (\mathbf{S}_A \times \mathbf{S}_B) \cdot \mathbf{D}_{AB}, \tag{1.19}$$

where $\mathbf{D}_{AB} \propto \lambda (\mathbf{l}_{\alpha\beta} - \mathbf{l}_{\delta\gamma})$ is the so-called Dzyaloshinskii vector. Thus the first-order correction to Heisenberg exchange due to the spin-orbit interaction is antisymmetric in spins. The symmetry properties of the vector $\mathbf{D}_{AB}$ are encoded in the so-called Moriya rules [34]. They can be summarized as follows: let $\mathbf{r}_{AB}$ be the vector connecting the site A to the site B and $\mathbf{x}$ to be the displacement of the ligand ion from the AB line [see Fig. 1.5 (c)]. Then,

$$\mathbf{D}_{AB} \propto \mathbf{x} \times \mathbf{r}_{AB}. \tag{1.20}$$

From Eq.(1.19) it is clear that the antisymmetric Dzyaloshinskii-Moriya interaction is only non-zero for non-collinear spin configurations.

Non-collinear magnetic orderings are usually present in magnetic systems where the geometry of the lattice or the exchange interactions are such that spins cannot minimize the exchange energy on each bond. Those systems are called frustrated magnets. A prototypical frustrated system is depicted in Fig. 1.6(a). It is a chain

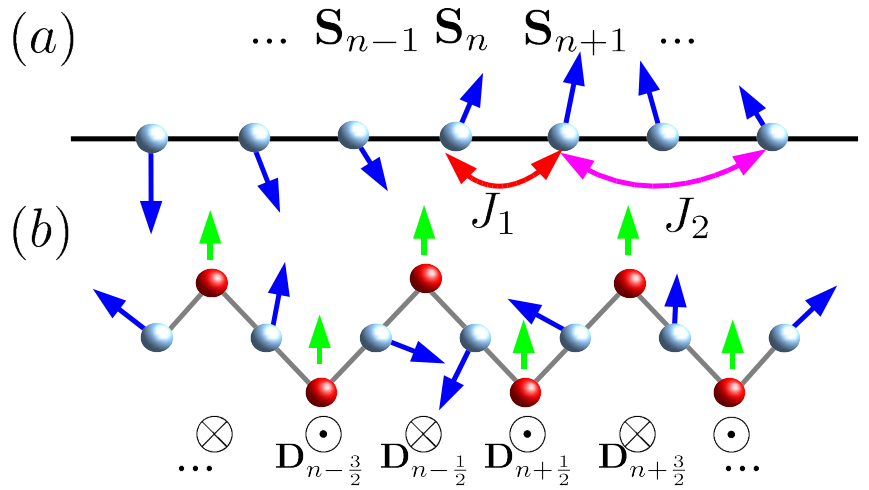

Figure 1.6: (a) The frustrated chain of classical spins. (b) The inset of cycloidal spin order favors the shift (green arrows) of the ligands ions by striction in the Dzyaloshinskii-Moriya exchange.

of classical spins $\mathbf{S}_i$ with ferromagnetic nearest-neighbor exchange $J_1 < 0$ and the antiferromagnetic next-nearest-neighbor exchange $J_2 > 0$,

$$H = \sum_{j=1}^{N} \left[J_1 \mathbf{S}_j \cdot \mathbf{S}_{j+1} + J_2 \mathbf{S}_j \cdot \mathbf{S}_{j+2} \right], \tag{1.21}$$

where N is the total number of spins. Defining $\mathbf{S}(q) = \sum_j \mathbf{S}_j \exp(2\pi q j/N)$, we can rewrite Eq.(1.21) in the form $H = N \sum_q \epsilon(q) |\mathbf{S}(q)|^2$, where $\epsilon(q) = J_1 \cos(q) + J_2 \cos(2q)$. The minimization of $\epsilon(q)$ with respect to q gives the minimal energy configuration:

$$\mathbf{S}_j = S \left[\cos(qj)\hat{\mathbf{e}}_1 + \sin(qj)\hat{\mathbf{e}}_2 \right], \quad \text{where} \quad \begin{cases} q = 0, & \text{if } |J_1| \geq 4J_2 \\ q = \arccos\left(\frac{|J_1|}{4J_2}\right), & \text{if } |J_1| < 4J_2 \end{cases} \tag{1.22}$$

and $\mathbf{e}_1$, $\mathbf{e}_2$ are two orthogonal unit vectors.
This mechanism explains the origin of the spiral magnetic ordering discussed in the previous sections. The microscopic origin of the electric polarization induced by the cycloidal spiral is the magnetostriction resulting from the Dzyaloshinskii-Moriya exchange interaction. In the cycloidal state the cross products $\mathbf{S}_j \times \mathbf{S}_{j+1}$ are oriented in the same direction for all pairs of neighboring spins. In the configuration shown in Fig. 1.6(b), they are alterately parallel and antiparallel to $\mathbf{D}_{i+\frac{1}{2}}$. Since the Dzyaloshinskii vector is linear in $\mathbf{x}$, while the elastic energy is quadratic, the onset of a cycloidal state energetically favors the displacement of the ligand ions in the same direction. This gives rise to ferroelectricity. The magnetostriction resulting from the Dzyaloshinskii-

Material	$T_{FE}(K)$	$T_M(K)$	$P(\mu C/m^2)$	Ref.
$TbMnO_3$	28	41	600	[35; 36; 37]
$Ni_3V_2O_8$	6.3	9.1	100	[38]
CuO	230	230	150	[39]
$MnWO_4$	8	13.5	60	[40; 41]
$CoCr_2O_4$	26	93	2	[25; 26]

Table 1.5: Ferroelectric and magnetic transition temperatures of some spiral (or conical spiral in the case of $CoCr_2O_4$) multiferroics and the value of the induced polarization. The magnetic transition temperature refers to the highest temperature magnetic transition while T_{FE} coincide with the setting in of the magnetic spiral order.

Moriya interaction is the microscopic mechanism behind the multiferroic behavior of a very large number of non-collinear magnets [see Table 1.5] and it correctly describes the appearance of ferroelectricity in materials with more complex magnetic structures, such as $CoCr_2O_4$ and $ZnCr_2Se_4$ in magnetic field, discussed in the later Chapters. However, as shown in Table 1.5, due to the relativistic nature of this interaction the strength of the magnetoelectric coupling is usually small compared to that resulting from the Heisenberg exchange interaction. The values of polarization induced by non-collinear magnetic ordering, shown in Table 1.5 for some materials, are very small compared to those of proper ferroelectrics ($P \sim 10 - 100\ \mu C/cm^2$).

1.5 Methods

After this short review of magnetic ferroelectrics, we discuss some analytical and numerical methods that will be used in the following chapters.

1.5.1 A rigorous technique: the generalized Luttinger-Tizsa method

The lowest-energy state of a frustrated spin system is often non trivial to find even if spins are treated as classical vectors. Consider a system of spins described by the quadratic Hamiltonian,

$$H = \sum_{\mu,\nu,j,k} J\left(\left|\mathbf{r}_{\mu,j} - \mathbf{r}_{\nu,k}\right|\right) \mathbf{S}_{\mu,j} \cdot \mathbf{S}_{\nu,k}, \tag{1.23}$$

where the Greek indexes label positions of spins in the unit cell and the Latin ones label the position of the unit cell. Due to the translational invariance, this quadratic form is diagonal in the Fourier space and the Hamiltonian can be written as,

$$H = \sum_{\mathbf{q}} J_{\mu\nu}(\mathbf{q}) \mathbf{S}^*_{\mu}(\mathbf{q}) \mathbf{S}_{\nu}(\mathbf{q}), \tag{1.24}$$

where $\mathbf{S}_\mu(\mathbf{q}) = \sum_j \mathbf{S}_\mu \exp(2i\pi/N\mathbf{q}\cdot\mathbf{r_j})$ and $\mathbf{J}_{\mu\nu}(\mathbf{q}) = \sum_j J(|\mathbf{r}_{\mu,j} - \mathbf{r}_{\mu,k}|)\exp(2i\pi/N\mathbf{q}\cdot(|\mathbf{r}_j - \mathbf{r}_k|))$. The minimization of such quadratic form is easy for unconstrained variables, but the spins have to fulfill the local constraints $|\mathbf{S}_{\mu,i}| = S_\mu$, which we will refer to as the *strong constraint*. Every local constraint in the coordinate space becomes non-local in the Fourier space, i.e. a function of all the variables $\mathbf{S}_\mu(\mathbf{q})$ has to be equal to S_μ. Thus, while on one hand, the transformation to the Fourier space simplifies the form of the interaction, on the other hand it increases the complexity of the constraints by making them non-local. As a result, the solution of the constrained minimization problem is generally impossible to obtain. However, as was noticed by Luttinger and Tisza [42] and then extended by Lyons and Kaplan in Refs. [43; 44], a set of configurations that minimize Eq.(1.23) often can be found using the weaker constraint:

$$\sum_{\mu,j} \alpha_\mu^2 \mathbf{S}_{\mu,j}\cdot\mathbf{S}_{\mu,j} = N\sum_{\mu,j}\alpha_\mu^2 S_\mu^2, \tag{1.25}$$

where α_μ are real constants. In general, it is not guaranteed that a configuration that minimizes Eq.(1.23) and fulfills Eq.(1.25) satisfies also the strong constraint. But if it is the case, than it is also a minimum for the original problem. Indeed, the set of configurations that respect the constraint Eq.(1.25) contains all configurations satisfying the strong constraint.
In the Fourier space Eq.(1.25) becomes: $\sum_{\mu,q}\alpha_\mu^2|\mathbf{S}_(q)|^2 = \sum_\mu \alpha_\mu^2 S_\mu^2$. Equations for the constrained minimization takes the form:

$$\sum_\mu J_{\mu\nu}(\mathbf{q})\mathbf{S}_\mu(\mathbf{q}) = \lambda\alpha_\nu^2\mathbf{S}_\nu(\mathbf{q}), \tag{1.26}$$

where λ is the Lagrange multiplier. After the transformation $T_\mu(\mathbf{q}) = \alpha_\nu S_\nu(\mathbf{q})$ and $W_{\mu,\nu}(\mathbf{q}) = J_{\mu,\nu}(\mathbf{q})/(\alpha_\mu\alpha_\nu)$, Eq.(1.26) reduces to the eigenvector equation for the matrix $W_{\mu,\nu}(\mathbf{q})$ with the eigenvalue λ: $W_{\mu,\nu}(\mathbf{q})T_\mu(q) = \lambda(q)T_\nu(q)$. We denote by $\lambda^-(\mathbf{q})$ the lowest egenvalue of such a matrix at the wave vector $\mathbf{q}$. The minimization problem reduces then to finding the minimum of $\lambda^-(\mathbf{q})$ and to constructing a solution satisfying Eq.(1.25) using the eigenvector.
Let the minimum of $\lambda(\mathbf{q})$ to be at the wave vector $\mathbf{q}'$ and the normalized eigevector corresponding to $\lambda^-(\mathbf{q}')$ to be $\mathbf{V}(\mathbf{q}')$. Finding the solution to the weak constraint reduces to finding complex constants A^i, where $i = x, y, z$, lables the spin components, which satisfy: $\sum_\mu\sum_i |A^i|^2 V_\mu^2 = \sum_\mu \alpha^2 S_\mu^2$. In that case the solution to the weak constraint is: $S_\mu^i(\mathbf{q}) = \delta(\mathbf{q}-\mathbf{q}')\frac{A^i V_\mu}{\alpha_\mu} + \delta(\mathbf{q}+\mathbf{q}')\frac{A^{*i}V_\mu}{\alpha_\mu}$.
A set of solutions of the original problem can be found, when by manipulating α_μ it is possible to find constants A^i satisfying the strong constraint. Here, the concept of "forced degeneracy" is often very useful. If for the values $\alpha_\mu = \alpha'_\mu$ it is possible to obtain two or more degenerate minima for $\lambda^-(q)$ (e.g. at $\mathbf{q}_1$ and $\mathbf{q}_2$), then the eigenvectors corresponding to these two minima (e.g. the eigenvectors $\mathbf{V}(\mathbf{q}_1), \mathbf{V}(\mathbf{q}_2)$) can be weighted with different constants (e.g. $A^i_{\mathbf{q}_1}$ and $A^i_{\mathbf{q}_2}$). This gives more degrees of freedom for constructing a state that satisfies the strong constraint.

1.5.2 The Monte Carlo algorithm

The Metropolis Monte Carlo algorithm is a very useful technique to calculate thermal averages. Consider a system of N spins and denote a general configuration by $\{\mathbf{S}\}$. For a given Hamiltonian $H(\{\mathbf{S}\})$ the thermal average of some quantity $A(\{\mathbf{S}\})$ is given by,

$$\langle A\rangle = \frac{\int d\{\mathbf{S}\}A(\{\mathbf{S}\})e^{-\beta H(\{\mathbf{S}\})}}{\int d\mathbf{S}e^{-\beta H(\mathbf{S})}} = \int d\{\mathbf{S}\}A(\{\mathbf{S}\})\omega(\{\mathbf{S}\}), \tag{1.27}$$

where $\int d\{\mathbf{S}\}$ denotes the integration over all the possible spin configurations and $\beta = (k_B T)^{-1}$. The Monte Carlo algorithm is used to calculate these averages by generating a Markov chain of configurations $\{\mathbf{S}\}_i$ that asymptotically reproduces the distribution $\omega(\{\mathbf{S}\})$. For this $\{\mathbf{S}\}_i$ has to satisfy two requirements: ergodicity and detailed balance. The ergodicity requirement states that all possible configurations have to be accessible starting with any possible configuration during the process of generation of the Markov chain. The detailed balance is a requirement for the convergence to the probability distribution $\omega(\{\mathbf{S}\})$ and states the following: in the generation of a new element of the Markov chain, for every two configurations $\{\mathbf{S}\}_A$ and $\{\mathbf{S}\}_B$, the ratio of the probability $p(\{\mathbf{S}\}_A \to \{\mathbf{S}\}_B)$ of going from the configuration $\{\mathbf{S}\}_A$ to the configuration $\{\mathbf{S}\}_B$ and the probability $p(\{\mathbf{S}\}_B \to \{\mathbf{S}\}_A)$ of the reverse process has to satisfy:

$$\frac{p(\{\mathbf{S}\}_A \to \{\mathbf{S}\}_B)}{p(\{\mathbf{S}\}_B \to \{\mathbf{S}\}_A)} = \frac{\omega(\{\mathbf{S}\}_B)}{\omega(\{\mathbf{S}\}_A)}. \tag{1.28}$$

A simple procedure that satisfies this requirement is given by the Metropolis algorithm where:

$$p(\{\mathbf{S}\}_A \to \{\mathbf{S}\}_B) = \min(1, \frac{\omega(\{\mathbf{S}\}_B)}{\omega(\{\mathbf{S}\}_A)}). \tag{1.29}$$

Since the frequency of the generated configuration reproduces asymptotically the probability distribution, the thermal average of a quantity $\langle A\rangle$ can be found by calculating its average value over the generated configurations. In other words, the Monte Carlo algorithm allows for visiting all points of the configuration space of a system with frequency proportional to their Boltzman weights.
In practice, the implementation of the Monte Carlo algorithm, presents difficulties both of fundamental and technical nature. The technical difficulties are related to the fact that only a limited number of configurations can be generated in a reasonable time, which can be overcome by using proper precautions in the sampling for the calculation of averages. For example, the thermalization times and sampling times must be longer than the time scale of correlations in the Markov chain (autocorrelation time) and the convergence of the averages has to be checked carefully. The fundamental difficulties are the finite size effects, which make it difficult to extract information about the system in the thermodynamic limit from simulations of relatively small lattices.

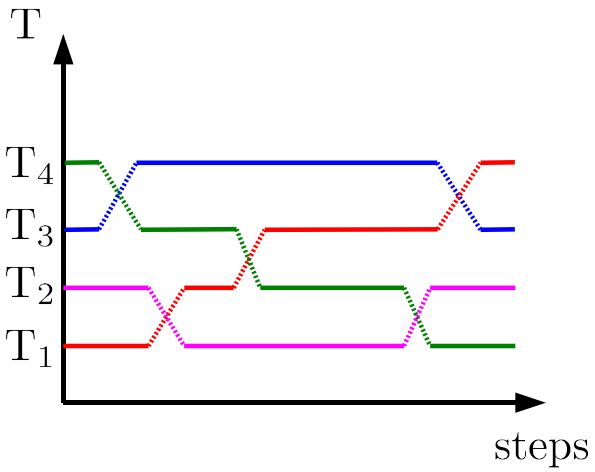

Figure 1.7: Pictorial view of the parallel tempering algorithm. Configuration (represented by different colours) evolving according to Monte Carlo algorithm at different temperatures can be exchanged with the acceptance ratio given by Eq.(1.30).

1.5.3 Parallel tempering

The parallel tempering, or replica exchange, is an extension of Monte Carlo algorithm that allows for a better sampling of the configuration space. Although the Monte Carlo algorithm is ergodic, real simulation at low temperatures often requires long times for overcoming barriers separating local minimima of energy. This problem is of particular relevance for the search of the ground state configuration of a frustrated system. The parallel tempering algorithm consist in performing simultaneous Monte Carlo simulations of systems at different temperatures T_j and allowing the configuration exchange between them.

Let us dentote with $\{\mathbf{S}\}_i^{T_j}$ the set of configurations generated by the Monte Carlo algorithm for the system at the temperature T_j. At a step k of the Monte Carlo procedure one exchanges configurations of the systems at temperature T_A and T_B with a probability:

$$P(\{\mathbf{S}\}_k^{T_A} \leftrightarrow \{\mathbf{S}\}_k^{T_B}) = \min(1, e^{(\beta_A-\beta_B)(H(\{\mathbf{S}\}_k^{T_B})-H(\{\mathbf{S}\}_k^{T_A}))}) \tag{1.30}$$

It is possible to show [45] that the detailed balance is satisfied for both systems. Figure 1.7 shows that this procedure can also be seen as an exchange in temperature keeping the configuration fixed. From this point of view, iteration of this exchange during the simulation allows a configuration to reach higher temperatures and tunnel through energy barriers. This makes it possible to simulate systems at very low temperatures. Keeping track of the lowest energy configuration visited by the system with the lowest temperature it is possible to find a good approximation for the ground state.

1.6 Outline

After this introduction to the magnetoelectric effect, to its microscopic origins and to some of the tools that will be used, we now summarize the content of the next chapters of this thesis.

In the following two chapters we study the magnetic manipulation of spontaneous electric polarization in magnetic ferroelectrics with spiral spin ordering. In Chapter 2 we show that the structure of ferromagnetic domain walls in conical spirals allows for the magnetic flip of electric polarization. There, we construct a simple spin model that, remarkably, has a phase with *conical spiral* spin ordering even in the absence of anisotropies. For such a model we first discuss the phase diagram and then we study the shape of a ferromagnetic domain wall. We show that in a large region of the conical spiral phase this type of domain wall also induce a wall between two domains with opposite electric polarization. In this region, the clamping between the two different type of domain walls allows for the magnetic control of the net electric polarization.

In Chapter 3 we discuss the conditions for the inversion of spontaneous electric polarization when a magnetic field is applied to a spin system with spiral magnetic order and then it is rotated. By studying the effect of the competition between Zeeman energy and magnetocrystalline anisotropy, we analyze the deformation from the spiral spin state when the magnetic field forms different angles with the crystallographic directions. Then we study the evolution of the electric polarization induced by the deformed spin ordering. Our study provides a simple theory explaining the magnetic switching of electric polarization in improper ferroelectrics with spiral spin order.

In the fourth chapter of this thesis we calculate the temperature dependence of the magnetoelectric susceptibility of the collinear antiferromagnet Cr_2O_3 [see sec. 1.1]. Using symmetry analysis, we obtain the microscopic exchange-striction coupling between spins and electric polarization. The strength of such a coupling and the value of exchange constants is evaluated by *ab initio* calculations. The magnetoelectric susceptibility of the resulting microscopic model is calculated by Monte Carlo simulations for various temperatures. Our results are in a very good agreement with the values observed experimentally and proves that the microscopic coupling behind the temperature-dependent magnetoelectric effect in collinear antiferromagnets has non-relativistic origin.

In Chapter 5 we propose a new route to magnetic-induced ferroelectric polarization at high temperature: the electric polarization induced by magnetic domain walls in the so-called “stripe domains” phase of ferromagnetic thin films. The presence of a Néel wall between two magnetic domains induces electric polarization. By performing Monte Carlo simulation on an effective spin model for a ferromagnetic thin film, we study patterns of electric polarization induced by these magnetic domain walls. We show that neighboring walls carry opposite electric polarizations. Moreover, we study the effect of an applied electric field on the electric polarization pattern finding that a rather high value of the field is necessary to flip it. However, we find that, at the flip transition, the dielectric constant of the film strongly increases.

Chapter 6 is slightly outside of the main argument of this thesis. In this chapter we study the effect of the insertion of Fe ions in the non-magnetic Ti sites of $FeTiO_3$.

The solid solution series of ilmenite and hematite, $(1-x)FeTiO_3$-xFe_2O_3, exhibit an unusual insulating ferromagnetic state appearing around room temperature. We show that Fe^{3+} dopants in the non magnetic Ti^{4+} layers induce large non-collinear modulations of spins in neighboring magnetic layers to which we refer as magnetic polarons. We study the features of these polarons, their interaction and their effect on magnetic properties. Polarons carry a large magnetic moment which leads to superparamagnetic response at low x. Furthermore, the long-range interaction between spin polarons suppresses the antiferromagnetic order of $FeTiO_3$ and leads to a ferromagnetic state at relatively low x.
In Chapter 7 we consider the non collinear magnetic state of YMn_2O_5 and we study its magnetic excitation. By using an appropriate spin Hamiltonian we classify the low energy magnetic modes, calculate their dispersion and their intensities for the inelastic neutron scattering. We relate quantitatively our results to the inelastic neutron scattering intensity scans observed experimentally. Furthermore, we identify the magnon which are strongly coupled to polar phonon (electromagnon) and relate their frequencies and spectral weight to the experimentally measured optical conductivity.

Bibliography

[1] Landau, L. and Lifshitz, E. *Electrodynamics Of Continuous Media*. Pergamon Press, (1984).

[2] Dzyaloshinskii, I. *Zh. Exp. Teor. Fiz.* **37**, 881 (1960).

[3] Debye, P. *Z. Phys.* **36**, 300 (1926).

[4] Curie, P. *J. Physique, 3ième série III* (1894). (Reprinted in (Euvres de Pierre Curie (Gauthier-Villars, Paris, 1908), pp. 118-141).

[5] Schmid, H. *Journal of Physics: Condensed Matter* **20**(43), 434201 (24pp) (2008).

[6] Astrov, D. *Zh. Exp. Teor. Fiz.* **38**, 984 (1959). [Soviet Phys. JETP **11**, 708 (1960)].

[7] Al'shin, B. and Astrov, D. *JETP* **17**(4), 809 (1963).

[8] Schmid, H. *Int. J. Magn.* **4**, 337 (1973).

[9] Rivera, J.-P. *Eur. Phys. J. B* **71**, 299 (2009).

[10] Rado, G. T. *Phys. Rev. Lett.* **13**(10), 335–337 Sep (1964).

[11] Ascher, E., Rieder, H., Schmid, H., and Stössel, H. *Journal of Applied Physics* **37**(3), 1404–1405 (1966).

[12] Tokunaga, Y., Iguchi, S., Arima, T., and Tokura, Y. *Phys. Rev. Lett.* **101**(9), 097205 Aug (2008).

[13] Brown, W. F., Hornreich, R. M., and Shtrikman, S. *Phys. Rev.* **168**(2), 574–577 Apr (1968).

[14] Hou, S. and Bloembergen, N. *Int. J. Magn.* **5**, 327–336 (1974).

[15] Mercier, M. *Int. J. Magn.* **6**, 77–88 (1974).

[16] Schmid, H. *Ferroelectrics* **162**, 317 (1994).

[17] Gajek, M., Bibes, M., Fusil, S., Bouzehouane, K., Fontcuberta, J., Barthelemy, A., and Fert, A. *Nat Mater* **6**(4), 296–302 (2007).

[18] Bibes, M. and Barthelemy, A. *Nat Mater* **7**(6), 425–426 (2008).

[19] Hill, N. A. *J. Phys. Chem. B* **104**, 6694–6709 (2000).

[20] Van Aken, B. B., Palstra, T. T., Filippetti, A., and Spaldin, N. A. *Nat Mater* **3**(3), 164–170 (2004).

[21] Fiebig, M., Lottermoser, T., Frohlich, D., Goltsev, A. V., and Pisarev, R. V. *Nature* **419**(6909), 818–820 (2002).

[22] Efremov, D. V., van den Brink, J., and Khomskii, D. I. *Nat Mater* **3**(12), 853–856 (2004).
[23] Kagawa, F., Mochizuki, M., Onose, Y., Murakawa, H., Kaneko, Y., Furukawa, N., and Tokura, Y. *Phys. Rev. Lett.* **102**(5), 057604 Feb (2009).
[24] Choi, Y. J., Yi, H. T., Lee, S., Huang, Q., Kiryukhin, V., and Cheong, S.-W. *Phys. Rev. Lett.* **100**(4), 047601 Jan (2008).
[25] Yamasaki, Y., Miyasaka, S., Kaneko, Y., He, J.-P., Arima, T., and Tokura, Y. *Phys. Rev. Lett.* **96**(20), 207204 May (2006).
[26] Choi, Y. J., Okamoto, J., Huang, D. J., Chao, K. S., Lin, H. J., Chen, C. T., van Veenendaal, M., Kaplan, T. A., and Cheong, S.-W. *Phys. Rev. Lett.* **102**(6), 067601 Feb (2009).
[27] Murakawa, H., Onose, Y., Ohgushi, K., Ishiwata, S., and Tokura, Y. *J. Phys. Soc. Jpn.* **77**(4), 043709 (2008).
[28] Murakawa, H., Onose, Y., Kagawa, F., Ishiwata, S., Kaneko, Y., and Tokura, Y. *Phys. Rev. Lett.* **101**(19), 197207 Nov (2008).
[29] Bary'achtar, V. G., L'vov, V. A., and Jablonskii, D. A. *JETP Lett* **37**.
[30] Mostovoy, M. *Phys. Rev. Lett.* **96**(6), 067601 Feb (2006).
[31] Cheong, S.-W. and Mostovoy, M. *Nat Mater* **6**(1), 13–20 (2007).
[32] Kadomtseva, A. M. *JETP Lett.* **79**, 571–581 (2004).
[33] Sergienko, I. A., Cengiz, Ş.., and Dagotto, E. *Phys. Rev. Lett.* **97**(22), 227204 Nov (2006).
[34] Moriya, T. *Phys. Rev.* **120**(1), 91–98 Oct (1960).
[35] Kimura, T., Goto, T., Shintani, H., Ishizaka, K., Arima, T., and Tokura, Y. *Nature* **426**(6962), 55–58 (2003).
[36] Abe, N., Taniguchi, K., Ohtani, S., Takenobu, T., Iwasa, Y., and Arima, T. *Phys. Rev. Lett.* **99**(22), 227206 Nov (2007).
[37] Kimura, T., Lawes, G., Goto, T., Tokura, Y., and Ramirez, A. P. *Phys. Rev. B* **71**(22), 224425 Jun (2005).
[38] Lawes, G., Harris, A. B., Kimura, T., Rogado, N., Cava, R. J., Aharony, A., Entin-Wohlman, O., Yildirim, T., Kenzelmann, M., Broholm, C., and Ramirez, A. P. *Phys. Rev. Lett.* **95**(8), 087205 Aug (2005).
[39] Kimura, T., Sekio, Y., Nakamura, H., Siegrist, T., and Ramirez, A. P. *Nat Mater* **7**(4), 291–294 (2008).
[40] Arkenbout, A. H., Palstra, T. T. M., Siegrist, T., and Kimura, T. *Phys. Rev. B* **74**(18), 184431 Nov (2006).
[41] Taniguchi, K., Abe, N., Takenobu, T., Iwasa, Y., and Arima, T. *Phys. Rev. Lett.* **97**(9), 097203 Aug (2006).
[42] Luttinger, J. M. and Tisza, L. *Phys. Rev.* **70**(11-12), 954–964 Dec (1946).
[43] Lyons, D. H. and Kaplan, T. A. *Phys. Rev.* **120**(5), 1580–1585 Dec (1960).
[44] Kaplan, T. and Menyuk, M. *Phil. Mag.* **87**, 3711 (2007).
[45] Earl, D. and Deem, M. *Phys. Chem. Chem. Phys.* **7**, 3910 (2005).

2

Clamping of ferroelectric and ferromagnetic domain walls in conical spiral magnets[1]

In this chapter we discuss the structure of domain walls in magnetic ferroelectrics with the conical spiral spin order and its relevance to magnetoelectric switching phenomena. We first introduce a simple spin model and prove that its ground state is a conical spiral for a wide range of coupling constants. Then, we discuss the structure of ferromagnetic end ferroelectric domain walls and the interaction between the two. We show that this interaction plays a crucial role in the observed magnetic reversal of electric polarization in $CoCr_2O_4$.

2.1 Introduction:

One of the practical motivations to study magnetoelectric multiferroics is the search for ways to control magnetic patterns by an applied voltage and to manipulate electric polarization by magnetic field. The magnetically-induced flip of electric polarization was first observed in nickel boracide [1], where the coexistence of a ferroelectric state with an antiferromagnetic ordering exhibiting a linear magnetoelectric effect gives rise to the magnetization, **M**, linearly coupled to the spontaneous electric polarization, **P** [2]. More recently, Kimura *et al.* [3] observed the magnetic field-induced 90°-rotation of electric polarization in rare earth manganites with a spiral magnetic ordering (see Chapter 3 for detailed discussion). There, an applied magnetic field results in the

[1]This chapter is based on A.Scaramucci, T.A. Kaplan, M. Mostovoy, arXiv:0906.5298.

90°-flop of the cycloidal spiral plane with a concomitant rotation of **P**. The giant peak in dielectric constant of $DyMnO_3$ observed at the polarization flop transition [4] was recently related to the motion of the 90° multiferroic domain walls in ac electric field [5]. The magnetically-induced polarization flip was also observed in $HoMn_2O_5$, which in an applied magnetic field toggles between two different multiferroic phases with opposite orientations of **P** [6].
Similar polarization reversals were recently found in the $CoCr_2O_4$ spinel, which shows a ferrimagnetic conical spiral ordering and is both ferroelectric and ferrimagnetic [7; 8]. In the conical spiral ordering spins have a uniform component $\mathbf{S}_{\parallel}$ and a spiral component $\mathbf{S}_{\perp}$. Since the rotation direction of the spins is independent of the uniform component of magnetic ordering, **M** and **P** are not coupled. This makes the observed polarization flips in $CoCr_2O_4$, at least, unexpected. The magnetization and polarization in this material are induced by two different magnetic transitions: the magnetization appears below 95 K as a result of the collinear ferrimagnetic ordering of Co and Cr spins, while the electric polarization is induced by the spiral spin ordering that sets in at 27 K. The interaction between the uniform and spiral components of the conical spiral favors the spiral plane (and hence the induced **P**) orthogonal to **M**, but it cannot constrain the direction of rotation of spins in the spiral (sometimes called chirality or handedness), which determines the sign of **P**. For a given **M**, the spiral states with opposite handedness and opposite polarizations are degenerate and both can be stabilized by electric field cooling [7; 8].
In Ref. [7] it was suggested that the coupling between the magnetization and polarization in $CoCr_2O_4$ occurs at domain walls, where **M** and **P** change sign simultaneously. The coexisting ferrimagnetic and spiral orders imply the existence of at least two types of domain walls: the ferromagnetic domain wall separating domains with opposite magnetization and the chiral or handed domain wall where the direction of spin rotation and the induced electric polarization changes sign. The polarization reversals in $CoCr_2O_4$ can be explained by clamping of ferromagnetic and chiral (ferroelectric) domain walls. In this Chapter we study the structure of domain walls in conical spiral magnets and the clamping of ferromagnetic (FM) and ferroelectric (FE) domain walls.

2.2 The model

The straightforward numerical simulation of the domain walls in spinels is impossible, as the domain wall width w is large compared to the period of the spiral l. Since maintaining the relations, $a \ll l \ll w \ll L$, where a is the distance between neighboring spins and L is the system size, is crucial for studying the clamping of the FM and FE domain walls, we devised a simple model of the conical spiral state, which is amenable to numerical simulations. To our knowledge, this is the first simple and rigorously soluble model where a conical spiral is stabilized without magnetic anisotropy. The first model where this physics was found, but only variationally, is the cubic spinel with nearest-neighbor AB and BB interactions, a complex structure with 6 coupled conical spirals [9], which incidentally, has provided the basis for understanding the observed behavior of several chromites [10; 9; 7; 8].
The model consists of two coupled chains of classical spins [see Fig. 2.1]: one with the

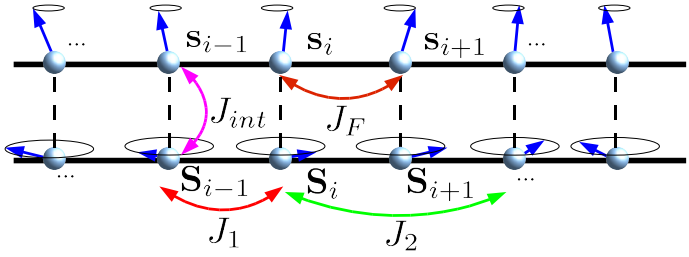

Figure 2.1: The system of coupled ferromagnetic and frustrated chains that shows a conical spiral ground state.

FM coupling, $J_F < 0$, between neighboring spins and another with the competing FM nearest-neighbor interaction, $J_1 < 0$ and the antiferromagnetic next-nearest-neighbor interaction, $J_2 > 0$. As was shown in Sec. 1.4.2, for $\frac{J_2}{|J_1|} > \frac{1}{4}$, the minimal energy state of the frustrated chain is a simple (flat) spiral with the wave vector $Q = \arccos \frac{|J_1|}{4J_2}$. The Hamiltonian of the model is

$$H = \sum_{n=1}^{L} \; [\; J_F \mathbf{s}_n \cdot \mathbf{s}_{n+1} + J_1 \mathbf{S}_n \cdot \mathbf{S}_{n+1} + J_2 \mathbf{S}_n \cdot \mathbf{S}_{n+2} \\ + \; J_{\text{int}} \mathbf{s}_n \cdot \mathbf{S}_n], \tag{2.1}$$

where $\mathbf{s}_i$ and $\mathbf{S}_i$ are spins in, respectively, the "ferromagnetic" and "spiral" chain, the spins being unit vectors. When a weak interchain coupling J_{int} between the two chains is turned on, the "ferromagnetic" chain acquires a small spiral component, while spins in the "spiral" chain rotate in the plane orthogonal to the magnetization vector in the "ferromagnetic" chain with a small canting in the magnetization direction. Infact, such a conical spiral state,

$$\begin{cases} \mathbf{s}_n &= s_\perp \left[\cos(Qn+\phi)\mathbf{e}_1 + \sin(Qn+\phi)\mathbf{e}_2\right] + s_\parallel \mathbf{e}_3, \\ \mathbf{S}_n &= S_\perp \left[\cos(Qn+\phi)\mathbf{e}_1 + \sin(Qn+\phi)\mathbf{e}_2\right] + S_\parallel \mathbf{e}_3, \end{cases} \tag{2.2}$$

where $(\mathbf{e}_1, \mathbf{e}_2, \mathbf{e}_3)$ is an orthogonal basis and $s_\parallel^2 + s_\perp^2 = S_\parallel^2 + S_\perp^2 = 1$, is the ground state of Eq.(2.1) in a wide range of the model parameters.
An handwaving argument explaining the stability of the conical spiral state is provided by the following. An interchain interaction J_{int} weak compared to the other couplings does not affect strongly the "ferromagnetic" chain. Therefore, the "spiral" chain feels the "ferromagnetic" chain as an approximately uniform magnetic field. Since this field couples linearly to the uniform component $S_\parallel$ and the exchange energy of the "spiral" chain is quadratic in $S_\parallel$ ($S_\perp = \sqrt{1 - S_\parallel^2} \approx 1 - S_\parallel^2/2$) the stable state has $S_\parallel \neq 0$. In Appendix 2.A we use the generalized Luttinger-Tisza method [11; 9] to prove that the conical spiral state minimizes the energy Eq.(2.1).

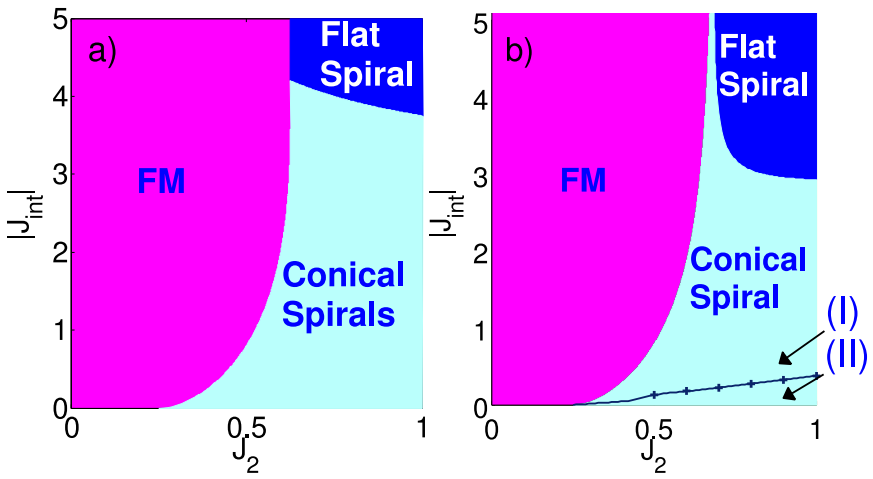

Figure 2.2: The phase diagram of the two-chain model Eq.(2.1) for $J_F = -1.5$, $J_{\rm int} < 0$, $\Delta = 0$ (a) and $\Delta = 0.02$ (b). In the anisotropic case the magnetization in the ferromagnetic and conical spiral states is oriented along z, while in the flat spiral phase the z axis is in the spiral plane. In region I of the conical spiral phase a FM domain wall induces a FE one, which does not happen in region II. The crosses represent points calculated numerically. All exchange constants are measured in units of $|J_1| = 1$.

As we are interested in the study of the domain wall structure, it is necessary to add a magnetic anisotropy term to the exchange energy Eq.(2.1) to make the width of the domain wall finite. We consider a single ion easy-axis anisotropy term on the sites of the "ferromagnetic" chain:

$$H_{\rm a} = -\Delta \sum_n (s_n^z)^2, \tag{2.3}$$

which for $\Delta > 0$ favors magnetization along the z axis and sets the width of the FM domain wall to $w \sim \pi\sqrt{\frac{|J_F|}{2\Delta}}$[12].

2.3 Phase diagram

The phase diagram of the isotropic ($\Delta = 0$) model Eq.(2.1) in the J_2-$J_{\rm int}$ plane is shown in Fig. 2.2(a). As was discussed above, for $J_{int} = 0$ the spiral component $S_\perp$ appears at $4J_2 = |J_F|$. For sufficiently strong interchain interaction, $\mathbf{s}_n$ is parallel to $\mathbf{S}_n$ and the system becomes equivalent to a single chain showing either the FM or the flat spiral ordering. The vertical line separating these two states is $4J_2 = |J_1| + |J_F|$ (in analogy with the $J_{int} = 0$ case), while the border line between the flat and conical spiral states is given by $\frac{J_{\rm int}}{J_F} = 2 + \frac{|J_F|-|J_1|}{2J_2}$ [see Appendix 2.B]. This analytically obtained phase diagram was confirmed by numerical simulations of the two-chain model.
It is worth noticing that when the inter-chain coupling is antiferromangetic, $J_{int} =$

$|J_{int}|$, only the relative orientation of spins in the two chains changes, i.e. the sign of $S_{\|}$ in Eq.(2.2) is opposite to that for $J_{int} = -|J_{int}|$. Therefore, the phase diagram Fig. 2.2 also applies for $J_{int} > 0$, provided that the ferromagnetic state and the conical spiral state are substituted, respectively, by the antiferromagnetic and ferrimagnetic spiral state. The rotation of spins in the conical and flat spirals induces an electric polarization $\mathbf{P} \propto \mathbf{Q} \times \mathbf{e}_3$, where $\mathbf{Q}$ is the spiral wave vector [13; 14; 15]. In the conical spiral state the polarization vector is orthogonal to the magnetization $\mathbf{M} \| \mathbf{e}_3$ [7].
Figure 2.2(b) shows the phase diagram when the anisotropy term is switched on ($\Delta > 0$). In the ferromagnetic and in the conical spiral phases the uniform magnetization is parallel to z. However, in the flat spiral state the anisotropy term Eq.(2.3) favors a spiral plane containing the z axis. Therefore, the spiral component of the spin ordering flops at the transition from the conical to the flat spiral state. The anisotropy affects also the shape of the flat spiral, distorting it from the circular state. As shown in Appendix 2.C, the main correction due to the term Eq.(2.3) to the flat circular state (Eq.(2.2) with $S_{\|} = s_{\|} = 0$) has the form:

$$\begin{aligned} \mathbf{S}_n = \mathbf{s}_n \quad = \quad & \left(\left(1 - \frac{\delta^2}{2} \sin(2qn) \right) \mathbf{e}_1 + \delta \sin(2qn) \mathbf{e}_3 \right) \cos(qn) + \\ & \left(\left(1 - \frac{\delta^2}{2} \sin(2qn) \right) \mathbf{e}_3 - \delta \sin(2qn) \mathbf{e}_1 \right) \sin(qn) \end{aligned} \tag{2.4}$$

where $\delta \propto \Delta$. The border line between the flat and the conical spiral state is strongly affected by the presence of magnetocristalline anisotropy, while the line separating the ferromagnetic and the conical spiral state does not change significantly. The phase diagram Fig. 2.2(b), calculated comparing the minimal energy of states Eq.(2.2) and the Ansatz Eq.(2.4), was found to be in perfect agreement with the results of numerical simulations.

2.4 Structure of ferromagnetic domain walls in conical spirals

Next we discuss the structure of domain walls in the conical spiral state. To ensure the presence of a FM domain wall in the system, we used the anti-periodic boundary condition for the spin projection on the easy axis in the ferromagnetic chain, $s^z_{n+L} = -s^z_n$. For all other spin components we used open boundary conditions to prevent the enforced commensurability of the conical spiral state by finite size effects. Despite the simplicity of the model, its numerical simulations are computationally demanding, as frustrated spin interactions result in a rather complex structure of the domain wall. We found the lowest-energy spin configuration for systems with up to 300 sites in each chain using the parallel tempering method [16; 17], which makes possible sampling of a large region of the configuration space with multiple local minima.
In the isotropic spin model Eq.(2.1) the width of the FM domain wall is of the order of the system size, $w \sim L$, in which case the normal to the spiral plane follows the slowly rotating uniform magnetization, so that $\mathbf{P}$ rotates together with $\mathbf{M}$. When the

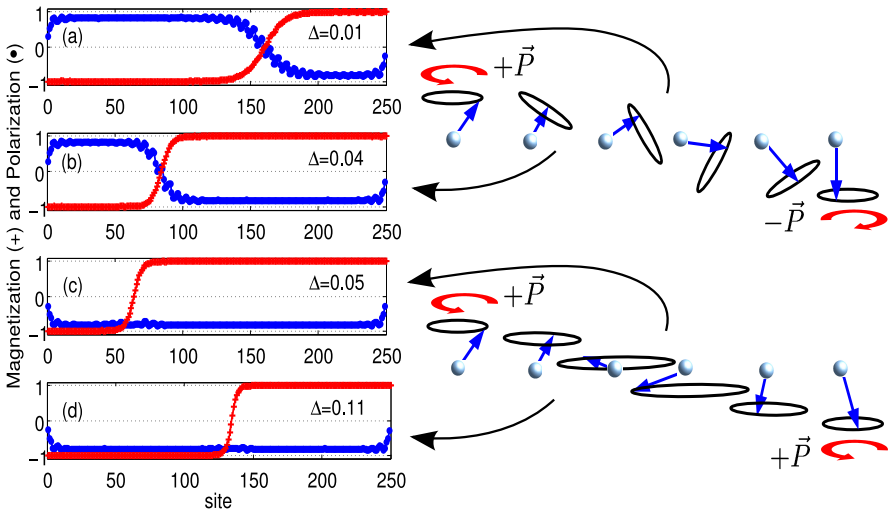

Figure 2.3: The magnetization s_n^z (red crosses) and the polarization $P_{n+1/2} = (\mathbf{S}_n \times \mathbf{S}_{n+1})^z$ (blue circles) in the domain wall. The four panels show the minimal-energy state when a FM domain wall is enforced by boundary conditions for $J_2 = 0.5$, $J_F = -4$, $J_{\rm int} = -0.1$ and four different values of the magnetic anisotropy: (a) $\Delta = 0.01$, (b) $\Delta = 0.04$ (clamped ferromagnetic and ferroelectric domain walls), (c) $\Delta = 0.05$ (d) $\Delta = 0.11$ (purely ferromagnetic domain wall). All exchange constants are measured in units of $|J_1| = 1$. The two types of domain walls are sketched in the right part of the figure.

anisotropy term is switched, the anisotropy strength Δ sets the width of the domain walls. By varying Δ we observe a transition from the regime where FM and FE domain walls are clamped to the regime where they are decoupled. Figures 2.3(a), (b) and (c) show the magnetization along the easy axis direction in the "ferromagnetic" chain, s_n^z, and the y-projection of the local polarization,

$$P_{n+1/2} \propto (\mathbf{S}_n \times \mathbf{S}_{n+1})^z, \tag{2.5}$$

induced in the "spiral" chain for two values of the anisotropy constant Δ (we assume that the chains are parallel to the x axis).

For relatively wide FM domain walls the direction of the rotation of spins in the spiral changes sign across the domain wall [see Fig. 2.3(a) and (b)], corresponding to the clamping of FM and FE domain walls responsible for the switching phenomena in $CoCr_2O_4$. When the thickness of the FM domain wall becomes smaller, the spins keep rotating in the same direction across the wall, so that the induced $\mathbf{P}$ has the same sign on both sides and the wall is purely ferromagnetic [see Fig. 2.3(c)].

Whether the FM domain wall will induce a FE domain wall or not depends on the balance between the interchain exchange energy, $E_{\rm int}$, and the energy cost of the FE domain wall, $E_{\rm FE}$. Expressions for the energies simplify in the limit $|J_F| \gg |J_{\rm int}|$, when $s_\perp \ll 1$ and the FM domain wall plays a role of the rotating magnetic field of

magnitude $|J_{\rm int}|$ applied to the spiral chain. If, furthermore, the spiral wave vector, given by $\sin^2\frac{Q}{2}=\frac{4J_2-|J_1|}{8J_2}$, is small, the energy of the FE domain wall, where the spiral plane rotates at the rate $\sim\frac{\pi}{w}\ll Q$ together with the applied field, is [see Appendix 2.D]:

$$E_{\rm FE}\sim J_2Q^2\left[1-2S_\parallel^2\right]\left(\frac{\pi}{w}\right)^2 w, \tag{2.6}$$

where $S_\parallel=\frac{|J_{\rm int}|}{J_2Q^4}$, while the interchain energy is

$$E_{\rm int}\sim-\frac{1}{2}S_\parallel|J_{\rm int}|w. \tag{2.7}$$

For $S_\parallel>\frac{1}{\sqrt{2}}$, the energy of the spiral decreases when its plane rotates and the FE and FM domain walls are clamped. This surprising result is explained by the fact that the spiral energy in the momentum space has a local *maximum* at $q=0$, so that the rotation of the uniform component, $S_\parallel\mathbf{e}_3$, results in an energy decrease, which for $S_\parallel>\frac{1}{\sqrt{2}}$ exceeds the reduction due to the rotation of the spiral plane.
For a nearly flat spiral, $S_\parallel\ll 1$, the dimensionless parameter determining the domain wall structure is $\lambda=\frac{QwS_\parallel}{\pi\sqrt{2}}=\frac{2|J_{\rm int}|}{|J_1|Q^3}\sqrt{\frac{|J_F|}{\Delta}}$: for $\lambda\gtrsim 1$, $E_{\rm FE}+E_{\rm int}<0$ and the FM and FE walls are clamped, while for $\lambda\lesssim 1$ the domain wall is purely ferromagnetic. As we discuss in Appendix 2.E, for a nearly flat spiral the continuum limit of Eq.(2.1) is:

$$E=\frac{|J_{\rm int}|}{\sqrt{2}Q}\int dv\left[\left(\frac{d\Theta}{dv}\right)^2+\sin^2(\Theta-\theta)\right]+const, \tag{2.8}$$

where the angles θ and Θ describe the rotation, respectively, of the magnetization and the spiral plane around an axis orthogonal to $\hat{z}$, and $v=\frac{\sqrt{2}|J_{int}|}{J_2Q^3}$ is the dimensionless coordinate along the chain, such that the domain wall thickness is $\sim\lambda$. The second term in Eq.(2.8) is the interaction energy between the ferromagnetic and spiral subsystems. Minimizing E, one can show that for $\lambda\gg 1$ the spin rotation axis follows closely the direction of the magnetization: $\Theta-\theta\approx\lambda^{-2}\theta''\left(\frac{v}{\lambda}\right)$. For $\lambda\ll 1$ the orientation of the spiral plane is only slightly perturbed in the vicinity of the FM domain wall: $\max(|\Theta|)\propto\lambda^2$, while $S_\parallel\approx\frac{|J_{\rm int}|}{J_2Q^4}\cos\theta$ changes sign across the domain wall.
In phase diagram Fig.2.2(b) the line inside the conical spiral phase separates the regions where the direction of rotation of spins changes through a ferromagnetic domain wall (I) from the region where it remains unchanged (II). This shows that for strength of the magnetocrystalline anisotropy fairly weak compared to the exchange constants ($\Delta=0.02J_1$) the region where ferromagnetic domain walls induce a ferroelectric one is much wider then the region where the walls are unclamped.
Spirals in frustrated magnets have a period of 10-20Å ($l\sim 13.4$Å for $CoCr_2O_4$), while the typical width of a FM domain wall is an order of magnitude larger. Furthermore, in cubic $CoCr_2O_4$ the lowest-order magnetic anisotropy is of fourth order, which

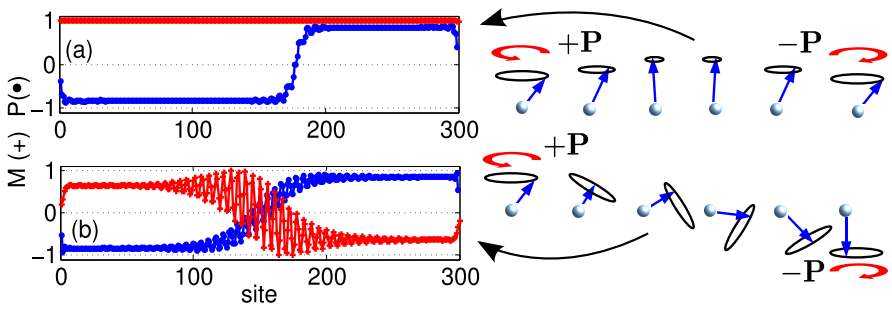

Figure 2.4: The magnetization s_n^z (red crosses) and the polarization $P_{n+1/2} = (\mathbf{S}_n \times \mathbf{S}_{n+1})^z$ (blue circles) in the domain wall. The two panels show the ground state when a FE domain wall is enforced by an electric field $+E(-E)$ applied at the left(right) end of the spiral chain for: (a) $J_2 = 0.5$, $J_F = -4$, $J_{\text{int}} = -0.1$, and $\Delta = 0.01$ (FE domain wall) and (b) $J_2 = 1$, $J_F = -1$, $J_{\text{int}} = -1.5$, and $\Delta = 0.01$ (FE + FM domain wall). All exchange constants are measured in units of $|J_1| = 1$. On the right the sketch of the two type of domain wall.

makes the domain wall width even larger, resulting in the perfect clamping of the FE and FM domain walls [2].

2.5 Ferroelectric domain walls

One might wonder whether the reciprocal effect, i.e. induction of FM domain walls by FE domain walls, can occur or not. In what follows we show that this kinf of induction is possible. However, the region in the phase diagram where a FE domain wall induces a ferromagnetic one does not coincide with the one discussed in the section above. In the previous discussion we showed that the energy cost of a domain wall that is both ferroelectric and ferromagnetic is often lower than the energy cost of a pure ferromagnetic one. However, now we have to compare it with the energy cost of a purely ferroelectric domain wall.

Ferroelectric domains can be stabilized by applying an electric field $+E(-E)$ at the left(right) end of the "spiral" chain, while the boundary conditions for spins are left open. Since spins in the "spiral chain" have no anisotropy of their own, the width of the FE domain wall is determined by the anisotropy in the FM chain and the interaction between the chains.

Figures 2.4(a) and (b) show s_n^z and $P_{n+1/2}$ for ferroelectric domain walls. The comparison of the configurations shown in Fig. 2.4(a) and Fig. 2.3(a), calculated for the same set of parameters but different boundary conditions, clearly shows the non-reciprocity of the domain wall clamping. The induction of a ferromagnetic domain wall by a ferroelectric one is shown in Fig. 2.4(b) where the uniform component of magnetization rotates together with electric polarization. The non-reciprocity of the effect seems to be a general phenomenon and may explain why the magnetization reversal in multiferroic $GdFeO_3$ results in an almost complete reversal of $\mathbf{P}$, while the

[2] The quartic anisotropy favors 90° domain walls.

electrically-induced changes in **M** are very small [18].

2.6 Concluding remarks

We presented the first simple and rigorously solvable isotropic spin model with conical spiral ordering. This allowed us to study numerically and analytically the structure of domain walls in a multiferroic material. We showed that there is a sharp transition between the regime where a ferromagnetic domain wall induces a ferroelectric one and the regime where those domain walls are decoupled. Furthermore, we showed that for typical values of magnetocrystalline anisotropy and spiral wave lengths the two kinds of domain walls are clamped. This explains why in the conical cycloidal magnet $CoCr_2O_4$ neighboring ferromagnetic domains with opposite magnetization have also opposite electric polarizations and why the reversal of magnetic field flips the sign of electric polarization. This study was focused on the energetics of domain walls in multiferroic materials. Another issue important for magnetoelectric switching is the dynamics of interacting ferroelectric and ferromagnetic domain walls. We showed that the fact that a ferromagnetic domain wall induces a ferroelectric one does not imply the inverse. This nonreciprocity explains why the magnetic control of electric polarization was demonstrated for many materials while the electric control of magnetization, which is more useful for applications, is hard to achieve.

2.A Appendix A: Conical spiral ground state

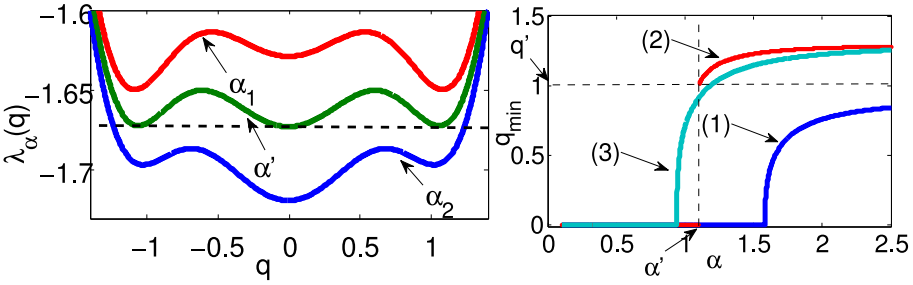

Figure 2.5: (a) Lowest eigenvalue of matrix l.h.s Eq.(2.10) as a function of the wave vector q for the coupling values $J_2 = 0.9$, $J_F = -1.5$ and $J_{int} = -2$ at different values of α . The presence of two degenerate global minima at α' allows the conical spiral state to be a solution of Eq.(2.10) and the strong constraint. (b) The wave vector q_{min} that minimize the lowest eigenvalue of matrix l.h.s. Eq.(2.10) for α in a continuous interval. For couplings that favors the ferromagnetic (1) ($J_2 = 0.4$,$J_F = -1.5$ and $J_{int} = -2$) and the flat spiral state (2) ($J_2 = 0.9$,$J_F = -1.5$ and $J_{int} = -7$)q_{min} is a continuous function of α. For the same couplings as (a) two degenerate minima ($q = 0$ and $q = q'$) are present at α'.

In this Aappendix we use the generalized Luttinger-Tizsa method [see sec. 1.5.1] to prove that the ground state of the model Eq.(2.1) is a conical spiral in the region showed in Fig. 2.2(a).
In momentum space the energy Eq.(2.1) can be written:

$$H = \sum_q \begin{pmatrix} \mathbf{S}_q \\ \mathbf{s}_q \end{pmatrix}^\dagger \begin{pmatrix} J_1 \cos q + J_2 \cos 2q & J_{\text{int}} \\ J_{\text{int}} & J_F \cos q \end{pmatrix} \begin{pmatrix} \mathbf{S}_q \\ \mathbf{s}_q \end{pmatrix} \tag{2.9}$$

where $\mathbf{S}_q = 1/L \sum_n^L \mathbf{S}_n \exp(-iqn)$ and $\mathbf{s}_q = 1/L \sum_n^L \mathbf{s}_n \exp(-iqn)$. With the weak constraint, $\sum_q |\mathbf{S}_q|^2 + \alpha^2 |\mathbf{S}_q|^2 = (1 + \alpha^2)$, the Lagrange equations reads:

$$\begin{pmatrix} J_1 \cos q + J_2 \cos 2q & \frac{J_{\text{int}}}{2\alpha} \\ \frac{J_{\text{int}}}{2\alpha} & \frac{J_F}{\alpha^2} \cos q \end{pmatrix} \begin{pmatrix} T_q^k \\ t_q^k \end{pmatrix} = \lambda_q \begin{pmatrix} T_q^k \\ t_q^k \end{pmatrix}, \tag{2.10}$$

where $(\mathbf{T}_q, \mathbf{t}_q) = (\mathbf{S}_q, \alpha \mathbf{s}_q)$ and k labels the spatial components. The matrix on the l.h.s. of Eq.(2.10) is the matrix $W(q)$ described in section 1.5.1. Its lowest eigenvalues $\lambda_\alpha^-(q)$ are plotted in Fig.2.5 (a) for different values of α and for a set of coupling constants that favors a conical spiral. At $\alpha = \alpha'$, $\lambda_\alpha^-(q)$ has two degenerate minima at $q = 0$ and $q = q'$, corresponding, respectively, to the normalized eigenvectors (V_0, v_0) and

$(V_{q'}, v_{q'})$. Thus,

$$(S^k_q, \alpha s^k_q) = (T^k_q, t^k_q) = \begin{cases} A^k_0(V_0, v_0) & \text{if } q = 0 \\ \frac{A^k_{q'}}{2}(V_{q'}, v_{q'}) & \text{if } q = q' \\ \frac{A^{*k}_{q'}}{2}(V_{q'}, v_{q'}) & \text{if } q = -q' \\ 0 & \text{otherwise} \end{cases} \tag{2.11}$$

satisfies Eq.(2.10) and minimizes Eq.(2.9) with the weak constraint, if the complex constants A^k_0, $A^k_{q'}$ are such that:

$$\sum_{k=x,y,z} |A^k_0|^2(V_0^2 + v_0^2) + |A^k_{q'}|^2(V^2_{q'} + v^2_{q'}) = 1 + \alpha'^2. \tag{2.12}$$

Among those solutions one can chose: $(A^x_0, A^y_0, A^z_0) = (A_\parallel, 0, 0)$ and $(A^x_{q'}, A^y_{q'}, A^z_{q'}) = (0, A_\perp, iA_\perp)$, where $A_\parallel$ and $A_\perp$ are real constants. With this choice of parameters the strong constraint can be reformulated in the form of the matrix equation:

$$\begin{pmatrix} V_0^2 & V^2_{q'} \\ v_0^2 & v^2_{q'} \end{pmatrix} \begin{pmatrix} A^2_\parallel \\ A^2_\perp \end{pmatrix} = \begin{pmatrix} 1 \\ \alpha^2 \end{pmatrix}, \tag{2.13}$$

which always has solutions, if the eigenvectors components are non-zero. For $(S_\parallel, s_\parallel) \equiv A_\parallel(V_0, \frac{v_0}{\alpha})$ and $(S_\perp, s_\perp) \equiv A_\perp(V_{q'}, \frac{v_{q'}}{\alpha})$, one obtains Eq.(2.2).
Note that to obtain such a state one has to find α' for which $\lambda^-(q)$ has two degenerate minima. In the opposite case the matrix on r.h.s. Eq.(2.13) is not a square one and the solution of the equations is not guaranteed. Figure 2.5 (b) shows the behavior of the wave vector q_{min} that minimizes $\lambda^-_\alpha(q)$ in an interval of α. In the ferromagnetic and the flat spiral states (respectively, curves 1 an 3 in Fig.2.5 (b)) q_{min} changes smoothly and the conical spiral state is not a solution of Eq.(2.10) with the weak constraint.

2.B Appendix B: Isotropic phase diagram

In the phase diagram Fig.2.2 the line separating the ferromagnetic and the flat spiral phases can be found by applying the flat spiral Ansatz (Eq.(2.2) with $S_\parallel = s_\parallel = 0$ and $S_\perp = S_\perp = 1$) and checking the stability of the $Q \neq 0$ solution. The energy of the flat spiral state,

$$E_{FS} = (J_1 + J_F)\cos q + J_2(2\cos^2 q - 1) + J_{int} \tag{2.14}$$

has a minimum at $Q = \arccos\left(\frac{|J_1+J_F|}{4J_2}\right)$, for $4J_2 > -(J_1 + J_F)$ and at $Q = 0$, otherwise. The border line between the flat spiral and the conical spiral state is found checking the stability of the flat spiral state towards the appearence of uniform spin components.

The perturbed state:

$$\begin{cases} \mathbf{S}_n^{(p)} = \left(1-\frac{\delta_1^2}{2}\right)(\cos(Qn+\phi)\mathbf{e}_1+\sin(Qn+\phi)\mathbf{e}_2)+\delta_1\mathbf{e}_3, \\ \mathbf{s}_n^{(p)} = \left(1-\frac{\delta_2^2}{2}\right)(\cos(Qn+\phi)\mathbf{e}_1+\sin(Qn+\phi)\mathbf{e}_2)+\delta_2\mathbf{e}_3, \end{cases} \tag{2.15}$$

is obtained by considering a small uniform perturbation with amplitude δ_1 in the ferromagnetic chain and δ_2 in the spiral chain. The difference between the energy per spin of the perturbed and unperturbed states is,

$$\frac{\delta H}{N} = \begin{pmatrix} \delta_1 \\ \delta_2 \end{pmatrix}^T \begin{pmatrix} \frac{(J_1+4J_2)^2-J_F^2+4J_2J_{int}}{8J_2} & \frac{J_{int}}{2} \\ \frac{J_{int}}{2} & J_F+\frac{J_F(J_1+J_F)}{4J2}-\frac{J_{int}}{2} \end{pmatrix} \begin{pmatrix} \delta_1 \\ \delta_2 \end{pmatrix}, \tag{2.16}$$

where only the terms quadratic in δ are kept. The instability towards the conical state occurs when a uniform mode softens, i.e. when one of the eigenvalues of the matrix $\mathcal{M}$ in the r.h.s of Eq.(2.16) vanishes. Therefore, the curve separating the two phases can be found imposing the condition: $\det(\mathcal{M})=0$, which gives $\frac{J_i}{J_F}=2+\frac{|J_F|-|J_1|}{2J2}$.

2.C Appendix C: Correction due to magnetocrystalline anisotropy to the circular spiral state

Here, we consider the lowest-order corrections in Δ to the circular spiral state using the model discussed in Sec. 1.4.2 with $S=1$. However, once J_1 is replaced by J_1+J_F, the same argument holds for the flat spiral phase of the model Eq.(2.1), where the strongest coupling constant is J_{int}.
Let $\boldsymbol{\delta}_j$ be the distortion of the spin sitting in the site j from its value $\mathbf{S}_j^0$ in the cirular spiral state. The easy axis anisotropy Eq.(2.3) favors a spiral state in a plane containing the axis $\mathbf{z}$ and the axis $\mathbf{e}$ perpendicular to $\mathbf{z}$. Every vector $\boldsymbol{\delta}_j$ also has to lie in the same plane and it has to be orthogonal to $\mathbf{S}_i^0$. Therefore, the distorted state is:

$$\mathbf{S}_j = \left[\left(1-\frac{\delta_j^2}{2}\right)\cos(Qj)+\delta_j\sin(Qj)\right]\mathbf{e}+\left[\left(1-\frac{\delta_j^2}{2}\right)\sin(Q)+\delta_j\cos(Q)\right]\mathbf{z}, \tag{2.17}$$

where we used $\sqrt{1-\delta_i^2}=1-\frac{\delta_i^2}{2}+\dots$ and Q is the wave vector of the unperturbed state. The difference between the energies Eq.(1.21) of the perturbed and unperturbed

states is $\delta H = \delta H^{(i)} + \delta H^{(a)}$, where:

$$\begin{aligned}\delta H^{(i)} &= \sum_{j=1}^{N}\left[J_1\left(\delta_j\delta_{j+1} - \frac{\delta_j^2+\delta_{j+1}^2}{2}\right)\cos(Q) + J_2\left(\delta_j\delta_{j+2} - \frac{\delta_j^2+\delta_{j+2}^2}{2}\right)\cos(2Q)\right], \\ \delta H^{(a)} &= \Delta\sum_{j=1}^{N}\left(\delta_j\sin(2Qj)\right) \end{aligned} \quad (2.18)$$

(we neglect higher order terms in in δ_j and Δ). Using the Fourier transform of the variables $\delta_j : \delta_q = 1/N\sum\delta_j\exp(iqj)$ the first of Eqs.(2.18) becomes:

$$\delta H^{(e)} = \sum_q\left[J_1\left(\cos(q)-1\right)\cos(Q) + J_2\left(\cos(2q)-1\right)\cos(2Q)\right]|\delta_q|^2. \quad (2.19)$$

The function $g(q)$ that multiplies $|\delta_q|^2$ in the right hand side of Eq.(2.19) is positive for all q. This indicates the stability of the circular spiral solution of the isotropic model. However, $g(0) = 0$, indicates that a a infinitesimal rotation of all spins by the same angle cost no energy, corresponding to a Golstone mode.
The second term in Eq.(2.18) in the Fourier space reduces to $\delta H^{(a)} = \Delta Im(\delta_{2Q})$. Since this term is linear in $Im(\delta_{2Q})$, for an arbitrary small Δ a distortion of the kind $\delta_j = \delta\sin(2Qj)$ is energetically favorable.
For the ladder model Eq.(2.1) one should introduce the vectors $\boldsymbol{\delta}_j^{(s)}$ and $\boldsymbol{\delta}_j^{(S)}$ for the distortions, respectively, in the ferromagnetic and spiral chains. However, in the flat spiral phase, where J_{int} is the biggest energy scale: $\boldsymbol{\delta}_j^{(s)} \approx \boldsymbol{\delta}_j^{(S)}$. In this limit the argument used for a single chain is also valid for the ladder model.

2.D Appendix D: Domain walls in the strong $|J_F|$ limit

Let us consider Eq.(2.1) in the limit of conical spiral with a large period and with $s_\perp \approx 1$. In this case, as discussed in the text, the ferromagnetic chain acts as magnetic field $h = |J_{int}|$ oriented along the z axis. Since the period is big compared to the lattice parameter, the Hamiltonian Eq.(2.1) can be replaced by its continuum limit $H[\mathbf{S}] = H^E[\mathbf{S}] + H^h[\mathbf{S}]$, where

$$H^E[\mathbf{S}] = \int dx\left[\frac{J_2}{2}\left[\left(\partial_x^2 + Q^2\right)\mathbf{S}\right]^2 - \mathbf{h}\cdot\mathbf{S}\right] \quad (2.20)$$

and $H^h[\mathbf{S}] = -\int dx\mathbf{h}\cdot\mathbf{S}$. The uniform spiral state is:

$$S^{(U)} = \sqrt{1-S_\parallel^2}\left[\cos(Q)\mathbf{e}_1 + \sin(Q)\mathbf{e}_2\right] + S_\parallel\mathbf{z}, \quad (2.21)$$

where $\mathbf{e}_1$ and $\mathbf{e}_2$ are two orthonormal vectors perpendicular to z and $S_\parallel = \frac{h}{J_2Q^4}$. Consider the case of a magnetic field rotating from $\mathbf{z}$ to $-\mathbf{z}$ around $\mathbf{e}_1$: $\mathbf{h} = h\mathcal{R}_{\mathbf{e}_1}(\theta)\mathbf{z}$.

Here the matrix representing $\mathcal{R}_{\mathbf{e}_1}(\theta)$ in the $\mathbf{e}_1, \mathbf{e}_2, \mathbf{z}$ basis is:

$$\mathcal{R}_{\mathbf{e}_1}(\theta) = \begin{pmatrix} 1 & 0 & 0 \\ 0 & \cos(\theta) & -\sin(\theta) \\ 0 & \sin(\theta) & \cos(\theta) \end{pmatrix}. \tag{2.22}$$

The state where spiral plane rotates together with the field is $\mathbf{S}^{(R)} = \mathcal{R}_{\mathbf{e}_1}(\theta)\mathbf{S}^{(U)}$. The energy cost of the ferroelectric domain wall can be calculated as $E_{FE} = H^E[\mathbf{S}^{(R)}] - H^E[\mathbf{S}^{(U)}]$. This gives:

$$E_{FE} = \frac{J_2}{2}\int_{-\infty}^{\infty} \left\{ \left[S_\parallel(\theta'^2 - Q^2) - \sqrt{1-S_\parallel^2}\left(\theta'' \sin(Qx) + 2\theta' Q\cos(Qx)\right)\right]^2 + \left[S_\parallel \theta'' + \sqrt{1-S_\parallel^2}\theta'^2 \right]^2 - S_\parallel^2 Q^4 \right\} dx, \tag{2.23}$$

where θ' and θ'' are, respectively, the first and the second derivative of θ respect to x. Since the rotation rate of the spiral pane is $\approx \frac{\pi}{\omega} \ll Q$, θ varies slowly and the terms containing θ'' can be neglected. Furthermore, since θ is approximately constant at the length scale of the order of the spiral period, also the terms containing odd powers of $\cos(Qx)$ vanish in the integration. Under these approximation one gets:

$$E_{FE} \approx J_2 \int_{-\frac{\omega}{2}}^{\frac{\omega}{2}} \left[\left(1 - 2S_\parallel^2\right) Q^2 \theta'^2 + \frac{\theta'^4}{2} \right] dx \approx J_2 (1 - S_\parallel^2) \left(\frac{\pi}{\omega}\right)^2 \omega, \tag{2.24}$$

where we used $\theta' << Q$.
The interchain energy gained by forming the domain wall, $E_{int} = H^h[S^{(R)}] - H^h[S^{(U)}]$, is:

$$E_{int} = -h\int_{-\infty}^{\infty} dx \left[S_\parallel \left[1 - \cos(\theta)\right] + \sqrt{1-S_\parallel^2}\sin(Qx)\cos(\theta) \right], \tag{2.25}$$

which under assumptions discussed above reduces to:

$$E_{int} = hS_\parallel \int_{-\frac{\omega}{2}}^{\frac{\omega}{2}} \left(1 - \cos(\theta)\right) dx \approx -\frac{S_\parallel h\omega}{2}. \tag{2.26}$$

2.E Appendix E: The $|S_\parallel| \ll 1$ limit

Consider the a vector field $\mathbf{\Omega}$ such that:

$$\partial_x \mathbf{S} = \mathbf{\Omega} \times \mathbf{S}. \tag{2.27}$$

The vector $\mathbf{\Omega}$ is defined up to the transformation $\mathbf{\Omega} \to \tilde{\mathbf{\Omega}} = \mathbf{\Omega} + \alpha\mathbf{S}$ where α is a function of x. By considering the additional constraint $\mathbf{\Omega} \cdot \partial_x \mathbf{S} = 0$, $\mathbf{\Omega}$ is uniquely defined and is parallel to the vector perpendicular to the spiral plane. By substituting

Eq.(2.27) in Eq.(2.20), we get,

$$H^E = \frac{\gamma}{2Q} \int \left[\mathbf{\Omega'^2} + (1-\Omega^2) + (2-\Omega^2)(\mathbf{\Omega}\cdot\mathbf{S})^2 + 2(\mathbf{\Omega}\cdot\mathbf{S}) \left[\left(\mathbf{\Omega}' \times \mathbf{S}\right) \mathbf{\Omega} \right] \right] dt, \tag{2.28}$$

where $t = Qx$, $\gamma = J_2 Q^4$ and $\mathbf{\Omega'} = \partial_t \mathbf{\Omega}$. Considering $\mathbf{\Omega}$ to be approximately constant over the spiral period and solving Eq.(2.27), we obtain Eq.(2.21) with $Q = \Omega$ and $\mathbf{z} = \hat{\mathbf{\Omega}} \equiv \frac{\mathbf{\Omega}}{\Omega}$. Replacing this solution in Eq.(2.28) and averaging over the period $\frac{2\pi}{\Omega}$, we obtain:

$$H^E \approx \frac{\gamma}{2Q} \int \left[\frac{1}{2}\Omega^2 \hat{\mathbf{\Omega}}'^2 \left(1 + S_\parallel^2\right) + \Omega'^2(1 - S_\parallel^2) + (2-\Omega^2)\Omega^2 S_\parallel^2 + (1-\Omega^2) \right] dt. \tag{2.29}$$

Under the same assumptions the Zeeman energy [see Appendix 2.D] averaged over the spiral period becomes: $H^h \approx -\int \frac{dt}{Q} S_\parallel \mathbf{h}\hat{\mathbf{\Omega}}$.
For $S_\parallel \ll 1$ and $\Omega' \approx 0$ the full Hamiltonian $H = H^E + H^h$ reads:

$$H = \int \frac{dt}{Q} \left[\frac{\gamma}{2} \left(\frac{\hat{\mathbf{\Omega}}'^2}{2}) + S_\parallel^2 \right) - S_\parallel \mathbf{h}\cdot\hat{\mathbf{\Omega}} \right] \tag{2.30}$$

and its minimization gives $S_\parallel = \frac{\mathbf{h}\cdot\hat{\mathbf{\Omega}}}{\gamma Q^4}$. Considering the spiral plane and the magnetization rotating around the $\mathbf{e}_1$ axis: $\Omega = \cos(\Theta)\mathbf{z} + \sin(\Theta)\mathbf{y}$ and $h = |J_{int}|(\cos(\theta)\mathbf{z} + \sin(\theta)\mathbf{y})$, Eq.(2.30) becomes:

$$H = \int \frac{dt}{Q} \frac{\gamma}{2} \left(\Theta'^2 - \frac{|J_{int}|}{2\gamma} \cos^2(\Theta - \theta) \right), \tag{2.31}$$

which after the substitution $v = \frac{\sqrt{2}|J_{int}|}{\gamma} t \equiv \frac{\sqrt{2}|J_{int}|}{j_2 Q^3} x$ gives Eq.(2.8).

Bibliography

[1] Ascher, E., Rieder, H., Schmid, H., and Stössel, H. *J. Appl. Phys.* **37**, 1404 (1966).

[2] Sannikov, D. *JETP* **84**, 293 (1997).

[3] Kimura, T., Goto, T., Shintani, H., Ishizaka, K., Arima, T., and Tokura, Y. *Nature* **426**(6962), 55–58 (2003).

[4] Goto, T., Kimura, T., Lawes, G., Ramirez, A. P., and Tokura, Y. *Phys. Rev. Lett.* **92**(25), 257201 (2004).

[5] Kagawa, F., Mochizuki, M., Onose, Y., Murakawa, H., Kaneko, Y., Furukawa, N., and Tokura, Y. *Phys. Rev. Lett.* **102**(5), 057604 (2009).

[6] Hur, N., Park, S., Sharma, P. A., Ahn, J. S., Guha, S., and Cheong, S.-W. *Nature* **429**(6990), 392–395 (2004).

[7] Yamasaki, Y., Miyasaka, S., Kaneko, Y., He, J.-P., Arima, T., and Tokura, Y. *Phys. Rev. Lett.* **96**(20), 207204 (2006).

[8] Choi, Y. J., Okamoto, J., Huang, D. J., Chao, K. S., Lin, H. J., Chen, C. T., van Veenendaal, M., Kaplan, T. A., and Cheong, S.-W. *Phys. Rev. Lett.* **102**(6), 067601 (2009).

[9] Kaplan, T. and Menyuk, M. *Phil. Mag.* **87**, 3711 (2007).

[10] Menyuk, N., Dwight, K., and Wold, A. *J. de Physique* **25**, 528 (1964).

[11] Lyons, D. H., Kaplan, T. A., Dwight, K., and Menyuk, N. *Phys. Rev.* **126**(2), 540–555 (1962).

[12] Landau, L. and Lifshitz, E. *Electrodynamics Of Continuous Media*. Pergamon Press, (1984).

[13] Katsura, H., Nagaosa, N., and Balatsky, A. V. *Phys. Rev. Lett.* **95**(5), 057205 (2005).

[14] Sergienko, I. A. and Dagotto, E. *Phys. Rev. B* **73**(9), 094434 (2006).

[15] Mostovoy, M. *Phys. Rev. Lett.* **96**(6), 067601 (2006).

[16] Swendsen, R. H. and Wang, J.-S. *Phys. Rev. Lett.* **57**(21), 2607–2609 (1986).

[17] Earl, D. and Deem, M. *Phys. Chem. Chem. Phys.* **7**, 3910 (2005).

[18] Tokunaga, Y., Furukawa, N., Sakai, H., Taguchi, Y., hisa Arima, T., and Tokura, Y. *Nat Mater* **8**(7), 558–562 (2009).

3

Manipulating electric polarization by magnetic field in spiral magnets

In this chapter we discuss magnetoelectric switching phenomena in spiral magnets when the spin ordering is manipulated by an applied magnetic field. We first consider the case of magnetic fields applied to a spin system with spiral ordering where the magnetocrystalline anisotropy favor the helicoidal spiral state. Then, we investigate the effects of magnetic fields applied to $Eu_{0.55}Y_{0.45}MnO_3$ by studying an effective spin model where the magnetic anisotropy induces three inequivalent directions for the spins and favors a cycloidal spiral ordering. In both cases we study the deformations of the spiral states produced by the combined effect of an applied magnetic field and magnetocrystalline anisotropy. The behavior of the electric polarization induced by the deformed spin spiral states explains a rich variety of phenomena observed experimentally.

3.1 Introduction

In the previous chapter we discussed how the structure of ferromagnetic domain walls in conical spirals allows for the flip of spontaneous electric polarization and magnetization by sweeping the magnetic field. The question that we address in this chapter is: how do the axis around which spins rotate, $\hat{\mathbf{e}}$, and $\mathbf{P}$ of a flat spiral state evolve when a uniform magnetic field is applied and then rotated?
Experimental investigation on this subject has been done for various spiral magnets [1; 2; 3; 4], however, among these compounds we discuss the case of $ZnCr_2Se_4$ and $Eu_{0.55}Y_{0.45}MnO_3$ due to the presence, in their structure, of only one magnetic species,

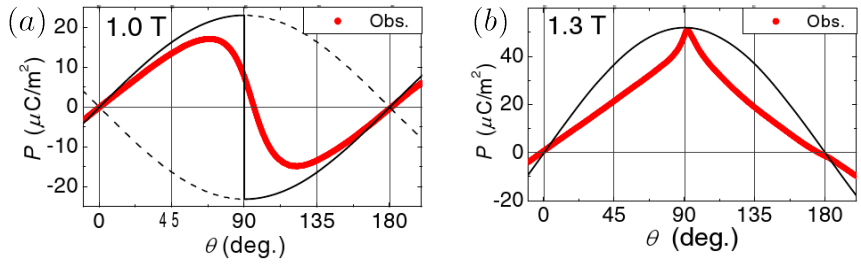

Figure 3.1: Observed evolution of electric polarization of $ZnCr_2Se_4$ for magnetic fields of strength $h = 1$ T (a) and $h = 1.3$ T (b) applied along the z ([100]) direction and then rotated by an angle θ within the xz plane ((001) plane (taken from Ref. [3]).

respectively, Cr^{3+} ($S = \frac{3}{2}$) and Mn^{3+} ($S = 2$).
First, let us discuss the case of the spinel $ZnCr_2Se_4$ studied by Murakawa *et al.* in Ref.[3]. The Cr^{3+} ions, which occupy the B sites in the spinel structure, order in an helical spiral at temperatures below 20 K. The spiral wave vector, $\mathbf{q}$, is oriented along the z direction (the $\langle 100 \rangle$ crystallographic direction), the spins lie in the xy plane ((100) crystallographic plane). Since the spins rotate around $\hat{\mathbf{e}} \parallel \mathbf{z}$, according to the rule of thumb $\mathbf{P} \propto \hat{\mathbf{e}} \times \mathbf{q}$, no spontaneous electric polarization is present. Murakawa *et al.* observed that, as a magnetic field with a component transverse to the original $\hat{\mathbf{e}}$ is applied, an electric polarization arises. Furthermore, they studied the evolution of the induced electric polarization when the applied magnetic field, $\mathbf{h}$, is first oriented along the z axis and then rotated towards the xy plane [3]. Depending on the strength of the applied magnetic field, three distinct regimes for the evolution of electric polarization, $\mathbf{P}$, were observed. Figure 3.1 (a) and (b), show the experimental results of Murakawa *et al.* for, respectively, $h = 1$ T and $h = 1.3$ T as the angle θ between $\mathbf{h}$ and the z axis is changed. At $h = 1.0$ T the electric polarization vanishes at $\theta = 0, \pi/2, \pi$ and changes direction at $\theta = \pi/2$ [see Fig. 3.1 (a)]. Whereas, at $h = 1.3$ T the electric polarization vanishes at $\theta = 0, \pi$ and reaches a maximum at $\theta = \pi/2$ [see Fig. 3.1 (b)]. Furthermore, a third regime is observed above $h \sim 2.4$ T . However, at these field strengths the evolution of $\mathbf{P}(\mathbf{h})$ is governed by the formation of domains with different wave vector [3] which makes this regime not relevant for the following discussion.
The evolution of electric polarization connects to the evolution of the spin ordering through the relation:

$$\mathbf{P} = \gamma \sum_{<i,j>} \left[\mathbf{r}_{i,j} \times \left(\mathbf{S}_i \times \mathbf{S}_j \right) \right], \tag{3.1}$$

where i, j are neighboring sites along the propagation direction of the spiral, $\mathbf{r}_{i,j}$ is the vector connecting them and γ is a constant. The spin cross product in the r.h.s.

Eq.(3.1) determines the axis $\hat{\mathbf{e}}(\mathbf{h})$ around which the spin rotates[1]. Using Eq.(3.1) and the results in Fig. 3.1 one can deduce the behavior of $\hat{\mathbf{e}}(\mathbf{h})$. At $h = 1.3$ T, $\hat{\mathbf{e}}(\mathbf{h})$ approximately follows $\mathbf{h}$ while at $h = 1.0$ T it oscillates around the z axis with a period which is doubled with respect to the period of $\mathbf{h}$.
A similar study was done for the multiferroic $Eu_{0.55}Y_{0.45}MnO_3$ [4], in which, at $h = 0$ and below $T_N = 22$ K, the spins of the Mn^{3+} ions lie in the ab plane and form a cycloidal spiral with wave vector along $\mathbf{b}$. There, in absence of an applied magnetic field, a spontaneous electric polarization, $P \parallel \mathbf{a}$, is present. The rotation by π rad of an applied magnetic field of strength $h \gtrsim 4.5$ T in the ac plane can reverse the electric polarization, $\mathbf{P}(-\mathbf{h}) = -\mathbf{P}(\mathbf{h})$ [4]. At lower field strengths, the same magnetic field rotation causes the weak oscillations of $\mathbf{P}$ around the a axis. The behaviors of $\hat{\mathbf{e}}(\mathbf{h})$ deduced from Eq.(3.1) above and below $h \approx 4.5$ T resemble those of $ZnCr_2Se_4$, respectively, above and below $h \approx 1.0$ T.
Furthermore, in this compound the evolution of electric polarization, $\mathbf{P}(\mathbf{h})$ (and thus of $\hat{\mathbf{e}}(\mathbf{h})$), is shown to be extremely sensitive to small variation of the axis around which $\mathbf{h}$ is rotated [4]. Magnetic fields of strength $h = 4$ T rotated by π rad around an axis slightly tilted form $\mathbf{c}$ in the bc plane reverses the electric polarization: $\mathbf{P}(-\mathbf{h}) = -\mathbf{P}(\mathbf{h})$. Whereas, the same π rad rotation of magnetic field around an axis slightly tilted from the $\mathbf{c}$ in the ac plane does not affect the direction of $\mathbf{P}$.
As Ref. [3] and Ref. [4] suggest, the evolution of electric polarization of spiral magnets in rotating magnetic field can be study from Eq.(3.1) in the framework of the deformations of the spin spiral ordering induced by a magnetic field which competes with magnetocrystalline anisotropies. In this chapter we consider a spin model with flat spiral ground state when a magnetocrystalline anisotropy is present. We study the evolution $\mathbf{P}(\mathbf{h})$ by calculating the deformation from the flat spiral state induced by a magnetic field oriented at various directions with respect to the anisotropy axes. First we consider a magnetocrystalline anisotropy compatible with the symmetry of $ZnCr_2Se_4$ and we recover quantitatively the evolution of $\mathbf{P}(\mathbf{h})$ shown in Fig.3.1. Then we discuss the case of $Eu_{0.55}Y_{0.45}MnO_3$. There we show that the type of magnetocrystalline anisotropy of this material allows for a more complex manipulation of $\mathbf{P}$ by magnetic fields.

3.2 Evolution of electric polarization in $ZnCr_2Se_4$ under magnetic field rotations

We first discuss the case of the helicoidal magnet $ZnCr_2Se_4$. We consider a chain of N classical spins $\mathbf{S}_j$ ($j = 1, \ldots, N$) described by the Hamiltonian:

$$H = H_{exc} + H_a + H_h, \tag{3.2}$$

where the exchange Hamiltonian H_{exc} is given by Eq.(1.21), H_a is the magnetocrystalline anisotropy term specified below and $H_h = -\sum_{j=1}^{N} \mathbf{h} \cdot \mathbf{S}_j$. For the cubic spinel,

[1] While this is obvious for flat spiral it is not for conical spiral. In conical spiral, the three-dimensional spin texture, $\mathbf{S}_i = \mathbf{M} + \boldsymbol{\sigma}_i$, is a sum of the uniform magnetization $\mathbf{M}$ and a spiral rotating spin component $\boldsymbol{\sigma}_i$. There, the average over a period of $\mathbf{S}_i \times \mathbf{S}_j$ reduces to the average of $\boldsymbol{\sigma}_i \times \boldsymbol{\sigma}_i$, i.e. $\hat{\mathbf{e}}(\mathbf{h})$.

the lowest order anisotropy contribution to the energy density of the continuum model[2], $\Delta \sum_{\alpha=x,y,z} (\partial_\alpha S^\alpha)^2$, favors, for $\Delta > 0$, a spin orientation perpendicular to the spiral wave vector, i.e. the helicodal spiral spin structure. For the spiral wave vector oriented along the z axis the discrete form of the anisotropy term is:

$$H_a = \Delta \sum_{n=1}^{L} (S_i^z - S_{i+1}^z)^2. \tag{3.3}$$

The ground state of model Eq.(3.2) at $\Delta = 0$ and $\mathbf{h} = 0$ was discussed in Sec. 1.4.2 and it is a flat circular spiral for $|J_1| < 4J_2$. An applied magnetic field transforms the flat spiral into a circular conical spiral with a uniform magnetization $\mathbf{M} = \gamma \mathbf{h}$, where $\gamma = \frac{4J_2}{(4J_2+J_1)^2}$, without modify its wave vector $q = Q = \arccos\left(\frac{|J_1|}{4J_2}\right)$. Thus the only two degenerate states are those with $\hat{\mathbf{e}}$ parallel or antiparallel to $\mathbf{h}$. For $h = 0$, the anisotropy term favors spiral states with $\hat{\mathbf{e}}$ parallel or antiparallel to $\mathbf{z}$. When both anisotropy and magnetic field are present, the deformation of the screw spiral, and thus $\hat{\mathbf{e}}(\mathbf{h})$, depends on the balance between anisotropy and Zeeman energies. The detailed structure of the spin order in this case is complex, analytical results are achievable only under some approximation and numerical calculations are required. Consider a magnetic field rotating in the xz plane and forming an angle ϕ with the z axis: $\mathbf{h} = h(\sin\phi\hat{\mathbf{x}} + \cos\phi\hat{\mathbf{z}})$. To obtain the evolution of $\mathbf{P}(\mathbf{h})$ we assume that the field is rotated slowly compared to time scale needed to reach the equilibrium. Then the $\mathbf{P}(\mathbf{h})$ can be calculate from the electric polarization of the minimal energy state of Eq.3.2 at different ϕ.

To calculate the ground state of the model in Eq.(3.2) we used the parallel tempering procedure [6; 7] discussed in Sec. 1.5.3. We compare the numerical results with the lowest order correction to the circular conical spiral state obtained by the minimization of the Ansatz[3]:

$$\begin{aligned}\mathbf{S}_n = \quad & \left(\sqrt{1-A^2} - \frac{\delta^2 \cos^2(qn)}{2}\right)(\cos(qn)\hat{\mathbf{y}} + \sin(qn)\hat{\mathbf{u}}_\perp) + \\ & \delta \cos qn\,(\sin(qn)\hat{\mathbf{y}} - \cos(qn)\hat{\mathbf{u}}_\perp) + A\hat{\mathbf{e}}\end{aligned} \tag{3.4}$$

where $\hat{\mathbf{u}}_\perp$ is the unit vector perpendicular to both $\hat{\mathbf{e}}$ and $\mathbf{y}$ and δ is the amplitude of the perturbation. Ansatz Eq.(3.4) holds for small Zeeman energies compared with the exchange energy scale and in the case $\Delta \ll h$. The choice of this Ansatz has a similar motivation as the choice of Ansatz Eq.2.4 discussed in the previous chapter and it is explained in Appendix 3.A.

Experiments show that the evolution of spiral in rotating magnetic field crucially depends on the strength of the magnetic field [3; 4] and that one can address the different evolutions on whether the magnetic field is strong enough to maintain a conical spiral state during the whole rotation or not. As the term that energetically favors the collapse to a flat spiral state is Eq.(3.3) it is important to study the minimal energy state in a magnetic field with $\phi = \pi/2$ (orthogonal to $\hat{\mathbf{e}}(0)$) where anisotropy

[2]Here we neglected the tiny tetragonal distortion appearing below the magnetic transition [5].

[3]The usage of this Ansatz was suggested by S. Artyukhin.

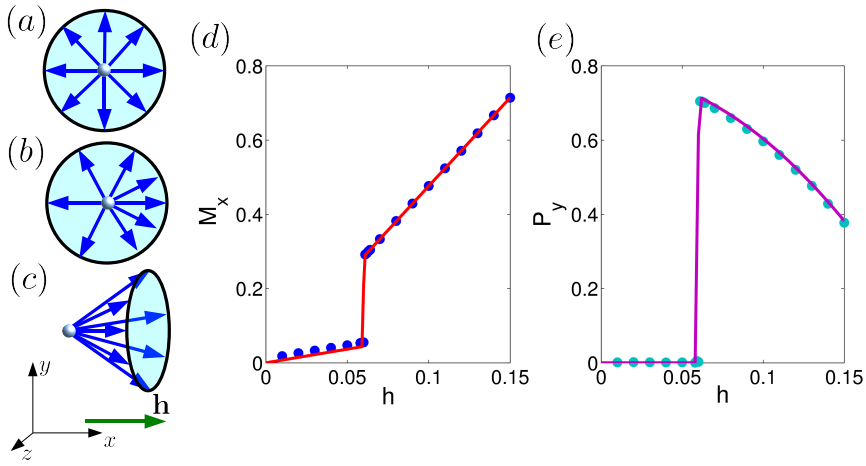

Figure 3.2: Sketches of the spin rotation in the spiral state at $h = 0$ (a), at $h < h_c$ (b) and at $h > h_c$ (c). The magnetic field dependence of the magnetization M_x (d) and the electric polarization P_y (e) in the minimal energy state of the model Eq.(3.2) for a magnetic field applied along $\hat{\mathbf{x}}$ for $J_2 = 0.4$ and $\Delta = 0.02$. The solid lines represent the results obtained using the Ansatz Eq.(3.4), and the filled circles are the values obtained by numerical minimization.

effects are maximal. Therefore, we first discuss the spiral deformation when the magnetic field is applied along **x**.

3.2.1 Magnetic field in the spiral plane

For small magnetic field ($h \ll \Delta$) applied along $\hat{\mathbf{x}}$ the ground state remains planar: $A = 0$ and $\hat{\mathbf{e}}(\mathbf{h}) \parallel \hat{\mathbf{z}}$. The presence of the magnetic field favors a smaller angle between neighboring spins when they have have a component parallel to the applied field and a bigger angle in the opposite case [see Fig. 3.2(b)]. This can be showed by substituting the Ansatz Eq.(3.4) with $A = 0$ and $\hat{\mathbf{u}}_\perp = \mathbf{x}$ in Eq.(3.2) and averaging over the period $\frac{2\pi}{q}$. This gives the energy density:

$$\begin{aligned} \frac{E}{L} \approx\ & J_1\cos(q) + J_2\cos(2q) - \frac{h\delta}{2} + \\ & \left[J_1(\cos^2 q - \cos q) + J_2(\cos^2(2q) - \cos(2q))\right]\delta^2. \end{aligned} \tag{3.5}$$

Note that the spiral wave vector q, obtained by minimizing the energy in Eq.(3.5), is also modified by the magnetic field. However, sizable deviations of q from its value at $h = 0$ are present only for spiral periods much larger than the lattice constant. The Ansatz Eq.(3.5) allows to extend the calculations previously done in Ref.[8] where q is assumed to be the same as the original circular spiral state. For spirals with short period $q \approx Q$, the magnetization in the spiral plane can be found minimizing Eq.(3.5)

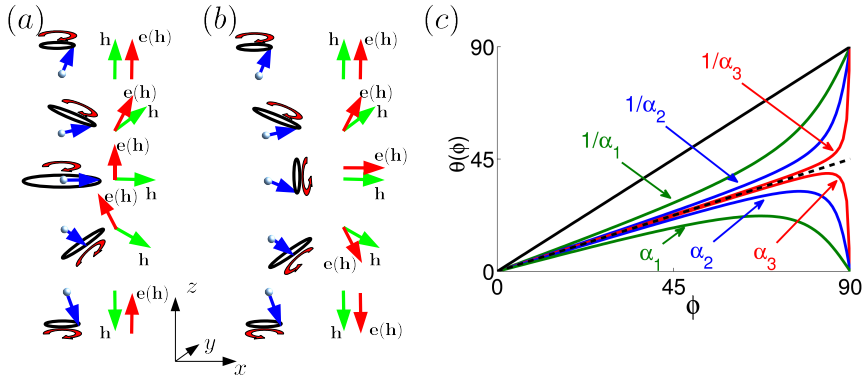

Figure 3.3: Pictorial representation of the evolution of $\hat{\mathbf{e}}$ when a magnetic field $\mathbf{h}$ is rotated for $h < h_c$ (a) and $h < h_c$ (b). (c) Duality of the minimal energy solution $\theta_M(\phi, \alpha)$ of Eq.(3.6) for $\alpha = \alpha_i$ ($\alpha_1 = 0.7$, $\alpha_2 = 0.9$ and $\alpha_3 = 0.98$). As described in the text, the sum of the solution $\theta_M(\phi, 1/\alpha_i)$ and $\theta_M(\phi, \alpha_i)$ is ϕ.

respect to δ. This gives $M^x = 2\delta = h\chi_h$ where $\chi_h = 4\gamma J_2^2 \left[J_1^2 - 4J_1J_2 + 8J_2^2\right]^{-1}$ is the magnetic susceptibility. As in this state $\hat{\mathbf{e}}(\mathbf{h})$ remains parallel to the spiral wave vector, no spontaneous polarization appears.
As sketched in Fig. 3.2(c), when the Zeeman energy becomes comparable with the anisotropy energy, a flop transition from a planar to a conical spiral state with $\hat{\mathbf{e}}(\mathbf{h})$ oriented along $\mathbf{x}$ occurs. For $\Delta \ll J_2$, when the deviation from the circular conical state can be neglected ($\delta = 0$), the critical field can be found by comparing the energy of the flat spiral and the energy of the conical spiral state Eq.(3.4) with $\hat{\mathbf{u}}_\perp = \mathbf{z}$ and $\hat{\mathbf{e}} = \mathbf{z}$. The approximate expression for the critical field is $h_c = 2\sqrt{\Delta\left(\frac{1}{\gamma} - \Delta\left(1 - \frac{J_1}{4J_2}\right)\right)}$. The flopped state is ferroelectric and the electric polarization (parallel to $\mathbf{y}$), as a function of the field, has a maximum at the transition. When an applied field is increased further, the amplitude of the spiral component decreases and the induced polarization falls off to zero, vanishing at $h_s = \frac{1}{\gamma} - \Delta\left(1 - \frac{J_1}{4J_2}\right)$. Figures 3.2 (d) and (e) show the results obtained using the Ansatz Eq.(3.4) and the numerical minimization of the energy Eq.(3.2).

3.2.2 Magnetic field rotation

We turn now to the evolution of the spiral state when a magnetic field is first applied along the z-axis and then slowly rotated by π around the $\hat{\mathbf{y}}$ axis. As shown in Fig. 3.3(a), if at $\phi = \pi/2$ the stable state is a flat spiral ($h < h_c$), the rotation direction $\hat{\mathbf{e}}(\mathbf{h})$ cannot follow the magnetic field and its direction is the same at $\phi = 0$ and $\phi = \pi$. If at $\phi = \pi/2$ the minimal-energy state is a conical spiral ($h > h_c$), $\hat{\mathbf{e}}(\mathbf{h})$ has opposite directions before and after the rotation [see Fig. 3.3(b)]. However, at $h > h_c$, $\hat{\mathbf{e}}(\mathbf{h})$ does not follow precisely the magnetic field vector due to the competition between

between anisotropy and Zeeman energies. In the case of very small anisotropies, when the deviations from the exact conical spiral state can be neglected, the energy per spin can be found inserting Eq.(3.4) with $\delta = 0$ in Eq.(3.2). After minimizing with respect to q and A, one gets

$$\frac{E}{\Delta L} \propto -\cos^2\theta - \alpha^2\cos^2(\theta - \phi) + const, \tag{3.6}$$

where $\alpha = h/h_c$ and θ is the angle between $\hat{\mathbf{e}}(\mathbf{h})$ and the z axis. The first term in the r.h.s. of Eq.(3.6) represents the energy loss due to the rotation of the spiral plane from the easy plane imposed by the magnetic anisotropy. The second term represents the energy loss by having the plane of the spiral component not perpendicular to $\mathbf{h}$. Minimizing Eq.(3.6) with respect to θ one gets

$$\theta_m(\phi,\alpha) = \arccos\sqrt{\frac{1}{2} + \frac{\alpha\cos(2\phi)+1}{2(1+\alpha^2+2\alpha\cos(2\phi))^{1/2}}}. \tag{3.7}$$

Consider the minimum $\theta_m(\phi,\alpha)$ of $E/(\Delta L)$ when ϕ is varied between 0 and $\pi/2$. From Eq.(3.6) it is clear that the duality transformation $\theta_m(\phi,\alpha) = \phi - \theta_m(\phi,1/\alpha)$ holds. Thus, the functions $\theta_m(\phi,1/\alpha)$ can be directly obtained by $\theta_m(\phi,\alpha)$ as shown in Fig. 3.3(c). For magnetic fields lower than h_c, $\alpha < 1$, the first term in Eq.(3.6) is always larger than the second, so that the minimum of the energy can only be realized for θ smaller than $\pi/4$. In particular, the maximum of $\theta_m(\phi,\alpha)$ is obtained at $\phi_M(\alpha) = \frac{1}{2}\arccos(\alpha^2)$ and $\theta(0,\alpha) = \theta(\pi/2,\alpha)$.
The solution for $h > h_c$ ($\alpha > 1$) can be directly found by the duality transformation. When the magnetic field exceeds h_c but still is comparable with it, θ increases slowly until $\phi_M(1/\alpha)$ (the same point where the maximum occurs for $1/\alpha$), and then it rapidly increases to catch up with the field at $\phi = \pi/2$ giving rise to a cusp like anomaly. As the field is increased further, the second term in Eq.(3.6) is dominant and the rotation axis directly follows the magnetic field direction.
Assuming that $\hat{\mathbf{e}}(\mathbf{h})$ is continuous at $\phi = \pi/2$, it is possible to infer the evolution of $\hat{\mathbf{e}}(\mathbf{h})$ for arbitrary rotations. For $h < h_c$, the rotation direction oscillates around $\hat{\mathbf{e}}(0)$ and becomes parallel to it at $\phi = \pi/2$. As a consequence, at this point the electric polarization Eq.(3.1) changes sign, so that $\mathbf{P}$ completes an oscillation between $\phi = 0$ and $\phi = \pi$. For $h > h_c$ the rotation direction follows the magnetic field with some delay and is parallel to it only at $\pi/2$, thus $\mathbf{P}$ has the same periodicity of the field.
The duality argument is exact only for circular conical spiral but all the other considerations can be extended considering the deviation from the circular spiral state. For $\Delta \ll J_2$ the main contribution to the distortion of the spiral comes from the component of the magnetic field perpendicular to $\hat{\mathbf{e}}$ and the corrections to the circular conical spiral state in the Ansatz of Eq.(3.4) are the most relevant. Fig. 3.4 shows the comparison between the polarization obtained by the full numerical minimization of the model in Eq.(3.2), by using the Ansatz of Eq.(3.4) and the reproduction of the experimental results. The ratio between the exchange constant $\frac{J_2}{J_1}$ is such that q is approximately the wave vector observe experimentally in $ZnCr_2Se_4$. The ratio $\frac{\Delta}{J_1}$ and

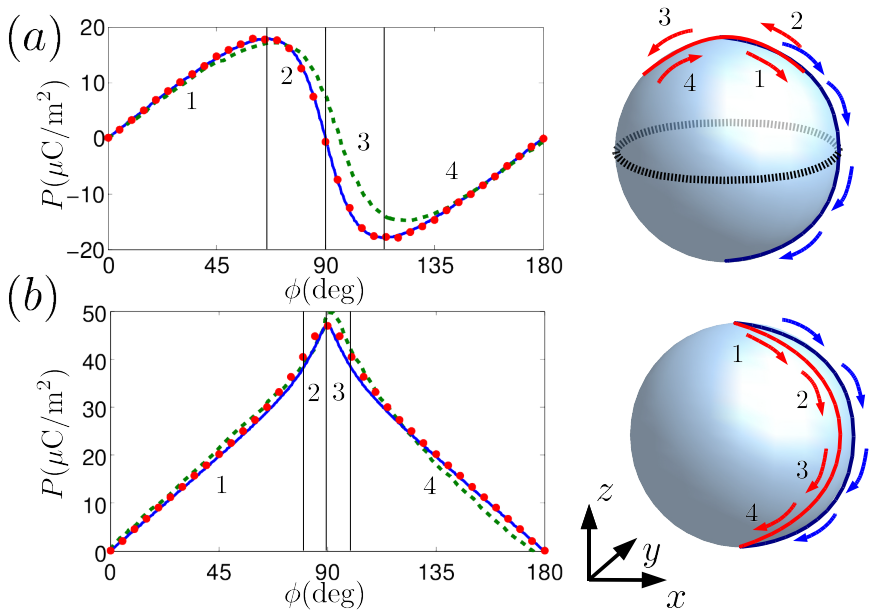

Figure 3.4: Electric polarization in the ground state of the model Eq.(3.2) for a magnetic field first applied along **z** and then rotated by ϕ in the xy plane. The magnetic field strength is below (a) and above (b) the critical field. The parameters are: $h = 0.0125J_1$ (a), $h = 0.015J_1$(b), $J_2 = 0.31J_1$, $\Delta = 0.012J_1$, are chosen to reproduce the experimental values (green dashed line). The solid line and the filled circles represent, respectively, the result obtained by using the Ansatz in Eq.(3.4) and by numerical minimization. The blue line on the spheres represents the path of the magnetic field **h**, while red line on the spheres shows the evolution of $\hat{\mathbf{e}}(\mathbf{h})$. For low magnetic fields oriented along the dashed line the conical spin spiral state collapses in a flat spiral.

the value of γ have been adjusted to obtain a reasonable agreement with experiments simultaneously at $h = 1.0$ T and $h = 1.3$ T. The good agreement between theoretical and experimental results underlines that, although what we use it is just an effective model, the physics of these phenomena is mainly related to the strength and the shape of magnetocrystalline anisotropy.

3.3 Rotating electric polarization in $Eu_{0.55}Y_{0.45}MnO_3$ by rotating magnetic fields

We discuss next the the behavior of **P** in the cycloidal spiral magnet $Eu_{1-x}Y_xMnO_3$, studied in Ref.[4]. Multiferroic orthorhombic perovskites $RMnO_3$ are characterized by the so-called $GdFeO_3$ distortion where, as shown in Fig. 3.5, the MnO_6 octahedra rotate in an alternate fashion along a and b. The magnitude of the distortion strongly

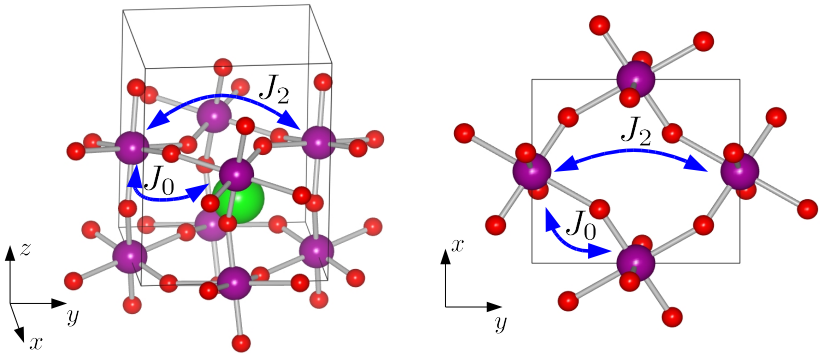

Figure 3.5: Unit cell of orthorhombic $RMnO_3$. The violet, green and red balls represent, respectively, Mn^{3+}, rare earth, and oxygen ions

depends on the radius of the rare earth ion [9]. The rotation of the MnO_6 octahedra reduces the exchange coupling J_0 between nearest neighbor Mn ions and enhances the coupling between J_2 next-nearest-neighbor Mn ions [see Fig. 3.5].
Moreover, Jahn-Teller distortions, caused by electrons in the e_g orbitals of Mn^{3+} (with electronic structure $e_g^1 t_{2g}^3$ and $S = 2$), give rise to orbital ordering at temperatures much higher than the Néel temperature [9]. The occupied e_g orbitals of neighboring Mn ions within the same xy layer order in a staggered way, i.e. the $3x^2 - r^2/3y^2 - r^2$-type of orbital ordering[4]. As noticed in Ref.[10] this type of orbital ordering enhances the antiferromagnetic exchange between next-nearest-neighbor Mn^{3+} ions along the y direction and favors ferromagnetic exchange between nearest-neighbor Mn^{3+}.
In the following discussion we consider the case of $Eu_{(1-x)}Y_xMnO_3$ where the ions on the A sites (here Eu or Y) have $S = 0$. As shown in Ref.[11], magnetic rare earth ions on the A sites of the perovskite structure strongly affect the interaction between spins of Mn^{3+} ions and complicate substantially our analysis.
The experimentally observed magnetic ordering in $Eu_{(1-x)}Y_xMnO_3$ ($x = 0.45$) is a spin spiral in the xy plane with the wave vector $\mathbf{q} = \frac{2\pi}{b}(0, \frac{k}{b}, 0)$ where b is the unit cell length in the y directions and $k \approx 0.2$ varies with the doping concentration[5] [12]. Thus, for the purpose of studying the minimal energy state, the exchange part of the spin Hamiltonian of $Eu_{0.55}Y_{0.45}MnO_3$ can be mapped onto the chain model Eq.(1.21) provided that the chain is oriented along y and that $J_1 = 2J_0$.
The Jahn-Teller distortions of the MnO_6 from the regular octahedral structure allow

[4]The coordinate system used refers to the one in the local distorted octahedral environment and should not be confused with the coordinate system used elsewere in the text.

[5]In the notation used in the text the crystallographic axes a, b, c corresponds, respectively, to the x, y and z axes

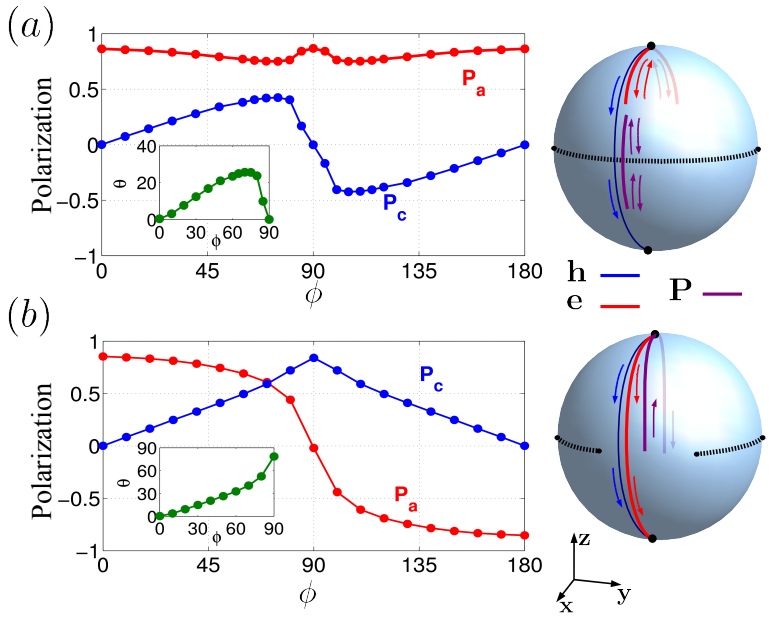

Figure 3.6: Evolution of the electric polarization **P** and the angle $\theta = \arccos(\hat{\mathbf{e}} \cdot \mathbf{a})$ (in-sets) for the ground state of the model described in Eq.(3.2) for magnetic field rotated around the **b** axis at $h < h_c^{(a)}$ (a) and $h > h_c^{(a)}$ (b). The parameters used are: $J_2 = 0.55$, $\Delta = 0.08$ and $\alpha = \pi/6$. All the parameters are expressed in units of J_1.

for single ion quadratic anisotropies of the form:

$$H_a = -\Delta \sum_{n=1}^{L} \left[(\hat{\mathbf{v}}_+ \cdot \mathbf{S}_{2n})^2 + (\hat{\mathbf{v}}_- \cdot \mathbf{S}_{2n+1})^2 \right] \tag{3.8}$$

where $\hat{\mathbf{v}}_\pm$ are determined by the direction of neighboring occupied e_g orbitals. For simplicity, here we consider $\hat{\mathbf{v}}_\pm$ to lie in the xy plane, $\hat{\mathbf{v}}_\pm = \pm \sin\psi \hat{\mathbf{x}} + \cos\psi \hat{\mathbf{y}}$, and we use $\psi = 0.52$ rad that approximately gives the directions of the easy axis described in the more complex single ion anisotropy used in Ref.[10].
The anisotropy term Eq.(3.8) effectively makes the y axis an easy axis and the z axis an hard axis for the spins. Therefore, at $\mathbf{h} = 0$, $\hat{\mathbf{e}} \parallel \mathbf{z}$ and **P** is oriented along the **x** axis. The inequivalence between the spin axes results in two different critical fields, $h_c^{(x)}$ and $h_c^{(y)}$, which are necessary to change the rotation plane of the spiral from xy to, respectively, the yz and the xz plane. The discussion of the evolution of polarization when **h** is applied along z and then rotated around the y axis is similar to the one for $ZnCr_2Se_4$. For $h < h_c^{(x)}$, a rotation of **h** around **y** from **z** up to $-\mathbf{z}$ does not reverse $\hat{\mathbf{e}}$ and **P**: $\mathbf{P}(\mathbf{h}) = \mathbf{P}(-\mathbf{h})$. As shown in Fig. 3.6(a), the oscillation of $\hat{\mathbf{e}}(\mathbf{h})$ during the rotation corresponds to a small cycloidal component of the spiral in the bc plane and

induces an oscillation of the c component of the polarization. For $h > h_c^{(a)}$, the same rotation of the field reverses $\hat{\mathbf{e}}$ and $\mathbf{P}$ [see Fig. 3.6(b)]. This numerical results reproduce qualitatively the behavior observed in Ref. [4]. The discussion of the evolution $\mathbf{P}(\mathbf{h})$ for the rotations of $\mathbf{h}$ around an axis slightly tilted from $\mathbf{z}$ in the yz and xz planes studied in Ref.[4] is more subtle.

Consider the case where $\mathbf{h}$ is rotated around an axis $\mathbf{u}$ which lies in the yz plane and that forms a small angle ϱ with z axis [see Fig. 3.7(a)]. Furthermore, consider the deformation from the spiral state with $\hat{\mathbf{e}}(0)$ oriented along the positive z direction. The field is initially applied in the yz plane and then rotated by ϕ. For $0 < h < h_c^{(x)}$ the spiral is deformed to a conical spiral for all ϕ but $\phi = \pi/2$ where it collapses to a flat spiral state with $\hat{\mathbf{e}} \parallel \mathbf{z}$. At $\phi = 0$, the uniform part of the conical spin spiral has negative z component and $\hat{\mathbf{e}}(\mathbf{h})$ is slightly tilted from $\mathbf{z}$ towards the $-\mathbf{y}$. As shown in Fig. 3.7(a), when ϕ is increased from 0 to $\pi/2$, $\hat{\mathbf{e}}(\mathbf{h})$ moves towards the z axis and acquires negative x component that vanishes at $\phi = \pi/2$. As ϕ is further increased the spin spirals becomes conical again and its uniform part has a positive z component. There, $\hat{\mathbf{e}}(\mathbf{h})$ moves from z to its original value at $\phi = 0$ but acquiring a positive x component. Therefore, the induced electric polarization oscillates around the positive x direction in the xz plane [see Fig. 3.7(b)]. For $h > h_c^{(x)}$ the spiral is conical for every ϕ and $\hat{\mathbf{e}}(\mathbf{h})$ follows $\mathbf{h}$ with some lag that vanishes at $\phi = \pi/2$ where $\hat{\mathbf{e}}$ crosses the xy plane [see Fig. 3.7(c)] and that decreases as the field strength is increased. The induced electric polarization rotates in the xz plane and is reversed at $\phi = \pi$: $\mathbf{P}(-\mathbf{h}) = -\mathbf{P}(\mathbf{h})$. [see Fig. 3.7(d) and (c)].

Consider now the similar case where the axis $\mathbf{u}$ is tilted in the xz plane and the field is initially applied along the y axis [see Fig. 3.8 (a) and (c)]. In this case the conical spiral collapses into the flat state only at $\phi = 0$ or $\phi = \pi$ and only if $h < h_c^{(b)}$. For $h < h_c^{(b)}$, as shown in Fig. 3.8 (a) and (c), when ϕ is changed from 0 to $\pi/2$, $\hat{\mathbf{e}}(\mathbf{h})$ tilts from the z direction and increasingly acquires a positive x component. When ϕ is increased from $\pi/2$ to π the x component of $\hat{\mathbf{e}}(\mathbf{h})$ decreases and vanishes at $\phi = \pi$. Thus, as shown in Fig. 3.8(b), (d) and (c), $\mathbf{P}(\mathbf{h})$ rotates in the xz plane acquiring a positive component along z up to $\phi = \pi/2$ and then starts to rotates back towards the x direction. At $h > h_c^{(b)}$ the spiral is conical for all angles and the $\hat{\mathbf{e}}(\mathbf{h})$ follows the magnetic field.

3.4 General rules of magnetic manipulation of electric polarization in spirals

We now extend the discussion of Sec. 3.3 to the case of manipulation of flat spirals by a magnetic field constant in magnitude. We assume again that $\mathbf{h}$ is initially applied along $\mathbf{z}$ (normally to the xy spiral) and then its direction is rotated. Furthermore, we assume $\mathbf{q}||\mathbf{y}$[6]. As we discussed, the hierarchy of the anisotropy axes induces two scales in the magnetic field strength: the critical field $h_c^{(x)}$ and the critical field $h_c^{(y)} > h_c^{(x)}$. Therefore three different scenarios are possible depending on the value

[6]For different orientations of the wave vectors the evolution of P can be inferred from the evolution of $\hat{\mathbf{e}}$.

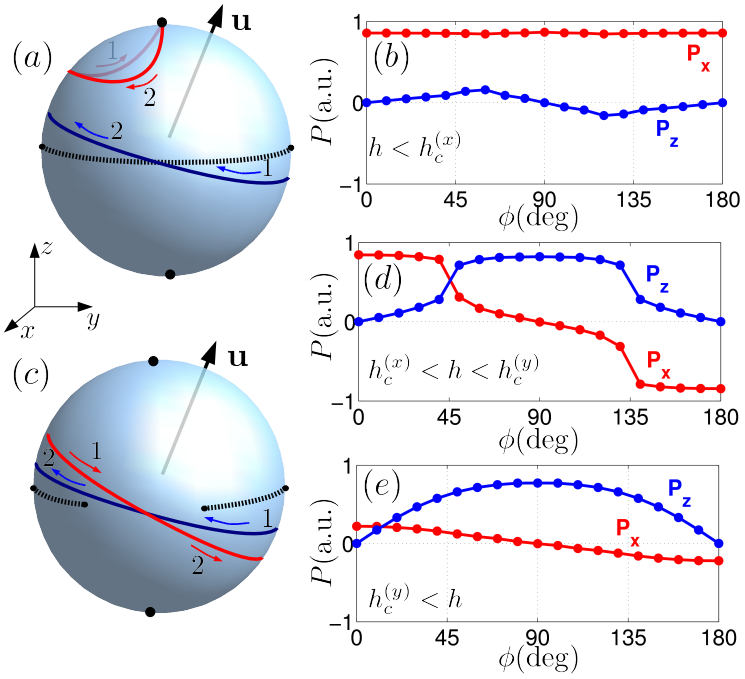

Figure 3.7: Sketch of the trajectories of the unit vector $\hat{\mathbf{e}}(\mathbf{h})$ (red lines) when the magnetic field (blue lines) of strength $h < h_c^x$ (a) and $h_c^{(x)} < h < h_c^{(y)}$ (c) is rotated around the axes $\mathbf{u}$ which is tilted by $\varrho = 10^\circ$ from $\hat{\mathbf{z}}$ in the yz plane. Evolution of electric polarization for the model described by Eq.(3.2) and Eq.(3.8) when as the applied magnetic field of strength $h < h_c^{(x)}$ (b), $h_c^{(x)} < h < h_c^{(y)}$ (d) and $h_c^{(y)} < h$ (e) is rotated.

of h.

For $h < h_c^{(x)}$ the stable state for field lying on the xy plane is a flat spiral with $\hat{\mathbf{e}}$ lying along the $\mathbf{z}$ axis. This case is not of extreme interest since modifying the direction of $\mathbf{h}$ slightly perturbs the original direction of $\hat{\mathbf{e}}$ and any path of $\mathbf{h}$ can invert the direction of $\mathbf{P}$.

For $h > h_c^y$ the stable state is a conical spiral everywhere and $\hat{\mathbf{e}}(\mathbf{h})$ approximately follows $\mathbf{h}$ in its path. Here, the original direction of electric polarization can be reversed by reversing the magnetic field: $\mathbf{P}(-\mathbf{h}) = -\mathbf{P}(-\mathbf{h})$. Here, however, it is not possible to reverse $\mathbf{P}$ by moving $\mathbf{h}$ along a close path.

The most interesting case is: $h_c^{(x)} < h < h_c^{(y)}$. Here, as shown inf Fig. 3.9 (a) and (b), whether a magnetic field applied in the xy plane deforms the flat spiral to a conical spiral or not depends on the angle that it forms with the y axis. Figure 3.9 shows the region Ω of angles where the minimal energy state is a flat spiral. The initial direction of $\hat{\mathbf{e}}$ and $\mathbf{P}$ can only be inverted by reversing the magnetic field through a path that does not cross Ω. If the direction of $\mathbf{h}$ crosses Ω during its inversion, $\hat{\mathbf{e}}$ and $\mathbf{P}$ return

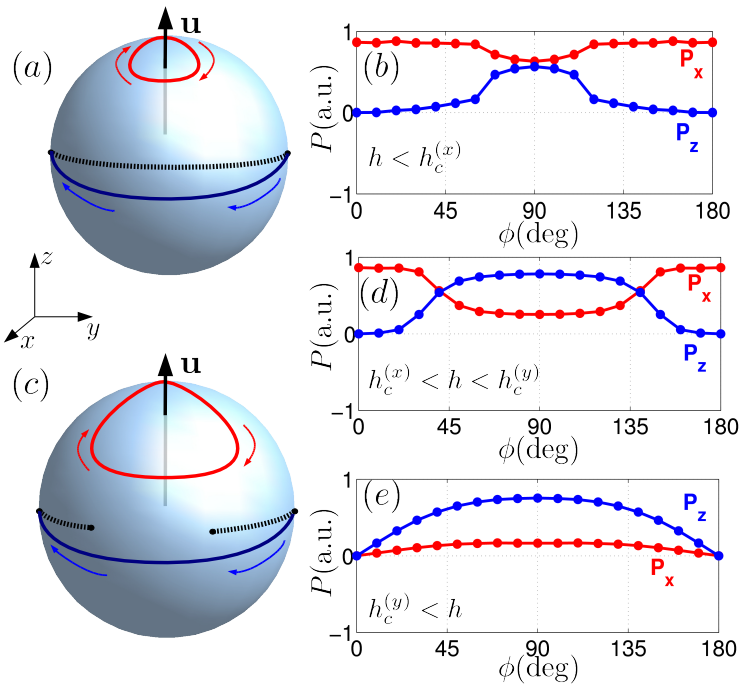

Figure 3.8: Sketch of the trajectories of the unit vector $\hat{\mathbf{e}}(\mathbf{h})$ (red lines) when the magnetic field (blue lines) of strength $h < h_c^x$ (a) and $h_c^{(x)} < h < h_c^{(y)}$ (c) is rotated around the axes $\mathbf{u}$ which is tilted by $\varrho = 10^\circ$ from $\hat{\mathbf{z}}$ in the xz plane. Evolution of electric polarization for the model described by Eq.(3.2) and Eq.(3.8) when as the applied magnetic field of strength $h < h_c^{(x)}$ (b), $h_c^{(x)} < h < h_c^{(y)}$ (d) and $h_c^{(y)} < h$ (e) is rotated.

to their original state. This behavior gives rise to a peculiar effect. In a close path the original state is restored if the magnetic field crosses an even number of times the region Ω [see Fig. 3.9 (a)], while $\hat{\mathbf{e}}_0$ and $\mathbf{P}$ are inverted if the crossing happens an odd number of times [see Fig. 3.9 (b)].

3.5 Conclusions

In conclusion, we studied theoretically the behavior of the electric polarization in spiral magnets in a rotating magnetic field, considering different types of anisotropies. As shown in Ref.[3], a magnetic field applied to helicoidal spirals states results in a cycloidal spiral component which induces electric polarization. Using a simple model of an anisotropic frustrated magnet, we show that at realistic values of the magnetocrystalline anisotropy strength the spiral distortion can be described by a simple Ansatz Eq.(3.4). We estimated the minimal value h_c of the magnetic field that allows the spiral's rotation axes to follow the magnetic field and obtained results that

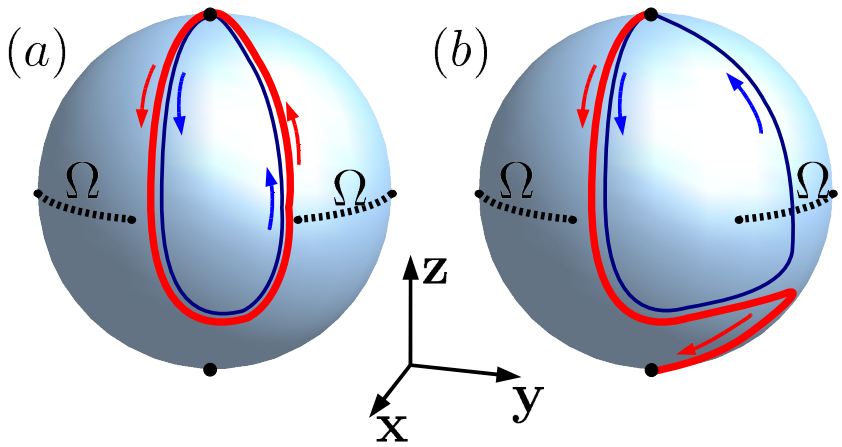

Figure 3.9: Pictorial view of two paths of the direction of **h** (blue curves) and $\hat{\mathbf{e}}(\mathbf{h})$ (red curves) for $h_c^{(a)} < h < h_c^{(c)}$ in the unit sphere. The equatorial black dashed curves represent the region Ω where the conical spiral collapses to the flat spiral state.

are in agreement with the experiment. The appearance of a cusp-like behavior of the electric polarization for field oriented approximately in the spiral plane is explained. We also considered a model of a cycloidal spiral magnet in the presence of an effective easy axis anisotropy along the y direction and intermediate axis anisotropy along the x direction. There, the condition for the inversion of the rotation axes of the spiral component $\hat{\mathbf{e}}$ strongly depends not only on the strength of the magnetic field but also on the axes around which the field is rotated. We finally considered the possibility of changing the spiral rotation direction and induced polarization along a closed path of a constant magnetic field on the sphere.

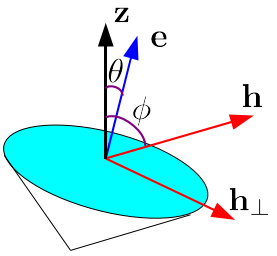

Figure 3.10: Schematic representation of the large component of the magnetic field $\mathbf{h}_\perp$ transverse to $\hat{\mathbf{e}}$ deforming the circular conical spiral.

3.A Appendix A: Correction to the circular spiral state

Here we justify the choice of Ansatz Eq.(3.4). This Ansatz originates from the assumption that the ground state is approximately a conical spiral with some distortions due to the presence of a magnetic field component in the spiral plane.
Figure 3.10 shows the circular conical spiral state in magnetic field forming an angle ϕ with the z axis in the xz plane. The axis $\hat{\mathbf{e}}$ around which the spins rotates forms an angle θ with the z axis. As shown in Fig. 3.3, for $h < h_c$, θ remains reasonably small for all values of ϕ and never exceeds $\pi/4$. When h is comparable to h_c, θ becomes large only at ϕ close to $\pi/2$. In all the regimes where $\theta \ll \phi$ a large component $\mathbf{h}_\perp = h\sin(\phi-\theta)\mathbf{u}_\perp$ of the field lies in the plane of the spiral component of the magnetic ordering [see Fig. 3.3]. Therefore, it is reasonable to assume that, in a large range of ϕ, the main correction to the circular conical spiral comes from the deformations due to the presence of $h_\perp$. Furthermore, for small θ, S_j^z do not deviate too much along the chain and the contribution of anisotropy to the corrections can be neglected.
The distortions to the spiral component $\mathbf{S}_\perp^{(0)}$ constrained in the $yu_\perp$ plane are:

$$S_j^\perp = \left(\sqrt{1-A^2} - \frac{\delta_j^2}{2}\right)(\cos(qj)\mathbf{y} + \sin(qj)\mathbf{u}_\perp) + \delta_j(\sin(qj)\mathbf{y} - \cos(qj)\mathbf{u}_\perp). \quad (3.9)$$

The main contribution of the distortions δ_j to $H_{exc} + H_h$ can be found using a similar argument to the one used in Appendix2.C. However, in this case the linear terms in δ_i comes from the coupling to $\mathbf{h}_\perp$:

$$\delta H_h = h_\perp \sum_{j=1}^{N} \delta_j \cos(qj). \quad (3.10)$$

In the Fourier space [see App.2.C] this correction becomes $\delta H_h = h_\perp Re\left(\delta_q\right)$. Therefore, to the lowest order in $h_\perp$, the magnetic field favors $\delta_j = \delta\cos(qj)$. Replacing δ_j in Eq.(3.9) and adding the uniform component one gets the Ansatz Eq.(3.4).

Bibliography

[1] Abe, N., Taniguchi, K., Ohtani, S., Takenobu, T., Iwasa, Y., and Arima, T. *Phys. Rev. Lett.* **99**(22), 227206 (2007).

[2] Kimura, T., Lawes, G., and Ramirez, A. P. *Phys. Rev. Lett.* **94**(13), 137201 (2005).

[3] Murakawa, H., Onose, Y., Ohgushi, K., Ishiwata, S., and Tokura, Y. *Journal of the Physical Society of Japan* **77**(4), 043709 (2008).

[4] Murakawa, H., Onose, Y., Kagawa, F., Ishiwata, S., Kaneko, Y., and Tokura, Y. *Phys. Rev. Lett.* **101**(19), 197207 (2008).

[5] Yokaichiya, F., Krimmel, A., Tsurkan, V., Margiolaki, I., Thompson, P., Bordallo, H. N., Buchsteiner, A., Stüßer, N., Argyriou, D. N., and Loidl, A. *Phys. Rev. B* **79**(6), 064423 (2009).

[6] Swendsen, R. H. and Wang, J.-S. *Phys. Rev. Lett.* **57**(21), 2607–2609 (1986).

[7] Earl, D. and Deem, M. W. *Phys. Chem. Chem. Phys.* **7**(23), 3910–3916 (2005).

[8] Enz, U. *Journal of Applied Physics* **32**(3), S22–S26 (1961).

[9] Kimura, T., Ishihara, S., Shintani, H., Arima, T., Takahashi, K. T., Ishizaka, K., and Tokura, Y. *Phys. Rev. B* **68**(6), 060403 (2003).

[10] Mochizuki, M. and Furukawa, N. *Phys. Rev. B* **80**(13), 134416 (2009).

[11] Aliouane, N., Prokhnenko, O., Feyerherm, R., Mostovoy, M., Strempfer, J., Habicht, K., Rule, K. C., Dudzik, E., Wolter, A. U. B., Maljuk, A., and Argyriou, D. N. *Journal of Physics: Condensed Matter* **20**(43), 434215 (2008).

[12] Yamasaki, Y., Miyasaka, S., Goto, T., Sagayama, H., Arima, T., and Tokura, Y. *Phys. Rev. B* **76**(18), 184418 (2007).

4

Microscopic theory of temperature-dependent magnetoelectric[1] effect in Cr_2O_3

In this chapter we calculate the temperature dependence of the linear magnetoelectric response of Cr_2O_3, starting by microscopic considerations. The microscopic coupling responsible for the magnetoelectric effect is determined by symmetry considerations and its strength is provided by *ab initio* calculations[2]. We use Monte Carlo and mean field approach to study the temperature dependence of the magnetoelectric susceptibility to magnetic field parallel to the spin direction ($\alpha_{\parallel}(T)$). The agreement between Monte Carlo results and experimental measurements makes this procedure a promising way for quantitative theoretical investigations of the temperature dependence of magnetoelectric effects.

4.1 Introduction

In Sec. 1.4 we discussed two types of microscopic mechanisms that allow magnetically ordered states to induce electric polarization and we classified them according to whether their origin comes from relativistic effects or not. Purely non-relativistic mechanisms, such as polar lattice distortions and polarization of electron clouds of

[1] This chapter is based on M. Mostovoy, A. Scaramucci, N.A. Spaldin and Kris T. Delaney, " Physical Review Letters **105**, 087202 (2010).

[2] The *ab initio* calculations were performed by N. Spaldin and K. Delaney, respectively, at the Materials Department and Materials Research Laboratory of the University of California Santa Barbara.

ions induced by Heisenberg (super)exchange interactions [1], originate from Fermi statistics of electrons, while mechanisms, such as inverse Dzyaloshinskii-Moriya interaction [2; 3; 4; 5], originate from the relativistic coupling between spin and orbital momentum of electrons. Since relativistic effects are relatively weak in magnetic $3d$ transition metal ions, the resulting electric polarization is typically 1-2 orders of magnitude smaller than the polarization induced by superexchange [1; 6]. In this chapter we show that, in addition to causing multiferroic behavior, the Heisenberg exchange mechanism can also give rise to the linear magnetoelectric effect in magnetoelectric collinear antiferromagnets.

In collinear antiferromagnets, when a magnetic field is applied longitudinally to the spin ordering, its competition with the magnetocrystalline anisotropy requires a minimal strength h_c to deform the magnetic ordering in the lowest energy state[3], i.e. to flop the spins. Therefore, since the magnetoelectric coupling induced by superexchange depends on scalar products of spins, for collinear antiferromagnets at zero temperature, one expects the magnetoelectric effect for magnetic field parallel to the spins to vanish together with the longitudinal susceptibility. At nonzero temperatures the longitudinal magnetic susceptibility is nonzero due to thermal spin fluctuations, which allows exchange interactions to contribute to the linear magnetoelectric effect. Indeed, in many magnetoelectrics with collinear magnetic orders the corresponding components of the magnetoelectric tensor strongly decrease with decreasing temperature [7; 8; 9; 10].

In this chapter, we calculate the temperature dependent magnetoelectric response, $\alpha_{\parallel}$, of the prototype magnetoelectric material, Cr_2O_3, using the results of first-principle calculations (obtained by our co-workers) and Monte Carlo methods. We show that the strong finite-temperature magnetoelectric response originates from the Heisenberg mechanism combined with thermal spin fluctuations, whereas at zero temperature, where spin fluctuations vanish, the observed weak response arises from relativistic effects.

In the first section of this chapter, after a brief discussion of the observed temperature dependence of the magnetoelectric tensor of Cr_2O_3, we introduce the magnetoelectric coupling and describe our spin model. Next we calculate the temperature dependence of $\alpha_{\parallel}$ using a mean field approach. In the last section we discuss the Monte Carlo calculations performed to include the effect of thermal fluctuations and the agreement of our results with experiment measures.

4.2 Microscopic model

The crystal structure, the symmetry group and the magnetic ordering of chromium sesquioxide, Cr_2O_3, were discussed in Chapter 1 and, throughout this chapter, we will use the same notation for the axes and the Cr ions in the crystallographic unit cell shown in Fig. 1.1. In the antiferromagnetic state of Cr_2O_3 the spins are oriented along the trigonal axis z. As was discussed in Sec. 1.1, the symmetry analysis gives

[3] Here we neglect quantum fluctuations.

	3_z	2_x	I
1	1	2	4
2	2	1	3
3	3	$4-c$	2
4	4	$3-c$	1

Table 4.1: Transformation of Cr sites under the generators of the $R\bar{3}c$ symmetry group [see Section 1.1]. Here $\mathbf{c} = \mathbf{a}_1 + \mathbf{a}_2 + \mathbf{a}_3$, where $\mathbf{a}_i$ ($i = 1, 2, 3$) are the rhombohedral unit vectors.

the phenomenological form of the magnetoelectric coupling [11]:

$$f_{\text{me}} = -g_{\parallel} G_z E_z H_z - g_{\perp} G_z \left(E_x H_x + E_y H_y \right), \tag{4.1}$$

where **G** is the antiferromagnetic order parameter (also described in sec. 1.1), **H** and **E** are, respectively, the static magnetic and electric field, $g^{\parallel}$ and $g^{\perp}$ are the coupling constants and the xy plane is perpendicular to z. However, this type of analysis does not give insights into magnitudes of the two magnetoelectric coefficients, $\alpha_{\parallel} = g_{\parallel} G_z$ and $\alpha_{\perp} = g_{\perp} G_z$.
Experimentally, the ratio of $\alpha_{\parallel}$ and $\alpha_{\perp}$ shows a remarkably strong temperature dependence [7]. While the temperature dependence of $\alpha_{\perp}$ is similar to that of the order parameter G_z, the coefficient $\alpha_{\parallel}$ reaches maximum at $T_{\text{max}} \sim 260$K, where it is one order of magnitude larger than $\alpha_{\perp}$. Below T_{max}, $\alpha_{\parallel}$ steeply decreases with decreasing temperature, changes sign and becomes smaller than $\alpha_{\perp}$. Old experimental measurements of temperature dependence of the magnetoelectric coefficients [12; 13; 14] as well as recent first-principle calculations [15] show that the relatively weak magnetoelectric effects observed at low temperatures result from relativistic interactions, while the relatively large $\alpha_{\parallel}$ near $T_{\text{max}} \sim 260$K is likely to originate from non-relativistic interactions, such as the lattice striction driven by Heisenberg superexchange.

4.2.1 Magnetoelectric coupling

Superexchange interactions between spins of transition metal ions depend on relative positions of metal and ligand ions. Conversely, positions of ions are affected by spin ordering, which induces an electric polarization, **P**, if the magnetic ordering breaks inversion symmetry. As discussed in Sec. 1.4.1 this polarization is linearly coupled to the scalar products of spins. Moreover, since we are interested only in the linear magnetoelectric effect resulting from magnetic field collinear to the spins and coupled to E_z, we restrict ourself to the analysis of the coupling between the z component of **P** and the spins' scalar products.
The form of the microscopic magnetoelectric coupling has to be invariant under the symmetry operations of the crystal. Since the polar distortions are coupled to the scalar product of the spins, the spin transformation properties are irrelevant and all the information necessary to find the form of the magnetoelectric coupling is contained in Table 4.1, which shows the transformations of the four magnetic sublattice under the generators of $R\bar{3}c$. To guarantee the invariance of the Hamiltonian under these transformations one has to find a term linear in the scalar product of spins that

transforms as P^z. Phenomenologically, the electric polarization P^z along the trigonal axis can couple to spins as follows:

$$P^z = \lambda \left(\mathbf{S}_1 \cdot \mathbf{S}_3 - \mathbf{S}_2 \cdot \mathbf{S}_4 \right), \tag{4.2}$$

where $\mathbf{S}_i$ with $i = 1, 2, 3, 4$ denotes the sublattice magnetization and λ is the coupling strength. As it can be seen by inspection of Tab. 4.1, the combination of scalar products in the right-hand-side Eq.(4.2) transforms in the same way as P^z.
Equation (4.2) is only meaningful within the mean field approach. To account for effects of spin fluctuations on the magnetoelectric response of Cr_2O_3 we will use the microscopic model described by the Hamiltonian

$$H = H^M + \mu \sum_{k=1}^{6} \sum_i \left[P^z_{i,i+\mathbf{b}_k} (\mathbf{S}_{1,i} \cdot \mathbf{S}_{3,i+\mathbf{b}_k} - \mathbf{S}_{2,i} \cdot \mathbf{S}_{4,i+\mathbf{b}_k}) + \frac{\Delta}{2} (P^z_{i,i+\mathbf{b}_k})^2 \right], \tag{4.3}$$

where H^M is the purely magnetic part of the Hamiltonian, $P^z_{i,i+\mathbf{b}_k}$ is the electric polarization induced by the exchange interactions between the i-th and the $i + \mathbf{b}_k$-th unit cell, Δ is the spring constant related to the correspondent polar mode, μ is the microscopic coupling constant and $\mathbf{b}_1 = \mathbf{a}_1$, $\mathbf{b}_2 = \mathbf{a}_2$, $\mathbf{b}_3 = \mathbf{a}_3$, $\mathbf{b}_4 = \mathbf{a}_1 + \mathbf{a}_2$, $\mathbf{b}_5 = \mathbf{a}_2 + \mathbf{a}_3$, $\mathbf{b}_6 = \mathbf{a}_1 + \mathbf{a}_3$.
Minimizing r.h.s. Eq.(4.3) with respect to $P^z_{i,i+b_k}$ one gets the total polarization ,

$$P^z = \frac{\lambda}{6N} \sum_i \sum_{k=1}^{6} (\mathbf{S}_{1,i} \cdot \mathbf{S}_{3,i+\mathbf{b}_k} - \mathbf{S}_{2,i} \cdot \mathbf{S}_{4,i+\mathbf{b}_k}), \tag{4.4}$$

where $\lambda = \frac{\mu}{\Delta}$ and N is the total number of unit cells. As we discussed in Sec. 1.1, the magnetization induced by an applied electric field is extremely small. This means that the magnetoelectric coupling in Eq.(4.3), which has a much smaller strength than the energy scale of spin-spin interactions, affects negligibly the spin degrees of freedom compared to the interactions in H^M.
The phenomenological expression Eq.(4.2) can be used to clarify the temperature dependence of $\alpha_{\parallel}$ by the following heuristic argument. States with the magnetization of even sublattices opposite to the magnetization of odd sublattices, i.e. the $\uparrow\downarrow\uparrow\downarrow$ magnetic ordering, do not induce electric polarization. Consider now the magnetic order to be of the type $\uparrow\downarrow\uparrow\downarrow$ and magnetic moments to be oriented along the z direction. At non-zero temeperatures, a magnetic field applied in the positive z direction increases (decreases) the thermal average of the spins of ions in the odd (even) sublattices. Therefore, it induces a nonzero electric polarization. As the difference between the magnetization of even and odd sublattices is proportional to the magnetic susceptibility χ^{zz}, P^z Eq.(4.4) must vanish at zero temperature where $\chi^{zz} = 0$.
The previous argument makes the calculation of the coupling constant λ by *ab initio* methods non trivial. The density-functional study of Cr_2O_3 cannot give any information about the strength of the part of magnetoelectric coupling because the part of $\alpha_{\parallel}$ induced by Heisenberg exchange striction vanishes at $T = 0$. However, it is possible to overcome this problem by the following consideration. Equation (4.4)

coupling	exchange pathway	values	number of neighbors
J_1	$1 \leftrightarrow 2\ (3 \leftrightarrow 4)$	12.17 meV	1
J_2	$1 \leftrightarrow 4 - b_j\ (2 \leftrightarrow 3 - b_k)$	10.12 meV	3
J_3	$1 \leftrightarrow 2 - b_k\ (3 \leftrightarrow 4 - b_k)$	-1.97 meV	3
J_4	$1 \leftrightarrow 3 - b_k\ (2 \leftrightarrow 4 - b_k)$ $1 \leftrightarrow 3 - b_j\ (2 \leftrightarrow 4 - b_j)$	-1.70 meV	6
J_5	$2 \leftrightarrow 3\ (1 \leftrightarrow 4 - \mathbf{a}_1 - \mathbf{a}_2 - \mathbf{a}_3)$	2.10 meV	1

Table 4.2: Coupling constants and exchange path used in model Eq.(4.6) where $\mathbf{b}_1 = \mathbf{a}_1$, $\mathbf{b}_2 = \mathbf{a}_2$, $\mathbf{b}_3 = \mathbf{a}_3$, $\mathbf{b}_4 = \mathbf{a}_1 + \mathbf{a}_2$, $\mathbf{b}_5 = \mathbf{a}_2 + \mathbf{a}_3$, $\mathbf{b}_6 = \mathbf{a}_1 + \mathbf{a}_3$., $k = 1, 2, 3$ and $j = 4, 5, 6$. Interactions with the same coupling constant can be obtained transforming the indexes according to Table 4.1.

applies to any type of sublattice spin ordering; therefore, the magnetic state $\uparrow\uparrow\uparrow\downarrow$ has spontaneous electric polarization,

$$\mathcal{P} \equiv P(\uparrow\uparrow\uparrow\downarrow) = 2\lambda S^2 \tag{4.5}$$

and is multiferroic. Thus, the calculation of λ using *ab initio* methods is possible if one enforces the magnetic state $\uparrow\uparrow\uparrow\downarrow$ [see Fig. 4.1 (b)] and calculates the value of $\mathcal{P}$. Such a type of calculations were performed by N. Spaldin and K. Delaney [16] and gave $\frac{\mathcal{P}}{v_0} = 0.585\mu\mathrm{C/cm}^2$, where v_0 is the volume of the crystallographic unit cell. In those calculation the spin-orbit interaction was explicitly omitted in order to ensure the pure exchange-striction origin of electric polarization.

4.2.2 Exchange Hamiltonian

We now discuss the magnetic part of the Hamiltonian Eq.(4.3). For the purely spin part of Eq.(4.3) we consider the Heisenberg Hamiltonian of classical spins in the presence of a magnetic field **H** applied along the z direction:

$$\mathcal{H}_M = \sum_{i,j} \sum_{\mathbf{r},\mathbf{r}'} J_{i,j}(\mathbf{r} - \mathbf{r}') \left(\mathbf{S}_{i,\mathbf{r}} \cdot \mathbf{S}_{i,\mathbf{r}'}\right) - g\mu_B H^z \sum_{\mathbf{r}} \sum_{j} S^z_{j,\mathbf{r}'} \tag{4.6}$$

where $i, j = 1, 2, 3, 4$ label the magnetic sublattices, $\mathbf{r}$ and $\mathbf{r}'$ are positions of the crystallographic unit cells, $\mathbf{S}_{j,\mathbf{r}}$ (with $S_{j,\mathbf{r}} = 3/2$) are the spins of Cr^{3+} ions, g_μ is the gyromagnetic ratio and μ_B is the Bohr magneton. Here S^z_i is the component of the i-th spin along the axis $z||\mathbf{a}_1 + \mathbf{a}_2 + \mathbf{a}_3$. The exchange couplings $J_{i,j}(\mathbf{r} - \mathbf{r}')$ were obtained by our collaborators using *ab initio* calculations. We considered couplings between spins of Cr ions up to the fifth nearest neighbor. The (super)exchange pathways and the strength of the couplings are reported in Tab. 4.2.
The antiferromagnetic coupling constants J_1, J_2, J_5 and the ferromagnetic one J_4 [see Tab. 4.2] favor the $\uparrow\downarrow\uparrow\downarrow$ type spin ordering. The relatively weak coupling constant J_3 favors a ferromagnetic alignment of the spins of the odd and even sublattices and frustrates the spin ordering. The weakness and the small coordination number

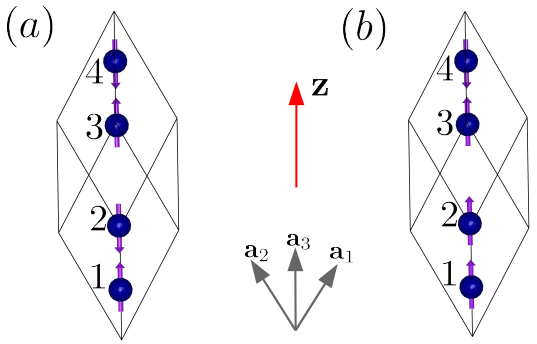

Figure 4.1: The rhombohedral unit cell of Cr_2O_3 with the unit vectors $\mathbf{a}_i$ $(i = 1,2,3)$ contains four magnetic Cr ions. The Cr sites have the fractional coordinate: $\mathbf{r}_1 = (u,u,u)$, $\mathbf{r}_2 = (1/2-u,1/2-u,1/2-u)$, $\mathbf{r}_3 = (1/2+u.1/2+u,1/2+u)$ and $\mathbf{r}_4 = (1-u,1-u,1-u)$ and are alligned along the z axis ($\mathbf{z} \parallel \mathbf{a}_1+\mathbf{a}_2+\mathbf{a}_3$) The antiferromagnetic state of Cr_2O_3 (a) and the imposed multiferroic state (b) used to obtain the magnetoelectric coupling by *ab initio* calculations. The numbers refers to the labels of the magnetic sublattices. In the hexagonal setting the hexagonal planes are perpendicular to z.

[see Tab. 4.2] of this coupling do not allow this interaction to induce non collinear ordering, however, as will be shown below, its presence enhances the effect of thermal fluctuations.
In Eq.(4.6) we neglect anisotropy terms. This is justified by their small strength compared to the relatively large exchange coupling constant listed in Tab.4.2 and by the reported experimental difficulties on poling Cr_2O_3 in a single magnetic domain [17]. One might argue that in absence of such anisotropy an arbitrary small magnetic field would immediately flop the spins. However, in the following calculations, we assume the magnetic order parameter to be oriented only in one direction (for the mean-field case) or we calculate the strength of $\alpha_\parallel$ from the fluctuations at $\mathbf{H} = 0$ (for the Monte Carlo case).

4.3 Mean-field calculation of $\alpha_\parallel(T)$

In this section we discuss the mean-field calculation of $\alpha_\parallel$ of the model Eq.(4.3) which gives a qualitatively good description of temperature dependence observed in Cr_2O_3. Collinear magnetic orders of a system with four spins in the magnetic unit cell are conveniently described using the 4×4 matrix $\mathcal{I}$, whose matrix element $\mathcal{I}_{ij}$ equals the sum of the exchange constants, $J_{i,j}(\mathbf{r}-\mathbf{r}')$, relative to the interactions between an arbitrary spin from the sublattice i of the unit cell at $\mathbf{r}$ and all spins from the sublattice j of the same unit cell and the neighboring ones (labeled by $\mathbf{r}'$). The resulting matrix has to be symmetric $I_{\beta\alpha} = I_{\alpha\beta}$ since $J_{i,j}(\mathbf{b}_k) = J_{j,i}(-\mathbf{b}_\mathbf{k})$. Furthermore, the invariance under transformations listed in Tab.4.2 imposes $I_{11} = I_{22} = I_{33} = I_{44}$, $I_{23} = I_{14}$,

$I_{24} = I_{13}$, and $I_{34} = I_{12}$. Therefore, the matrix $I_{\alpha\beta}$ can be written in the form:

$$\mathcal{I} = \begin{bmatrix} I_{11} & I_{12} & I_{13} & I_{14} \\ I_{12} & I_{11} & I_{14} & I_{13} \\ I_{13} & I_{14} & I_{11} & I_{12} \\ I_{14} & I_{13} & I_{12} & I_{11} \end{bmatrix}. \tag{4.7}$$

The four eigenvectors of this matrix correspond to the four type of magnetic orders introduced by Bertaut [18]:

$$F = \begin{pmatrix} 1 \\ 1 \\ 1 \\ 1 \end{pmatrix},\ G = \begin{pmatrix} 1 \\ -1 \\ 1 \\ -1 \end{pmatrix},\ A = \begin{pmatrix} 1 \\ 1 \\ -1 \\ -1 \end{pmatrix},\ C = \begin{pmatrix} 1 \\ -1 \\ -1 \\ 1 \end{pmatrix}. \tag{4.8}$$

It is worth to notice that according to the magnetoelectric coupling Eq.(4.4) none of the collinear states represented by these eigenvectors is multiferroic. Moreover, for the case where the spin ordering is homogeneous (wave vector $\mathbf{q} = 0$), the eigenvector of the matrix $\mathcal{I}$ relative to its lowest eigenvalue corresponds to the spin ordering in the ground state.
The eigenvalues relative to the eigenvectors Eq.(4.8) are

$$\begin{array}{rcl} \lambda_F &=& I_{11} + I_{12} + I_{13} + I_{14}, \\ \lambda_G &=& I_{11} - I_{12} + I_{13} - I_{14}, \\ \lambda_A &=& I_{11} + I_{12} - I_{13} - I_{14}, \\ \lambda_C &=& I_{11} - I_{12} - I_{13} + I_{14}, \end{array} \tag{4.9}$$

and, from the exchange interactions listed in Tab.4.2, which gives $I_{11} = 0$, $I_{12} = J_1 + 3J_3$, $I_{13} = 6J_4$ and $I_{14} = 3J_2 + J_5$, we get $\lambda_G = -48.92$ meV, $\lambda_A = -16$ meV, $\lambda_F = 28.52$ meV and $\lambda_C = 36.4$ meV . Since the magnetic order is homogeneous, the minimal energy state of the exchange Hamiltonian is collinear and of the G-type [4] which is consistent with the well know magnetic structure of Cr_2O_3. To be consistent with experiments and the phenomenological description, in what follows we assume this spin order to be oriented along the z direction.
Let us now calculate the magnetoelectric response in the mean-field approximation in which the scalar products $\mathbf{S}_{i,\mathbf{r}} \cdot \mathbf{S}_{j,\mathbf{r}}$ in Eq.(4.6) are replaced by $\langle \mathbf{S}_{i,\mathbf{r}} \rangle \cdot \mathbf{S}_{j,\mathbf{r}'} + \mathbf{S}_{i,\mathbf{r}} \cdot \langle \mathbf{S}_{j,\mathbf{r}'} \rangle$, where $\langle \dots \rangle$ indicates the average value. Consider first the case $H = 0$. Since the magnetic ordering is homogeneous and G-type, one can write $\langle \mathbf{S}_{i,\mathbf{r}} \rangle_0 = G_i \langle \mathbf{S} \rangle_0$, where the subscripts indicates the absence of magnetic field. The mean field acting on the spin $\mathbf{S}_{i,\mathbf{r}}$ in model Eq.(4.6) is

$$\mathbf{h}^0_{i,\mathbf{r}} = \sum_j \sum_{\mathbf{r}'} J_{i,j}(\mathbf{r} - \mathbf{r}') \langle \mathbf{S}_{j,\mathbf{r}'} \rangle_0 = \sum_j \mathcal{I}_{i,j} G_j \langle S \rangle_0 \mathbf{z} \equiv \lambda_G G_j \langle S \rangle_0 \mathbf{z}. \tag{4.10}$$

[4] Here "G-type" refers to the antiferromagnetic setting relative to the eigenvector **G** in Eq. 4.8. It should not be confused with the G-type antiferromagnetic ordering occuring, for instance, in orthorombic perovskites.

Note that $\mathbf{h}^0_{i,\mathbf{r}} = \mathbf{h}^0_i$ is independent on the unit cell position $\mathbf{r}$. The average value of the spins along z can be found self-consistently by

$$\langle S_i\rangle_0 \equiv G_i\langle S\rangle_0 \equiv \frac{\int d\mathbf{S}\left(S^z e^{-\beta\mathbf{h}_\mu\cdot\mathbf{S}}\right)}{\int d\mathbf{S} e^{-\beta\mathbf{h}_\mu\cdot\mathbf{S}}} = G_i L(\beta S|h_i|) \equiv G_i L(z(T)), \tag{4.11}$$

where $\beta = \frac{1}{k_B T}$, $z(T) = \beta S|h_i| = \beta S\lambda_G\langle S\rangle_0$ and $L(x) = \coth(x) - \frac{1}{x}$ is better known as Langevin function[5]. The mean-field value of the Néel temperature for classical spins, $T_N^{MF} = \frac{\lambda_G S^2}{3}$, is determined by the lowest temperature at which Eq.(4.11) has non-zero solutions and for the values in Tab. 4.2 is 425 K.
We turn now to the case of a magnetic field, **H**, applied along z. An arbitrary small strength of this field admixes the G-type of order with a tiny ferromagnetic component (F-type). To the lowest order in H^z, the average values of the spins become $\langle S_i^z\rangle = G_i\langle S_i^z\rangle_0 + xF_i$ while the mean field acting one the spin $S_{i\mathbf{r}}$ becomes $h_i^z = G_i h^0 + yF_i \equiv G_i(h^0 + yG_i)$. From the equation of the effective field acting on the spin $S_{i,\mathbf{r}}$: $h_i = -\sum_j I_{ij}\langle S_j\rangle + g\mu_B H$ one recovers Eq.(4.10) plus the additional equation for the ferromagnetic component:

$$y = -\lambda_F x + g\mu_B H. \tag{4.13}$$

The self-consistent equation Eq.(4.11) then becomes

$$\langle S_i\rangle = G_i L\left(z(T) + yG_i\beta S\right) \simeq G_i L(z(T)) + F_i\beta S y L'(z(T)), \tag{4.14}$$

where $L'(x) = \partial_x L(x)$, and in the last step we kept the term up to the linear order in H. Combining the last two equations we get the size of the ferromagnetic component,

$$x = \frac{g\mu_B S H}{k_B T}\frac{L'(z(T))}{1 + \beta\lambda_F S L'(z(T))}. \tag{4.15}$$

and, thus, the magnetization $M^z = \frac{\sum_i\sum_{\mathbf{r}} S^z_{i\mathbf{r}}}{V} = \frac{4g\mu_B x}{v_0}$, where V is the total volume and v_0 is the volume of the unit cell.
From Eq.(4.4) one gets:

$$P^z = 4\lambda\langle S\rangle_0 x \equiv \frac{\lambda v_0}{g\mu_B}\langle S\rangle_0 M^z \tag{4.16}$$

[5]The same calculation for quantum spins gives

$$G_\mu\langle S\rangle_0 \equiv \frac{Tr\left(\mathbf{S}e^{-\beta\mathbf{h}_\mu\cdot\mathbf{S}}\right)}{Tr\left(e^{-\beta\mathbf{h}_\mu\cdot\mathbf{S}}\right)} = B_S(\beta S\lambda_G\langle S\rangle_0), \tag{4.12}$$

where $B_S(x) = \left(1 + \frac{1}{2S}\right)\coth\left(\left(1 + \frac{1}{2S}\right)x\right) - \frac{1}{2S}\coth\left(\frac{x}{2S}\right)$ are known as Brillouin functions.

where λ can be estimated using the *ab initio* calculation and Eq.(4.5). Therefore, in the mean field approximation the polarization induced by a tiny magnetic field is proportional to the product of the order parameter and the induced magnetization. Similarly, the component of the magnetoelectric tensor relative to longitudinal magnetic fields,

$$\alpha_{\parallel} \equiv \left.\frac{\partial P^z}{\partial H^z}\right|_{H=0} = \frac{\lambda v_0}{g\mu_B}\langle S\rangle_0 \chi^{zz}, \tag{4.17}$$

is proportional to the product of the order parameter and the longitudinal magnetic susceptibility χ^{zz}. This qualitatively explains the observed temperature dependence of $\alpha_{\parallel}$. As shown in Fig.4.3, the mean-field value of $\alpha_{\parallel}$ first grows together with the order parameter as the temperature is decreased from T_N^{MF}. Then, it starts decreasing and vanishes at $T = 0$ together with χ^{zz}. Although Eq.(4.17) catches the physics behind the temperature dependence of $\alpha_{\parallel}$, for quantitative comparison one needs to take in account the effect of thermal fluctuations.

4.4 Monte Carlo calculation of $\alpha_{\parallel}(T)$

We now discuss the way in which a more quantitative comparison can be achieved by using Monte Carlo simulations. To include the effect of thermal fluctuation on $\alpha_{\parallel}$, we performed Monte Carlo simulations on a lattice of classical spins $\mathbf{S}_{i,\mathbf{r}}$ with the Hamiltonian Eq.(4.6) using the coupling constants given in Tab. 4.2. The following results were obtained considering a $6 \times 6 \times 6$ unit cells lattice with periodic boundary conditions applied to all the crystallographic directions.
Since in model Eq.(4.6) we neglect magnetocrystalline anisotropies, domains with all the possible orientations of **G** are degenerate. The large degeneracy, together with the finite size of the simulated spin lattice, allows the direction of the order parameter to rotate during the Monte Carlo evolution, making it challenging to calculate thermal averages of vectorial quantities. To overcome this problem we added to Eq.(4.6) a term $H_s = h_g \sum_{j,\mathbf{r}} (-1)^j S^z_{j,\mathbf{r}}$ containing the coupling of spins to a tiny staggered field of strength h_g oriented along the trigonal axes z. Staggered fields of strength $h_g \sim \frac{k_B T}{4NS} \ll \frac{J_{min}}{S}$, where J_{min} is the smallest exchange constant, stabilize the domain with order parameter oriented along z without appreciably affecting thermal averages.
For **G** oriented along z, the longitudinal magnetoelectric susceptibility is:

$$\alpha_{\parallel} \equiv \left.\frac{\partial \langle P^z\rangle}{\partial H_z}\right|_{H_z=0} = \frac{2\mu_B}{k_B T}\langle P^z \sum_{j,\mathbf{r}} S^z_{j\mathbf{r}}\rangle, \tag{4.18}$$

where we consider the gyromagnetic factor $g = 2$. As for the case of mean-field calculations, the constant λ in Eq.(4.4) can be extracted from the value $\mathcal{P}$ of the electric polarization in the $\uparrow\uparrow\uparrow\downarrow$ state: $\lambda = \frac{\mathcal{P} v_0}{2S^2}$, where v_0 is the volume of the unit cell.
To check that the staggered field stabilizes one antiferromagnetic domain without

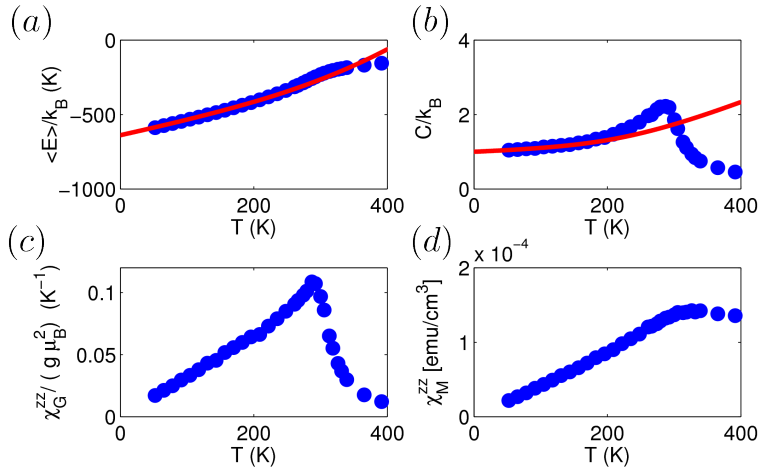

Figure 4.2: Temperature dependence of thermodynamic properties model Eq.(4.6). (a) Average energy of obtained by Monte Carlo simulations (blue dots) and ϵ^{MF} (red line). (b) Monte Carlo values (blue dots) and mean field values of magnetic specific heat. (c) and (d) show, respectively, the Monte Carlo values of the susceptibility of the order parameter to staggered field applied along the z direction $\chi^{zz}_G = \frac{\langle (G^z)^2 \rangle - \langle G^z \rangle^2}{T}$ and the longitudinal magnetic susceptibility χ^{zz}_M.

affecting sensibly $\alpha_{\parallel}(T)$, we performed Monte Carlo simulations[6] for various values of h_g at $T \approx 208$ K. Figures 4.3 (a) and (b) show, respectively, the dependence of the antiferromagnetic order parameter and of $\alpha_{\parallel}$ on h_g. For 0.1 meV $\lesssim h_g \lesssim$ 0.25 meV the magnetoelectric susceptibility shows a plateau while the G^z does not vary sensibly. This indicates that fields' strength in such interval can be use to stabilize the antiferromagnetic order along the z direction.
Figure 4.2 shows the temperature dependence of some of the thermodynamic quantities obtained by Monte Carlo simulations at $h_g = 0.165$ meV. At $T_N^{MC} = 290$ K the magnetic specific heat [see Fig.4.2 (b)] and the staggered susceptibility, $\chi^{zz}_g = \frac{\partial G^z}{\partial h^z_g}$, [see Fig.4.2 (c)] show a sharp peak indicating the antiferromagnetic transition. The significant difference between T_N^{MC} and the calculated mean field transition temperature, $T_N^{MF} = 425$ K, underlines the crucial role of thermal fluctuations, which are enhanced by the small frustration induced by the ferromagnetic interactions with exchange constant J_3 [see Table 4.2].
The Monte Carlo results for r.h.s. of Eq.(4.18) and the mean-field results for $\alpha_{\parallel}(T)$ are shown in Fig. 4.3(c). At temperatures just below T_N^{MC} the mean field results largely overestimate the value of $\alpha_{\parallel}$, while at low temperatures ($T \lesssim 180$ K) they agree remarkably with Monte Carlo results. The maximal value of $\alpha_{\parallel}$, obtained at $T \approx 250$

[6] These calculations were performed considering $J_5 = 0$. However, due to its tiny strength and the small number of neighbors, the coupling corresponding to J_5 weakly affects $\alpha_{\parallel}$, its maximum as a function of T and the antiferromagnetic transition temperature.

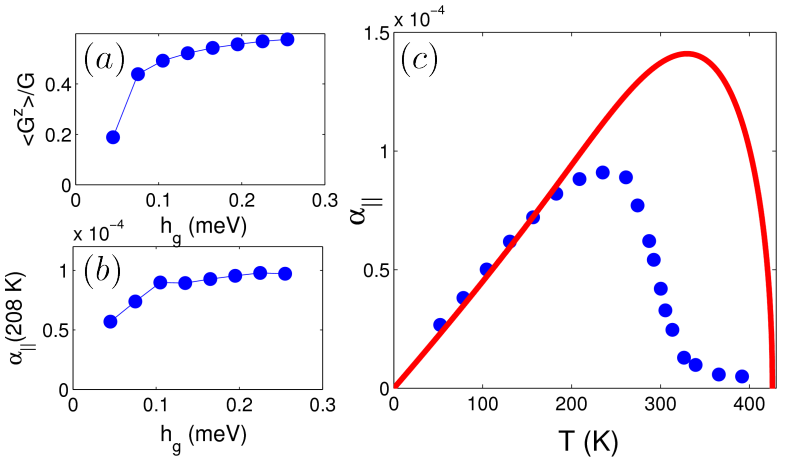

Figure 4.3: Dependence of the antiferromagnetic order parameter (a) and $\alpha_{\parallel}$ on the strength h_g of the staggered field introduced to stabilize on magnetic domain. (c) Temperature dependence of the magnetoelectric susceptibility $\alpha_{\parallel}$ obtained using Monte Carlo for the *ab initio* values of the exchange constants [see Tab.4.2] and magnetoelectric coupling (blue circles) compared to the mean-field result (solid red line).

K, is $0.9 \cdot 10^{-4}$ in Gaussian units, and it is in good agreement with the experimental values [19].

4.5 Conclusions and remarks

We presented the first *ab initio* calculation of temperature-dependent magnetoelectric response. We calculated the contribution to $\alpha_{\parallel}$ coming from non-relativistic interactions between spins and polarization. Using symmetry analysis, we obtained the form of such a coupling. While the calculation of the coupling strength is non-trivial for the antiferromagnetic state of Cr_2O_3, it can be achieved by enforcing a multiferroic state. This calculation was performed by our co-workers using *ab initio* methods, which also allows for the computation of the exchange constants. We first estimated $\alpha_{\parallel}(T)$ using mean-field approximation and we obtained a qualitative agreement with the experimentally observed behavior. Then we went beyond mean-field by using Monte Carlo techniques. The results of our simulations are in good agreement with the experimental results, proving that the strong temperature dependence and a relatively large maximal value of this magnetoelectric coefficient originates from non-relativistic exchange mechanisms of magnetoelectric coupling. The same mechanism is responsible for linear magnetoelectric effect also in other collinear magnets, such as Fe_2TeO_6 [9], $Ga_{2x}Fe_xO_3$ [8] or Ti_2O_3 [10], which, remarkably, show a similar temperature dependence of $\alpha_{\parallel}$.
The approach used for this study, i.e. the combination of symmetry considerations,

first principle calculations and Monte Carlo simulations, opens a new route to the theoretical investigation of the temperature dependence of magnetoelectric effects and to the design of magnetoelectric materials where the exchange-driven coupling is the dominant mechanism. Furthermore, Eqs.(4.16) and (4.18), which relate the polarization in the multiferroic state to the magnetoelectric coefficient in the magnetoelectric state, reflect the common origin of the electric polarization induced by exchange striction in collinear multiferroics ($P \approx 0.1 - 1\mu\mathrm{C/cm}^{-2}$) and the magnetoelectric effect with $\alpha \sim 10^{-4} - 10^{-3}$ in Gaussian units.

Bibliography

[1] Sergienko, I. A., Şen, C., and Dagotto, E. *Phys. Rev. Lett.* **97**(22), 227204 Nov (2006).

[2] Katsura, H., Nagaosa, N., and Balatsky, A. V. *Phys. Rev. Lett.* **95**(5), 057205 Jul (2005).

[3] Sergienko, I. A. and Dagotto, E. *Phys. Rev. B* **73**(9), 094434 Mar (2006).

[4] Mostovoy, M. *Phys. Rev. Lett.* **96**(6), 067601 Feb (2006).

[5] Malashevich, A. and Vanderbilt, D. *Phys. Rev. Lett.* **101**(3), 037210 Jul (2008).

[6] Picozzi, S., Yamauchi, K., Sanyal, B., Sergienko, I. A., and Dagotto, E. *Phys. Rev. Lett.* **99**(22), 227201 Nov (2007).

[7] Astrov, D. N. *Sov. Phys. JETP* **11**, 708 (1961).

[8] Popov, Y., Kadomtseva, A., Vorobev, G., Timofeeva, V., Ustinin, D., Zvezdin, A., and Tegeranchi, M. *Journal of Experimental and Theoretical Physics* **87**, 146–151 (1998). 10.1134/1.558635.

[9] Buksphan, S., Fischer, E., and Hornreich, R. M. *Solid State Communications* **10**(8), 657 – 662 (1972).

[10] Al'shin, B. I. and Astrov, D. *Sov. Phys. JETP* **17**, 809 (1963).

[11] Dzyaloshinskii, I. E. *JETP* **10**, 628 (1959).

[12] Rado, G. T. *Phys. Rev.* **128**(6), 2546–2556 Dec (1962).

[13] Hornreich, R. and Shtrikman, S. *Phys. Rev.* **161**(2), 506–512 Sep (1967).

[14] Yatom, H. and Englman, R. *Phys. Rev.* **188**(2), 793–802 Dec (1969).

[15] Íñiguez, J. *Phys. Rev. Lett.* **101**(11), 117201 Sep (2008).

[16] Mostovoy, M., Scaramucci, A., Spaldin, N. A., and Delaney, K. T. *Phys. Rev. Lett.* **105**(8), 087202 Aug (2010).

[17] Rado, G. T. and Folen, V. J. *Phys. Rev. Lett.* **7**(8), 310–311 Oct (1961).

[18] Bertaut, E. F. *Magnetism*, volume III. Academic Press, New York.

[19] Borovik-Romanov, A. S. and Grimmer, H. *International Tables for Crystallography*. Kluwer Academic, Dordrecht, (2003).

5

High-Tc magnetoelectric effect in ferromagnetic thin films

In this chapter we consider magnetoelectric phenomena occurring in the "stripe domain" phase of a thin film ferrimagnetic insulator. The Néel walls between ferromagnetic domains induce electric polarization through the same mechanism that induces ferroelectricity in cycloidal spiral states. Using Monte Carlo simulations we study patterns of electric polarization induced by these magnetic domain walls. We show that neighboring walls carry opposite electric polarizations. We show that a sufficiently strong electric field can align the electric polarization of all domain walls. At the flip transition the dielectric constant strongly increases.

5.1 Introduction

Cycloidal spirals states induce an electric polarization, which can be controlled by applied magnetic fields. However, in insulators these states originate from competing interactions between spins, which frustrate collinear spin orders; therefore, they usually occur far below room temperature [1]. Low transition temperatures together with the small magnitudes of the induced electric polarization [see sec.1.4.2] constitute the major obstacles on the way to technological applications of these materials [4]. In this chapter we suggest a route to magnetically-induced ferroelectricity at high temperatures. We propose to use the electric polarization of ferromagnetic domain

[1] Remarkable exceptions are hexaferrite $Ba_{0.5}Sr_{1.5}Zn_2Fe_{12}O_{22}$ ($T_S = 326$ K) [1; 2] and CuO ($T_S = 230$ K)[3].

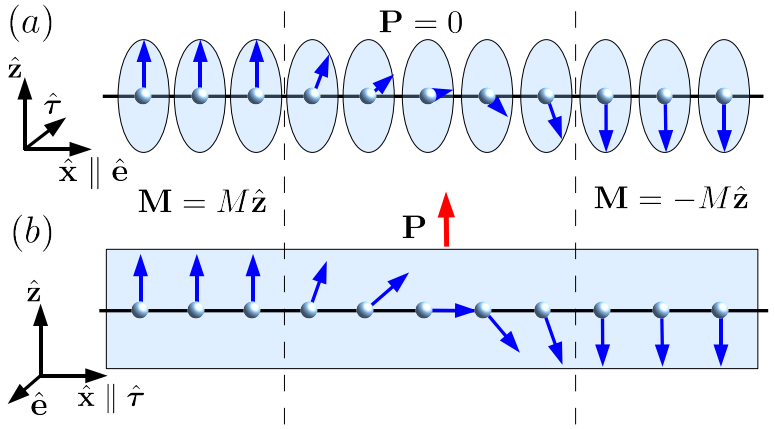

Figure 5.1: Sketches of magnetic domain walls (between the dashed lines) separating two domains with opposite magnetizations. A Bloch wall (a) does not carry electric polarization, while a Néel wall induces an electric polarization in the direction perpendicular to the axis around which spins rotate ($\hat{\mathbf{e}}$) and the normal to the wall ($\hat{\mathbf{x}}$).

walls, which has the same origin as the ferroelectricity of spin spiral states [5]. Ferromagnetic domain walls smoothly connect domains with different magnetization directions. In the so-called 180° ferromagnetic domain wall, which links two domains with opposite magnetization $\pm M\hat{\mathbf{z}}$ [see Fig. 5.1 (a) and (b)], the space dependence of magnetization is

$$\mathbf{M}(x) = M(\sin(\phi(x))\,\hat{\boldsymbol{\tau}} + \cos(\phi(x))\,\hat{\mathbf{z}}), \tag{5.1}$$

where x is the coordinate normal to the domain wall, $\hat{\boldsymbol{\tau}} \perp \hat{\mathbf{z}}$ and the angle ϕ monotonously varies between 0 and π. In analogy with magnetic spirals, domain walls can be classified according to the relative orientation of the axis around which $\mathbf{M}$ rotates, $\mathbf{e} = \hat{\boldsymbol{\tau}} \times \hat{\mathbf{z}}$, and $\hat{\mathbf{x}}$. In the so-called Bloch walls $\mathbf{e} \parallel \hat{\mathbf{x}}$ [see Fig.5.1 (a)], while in Néel walls $\mathbf{e}$ is orthogonal to $\hat{\mathbf{x}}$ [see Fig.5.1 (b)]. The difference between the Bloch and Néel walls is similar to the difference between the helical and cycloidal spirals. This analogy arises from the fact that one can picture a domain wall as a stretched half period of a spiral. Thus, it is natural to expect that the Lifshitz invariant coupling Eq.(1.7) can lead to a spontaneous polarization at the domain wall. Substituting Eq.(5.1) in Eq.(1.8), one finds that a Néel domain wall carries an electric dipole moment per unit area of the wall, while a Bloch wall has no polarization. Furthermore, considering a periodic pattern of Néel domain walls, one gets

$$P_z \equiv \gamma\chi_e \int_{-\infty}^{\infty} (M^z \partial_x M^x - M^x \partial_x M^z)\, dx = \gamma\chi_e\,(\phi(\infty) - \phi(-\infty))\,, \tag{5.2}$$

which means that the total induced electric polarization is proportional to the number of times that the magnetization rotates around the $\hat{\mathbf{e}}$ axis in the sample.

Periodic arrays of domain walls are spontaneously induced in the so-called stripe domain phase of ferromagnetic thin films [6; 7]. In this magnetic state, as we shall see below, stripes with opposite magnetization are stabilized by the long range magnetostatic interactions. The stripe domain patterns can appear well above room temperature. Indeed, for the most studied "magnetic striped" materials, which are are doped versions of the ferrimagnetic yttrium iron garnet (YIG), $Y_3Fe_5O_{12}$, Curie temperatures range from 540 K to 570 K [6]. The stability of the stripe domain pattern and the high transition temperatures make thin films of these materials good candidates for the observation of magnetoelectric effects induced by domain walls. In the first section of this chapter we review the mechanisms that stabilize the stripe domain phase in thin films and discuss the pattern of electric polarization induced by Néel walls separating the ferromagnetic domains. Then we introduce our spin model of a thin ferromagnetic film and present the Monte Carlo results for the transition to the striped phase. Finally, we discuss the effect of an applied electric field on the polarization pattern at nonzero temperature showing the existence of a flip transition where the dielectric constant increases dramatically.

5.2 Striped phase of ferromagnetic thin films

In this section we discuss the Landau theory describing the formation of the stripe domain phase in ferromagnetic thin films. We first note that an important role in the phenomenological theory of thin film is played by the dipole-dipole interaction:

$$\Phi_{DD} = \frac{(g\mu_B)^2}{2} \int d\mathbf{r} \int d\mathbf{r}' \left[\frac{\mathbf{M}(\mathbf{r}) \cdot \mathbf{M}(\mathbf{r}')}{|\mathbf{r}-\mathbf{r}'|^3} - 3\frac{(\mathbf{M}(\mathbf{r}) \cdot (\mathbf{r}-\mathbf{r}'))\,(\mathbf{M}(\mathbf{r}') \cdot (\mathbf{r}-\mathbf{r}'))}{|\mathbf{r}-\mathbf{r}'|^5} \right], \tag{5.3}$$

where g is the gyromagnetic factor, μ_B is the Bohr magneton, $\mathbf{M}(\mathbf{r})$ is the local magnetization at the point $\mathbf{r}$ divided by $g\mu_B$ and Gaussian units are used. After a double integration by parts, the right-hand-side of Eq.(5.3) can be conveniently rewritten as

$$\Phi_{DD} = \frac{(g\mu_B)^2}{2} \int d\mathbf{r} \int d\mathbf{r}' \frac{(\nabla_{\mathbf{r}} \cdot \mathbf{M}(\mathbf{r}))\,(\nabla_{\mathbf{r}'} \cdot \mathbf{M}(\mathbf{r}'))}{|\mathbf{r}-\mathbf{r}'|}, \tag{5.4}$$

which can be pictured as the Coulomb energy associated with a density of magnetic charges $Q(\mathbf{r}) = -\nabla \cdot \mathbf{M}$. In the case of uniform magnetization these charges are present only at the boundaries of the sample where the magnetization abruptly changes from $\mathbf{M}$ to 0. For the thin film samples with weak anisotropies the system avoids formation of those charges by forming a state with an in-plane magnetization. In other words, the dipole-dipole interactions in thin films effectively result in the easy-plane magnetic anisotropy: a state with uniform $\mathbf{M}$ oriented perpendicular to the film creates two opposite magnetic charges separated by the film thickness h, whereas, for $\mathbf{M}$ lying in the film plane, these charges are separated by the film width L. Since the latter configuration is energetically less expensive, the magnetization lies in the film plane.

We consider now the free energy expansion when the dipole-dipole term competes with a magnetocrystalline anisotropy that favors **M** normal to the film plane. The case of large magnetocrystalline uniaxial anisotropy was first studied by Garel and Doniach [8], who considered a system of Ising spins. However, since the rotation of **M** through the domain wall is crucial for our discussion, we will consider the more general case of non-collinear magnetic moments. The Landau expansion of the free energy of a ferromagnetic thin film is $\Phi = \Phi_0 + \Phi_A + \Phi_{DD}$, where Φ_0 contains all the rotational invariant terms and Φ_A is the magnetic anisotropy term coming from the magnetocrystalline interaction, i.e. spin orbit coupling. Consider a film of thickness h and assume that the z axis is perpendicular to the film plane. In addition, we assume that the magnetization **M** does not depend on z. It is convenient to perform the Fourier transform of the magnetization:

$$\tilde{\mathbf{M}}(\mathbf{q}) = \int d\mathbf{r}_\perp \mathbf{M}(\mathbf{r}_\perp) e^{-i\mathbf{q}\cdot\mathbf{r}_\perp}, \tag{5.5}$$

where $\mathbf{r}_\perp$ is the position vector in the the plane and $\mathbf{q} = q_x\hat{\mathbf{x}} + q_y\hat{\mathbf{y}}$ is the wave vector lying in the plane. Then the rotational invariant part of the free energy is

$$\begin{aligned}\Phi_0 &= h\left[\int \frac{d\mathbf{q}}{(2\pi)^2}\frac{1}{2}\left[a(T) + c_x q_x^2 + c_y q_y^2\right]\tilde{M}^2 + \right. \\ &\left. + \frac{b}{4}\int\frac{d\mathbf{q}}{(2\pi)^2}\int\frac{d\mathbf{q}_1}{(2\pi)^2}\int\frac{d\mathbf{q}_2}{(2\pi)^2}\tilde{M}^\alpha(\mathbf{q})\tilde{M}^\alpha(\mathbf{q}_1)\tilde{M}^\beta(\mathbf{q}_2)\tilde{M}^\beta(-\mathbf{q}-\mathbf{q}_1-\mathbf{q}_2) + \dots\right],\end{aligned} \tag{5.6}$$

where c_x and c_y are the exchange stiffness constants, respectively, along the x and y directions, the sum over the repeated indexes $\alpha, \beta = x, y, z$ is implied and we neglect the higher powers of $\tilde{\mathbf{M}}$. The term Φ_A is the second-order anisotropy favoring the magnetization perpendicular to the film plane:

$$\Phi_A = -\frac{h\Delta}{2}\int\frac{d\mathbf{q}}{(2\pi)^2}(\tilde{M}^z)^2, \tag{5.7}$$

where $\Delta > 0$. The term Φ_{DD} is given by Eq.(5.4). As discussed in Appendix 5.A, for $\mathbf{M} = \mathbf{M}(x, y)$, this term can be rewritten as follows:

$$\Phi_{DD} = \frac{\gamma h}{2\pi}\int d\mathbf{q}\left[\frac{1-e^{-qh}}{qh}\left|\tilde{M}^z\right|^2 + \left(1 - \frac{1-e^{-qh}}{qh}\right)\frac{|\mathbf{q}\cdot\tilde{\mathbf{M}}|^2}{q^2}\right], \tag{5.8}$$

where $\gamma = \frac{(g\mu_B)^2}{2}$.
Next we show that, depending on the relative size of Δ and γ, the minimization of Φ at the ferromagnetic transition can give two different magnetic structures: the uniformly magnetized state with $\mathbf{M} \perp \mathbf{z}$ or the stripe domain state where $\mathbf{M} \parallel \mathbf{z}$. Just below T_C, $\mathbf{M}(\mathbf{r})$ is arbitrarily small and the fourth-order terms in Eq.(5.7) are

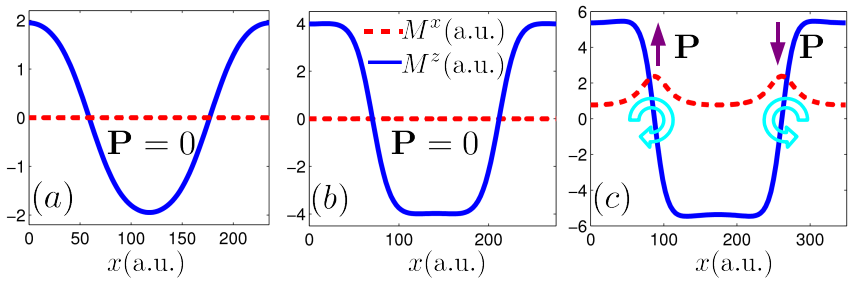

Figure 5.2: Evolution of the magnetic domain profiles increasing the value of $\tau = \frac{T-T_N}{T_N}\ T_1$. obtained by numerical minimization of Φ for $Q = 1.01$. At $\tau = 0.0001$ (a) a sinusoidal spin-density-wave sets in. At $\tau = 0.0005$ (b) the spin-density-wave has the domain profile. At $\tau = 0.001$ (c) Néel walls between the domains appear. The magnetostatic interaction favors the in-plane magnetization of the walls to point in the same direction, forcing neighboring walls to induce opposite electric polarizations. The profiles are obtained by numerical minimization of Φ for $Q = 1.01$.

negligible. In these regime the free energy is

$$\Phi \approx \frac{h}{2}\int \frac{d\mathbf{q}}{(2\pi)^2}\left[f(T,\mathbf{q})|\tilde{M}^z(\mathbf{q})|^2 + g(T,\mathbf{q})|\mathbf{q}\cdot\tilde{\mathbf{M}}_\perp(\mathbf{q})|^2\right], \tag{5.9}$$

where $\tilde{\mathbf{M}}_\perp$ lies in the film plane,

$$f(T,q) = a(T) + c_x q_x^2 + c_y q_y^2 + 4\pi\gamma\left(\frac{1-e^{-qh}}{qh}\right) - \Delta, \tag{5.10}$$

and

$$g(T,q) = a(T) + c_x q_x^2 + c_y q_y^2 + 4\pi\gamma\left(1 - \frac{1-e^{-qh}}{qh}\right). \tag{5.11}$$

We note that the minimum of $g(T,\mathbf{q})$ and of $f(T,\mathbf{q})$ with respect to $\mathbf{q}$ occur, respectively, at $\mathbf{q} = 0$ and $\mathbf{q} = \mathbf{q}_{min} \neq 0$. Moreover, it is convenient to notice that $f(T,\mathbf{q}_{min}) - g(T,0) \approx 4\pi\gamma - \Delta$ is temperature independent. The state that sets in at the transition depends on which of the two minima becomes zero at $T = T_C$ or, in other words, on the value of the so-called quality factor:

$$Q = \frac{\Delta}{4\pi\gamma}. \tag{5.12}$$

For $Q < 1$, $g(T_C,0) = 0$ and the instability occurs towards a state with Fourier component $\tilde{M}_\perp(0) \neq 0$, i.e. the state uniformly magnetized in the film plane. For $Q \gtrsim 1$, $f(T_C,\mathbf{q}_{min}) = 0$ and a state with $\tilde{M}^z(\mathbf{q}_{min}) \neq 0$ sets in. This state correspond

to the sinusoidal spin-density-wave [see Fig. 5.2(a)] with $\tilde{\mathbf{M}}$ oriented along $\mathbf{z}$ and the wave vector $\mathbf{q}_{min}$ oriented along the direction with the lowest exchange stiffness constant.
As the temperature is decreased below T_C, the fourth-order terms in M contribute to the free energy. These terms couple Fourier components with different wave vectors [see Eq.(5.7)]. For $Q \gtrsim 1$, the effect of this coupling on the minimal Φ state is to admix $\tilde{M}^z_S(\mathbf{q}_{\min})$ with the higher harmonics $(\tilde{M}^\alpha_S(3\mathbf{q}_{\min}), \tilde{M}^\alpha_S(5\mathbf{q}_{\min}), \dots)$. As shown in Fig. 5.2 (b), in the coordinate representation this corresponds to the cross-over from the sinusoidal modulation of magnetization to the periodic array of domain walls [see Fig. 5.2(c)]. Since the largest contribution to the magnetization profile comes from the Fourier component of $\mathbf{M}^z(\mathbf{q}_{min})$, half of the spin-density-wave period at T close to T_c gives approximately the width d of a magnetic domain. This width is much larger than the lattice constant a, due to the weakness of magnetostatic coupling compared to the exchange stiffness, and it depends on the film thickness. For small values of the film's thickness compared to the domain width, $q_{\min} h \ll 1$, one can expand the exponential e^{-qh} in the right-hand side of Eq.(5.10). With this approximation one obtains the value

$$q_{min} \approx \frac{\pi\gamma h}{\min(c_x, c_y)}. \tag{5.13}$$

In what follows we will consider the case, $c_x < c_y$ and, therefore, $\mathbf{q}_{min}$ will be oriented along $\mathbf{x}$.
Next we discuss two other effects of the dipole-dipole interaction. First, the magnetostatic energy Eq.(5.4) always favors Bloch walls in which magnetization rotates in the yz plane. Indeed, in this type of walls $\nabla \cdot \mathbf{M}$ in Eq.(5.4) vanishes. From our perspective this is undesirable since, according to Eq.(1.8), Bloch walls do not carry any electric polarization. Nonetheless, Néel walls, which have higher magnetostatic energy, can be stabilized by strong magnetocrystalline anisotropy within the film plane or by a magnetic field applied along the x direction [see Ref.[9]].
Second, the magnetostatic interaction favors a state with $\mathbf{P} = 0$. If we assume that magnetization only varies along one direction, e.g. along the x axis, the dipolar interaction Eq.(5.3) favors the in-plane magnetization of neighboring walls to point in the same direction [see Fig. 5.2 (c)]. This means that the magnetization rotates in opposite direction in neighboring domain walls and the term at the right-hand side of Eq.(5.2) vanishes. If the magnetization varies also along the other in-plane direction, i.e. along the y axis, the case is more complex. The magnetostatic interaction between the domain walls can favor a state in which the magnetization has opposite rotation directions in different regions of the same Néel wall. This gives rise to the so-called vertical Bloch lines in the domain wall, i.e. a line propagating along the z axis that separates regions of the same domain wall with opposite rotation directions of spins [7]. Since we assume $\mathbf{M}$ to be independent on z, we can only obtain straight Bloch lines, which, in our two-dimensional model corresponds to points in the xy plane.

5.3 Monte Carlo simulation

In this section we introduce an effective Hamiltonian for the microscopic model of a thin ferromagnetic film and discuss its magnetic properties obtained by Monte Carlo simulation.
The large width of the magnetic domains compared to the lattice constant, $d \gg a$, makes the simulation of microscopic models of domain wall patterns computationally demanding unless some coarse graining is introduced. Furthermore, the long range dipole-dipole interaction makes Monte Carlo simulations very time-consuming. To make numerical simulation more accessible, we consider a coarse grained model derived from the microscopic Hamiltonian. In addition we assume that all spins lie in the xz plane, which allows us to further decrease the computational time.

5.3.1 The model

We first describe the underlying microscopic model and then the coarse graining procedure. We assume that the magnetization $\mathbf{M}$ does not depend on the z-coordinate. This assumption allows us to reduce our model to a two-dimensional one described by the energy density per unit length along the z direction. Denoting by H this energy density and by $\mathbf{r}$ the position in the film plane, the part of H coming from the exchange interaction and the magnetocrystalline anisotropy is

$$H_B = \sum_{\mathbf{r}} \left[J_x \mathbf{S}_{\mathbf{r}} \cdot \mathbf{S}_{\mathbf{r}+\mathbf{x}} + J_y \mathbf{S}_{\mathbf{r}} \cdot \mathbf{S}_{\mathbf{r}+\mathbf{y}} - \Delta_z (S^z_{\mathbf{r}})^2 \right], \tag{5.14}$$

where J_x and J_y are the ferromagnetic exchange constants between nearest-neighbor spins, respectively, along the x and the y directions and Δ_z is the strength of the easy axis anisotropy. The term in H coming from dipole-dipole interaction is

$$H_D = \frac{1}{2} \sum_{\alpha,\beta} \sum_{\mathbf{r} \neq \mathbf{r}'} S^{\alpha}_{\mathbf{r}} g^{\alpha\beta}(|\mathbf{r} - \mathbf{r}'|) S^{\beta}_{\mathbf{r}'}, \tag{5.15}$$

where $\alpha, \beta = x, z$ are the spins components and the functions $g^{\alpha\beta}(r)$ are obtained dividing the dipole-dipole interaction Eq.(5.4) integrated along z by h [see Appendix 5.A].
The coarse grained Hamiltonian is obtained by partitioning the lattice into squares $\sigma_{\bar{\mathbf{r}}}$ with l sites along the edge and centered at the positions $\bar{\mathbf{r}}$ [see Fig 5.3]. Inside each square spins are assumed to rotate uniformly. Then the coarse-grained interactions for block spins at the center of each square, $\bar{\mathbf{S}}_{\bar{\mathbf{r}}}$, have the form of Eq.(5.14) and Eq.(5.15) with the rescaled couplings $\bar{J}_x$, $\bar{J}_y$, $\bar{\Delta}$ and $\bar{g}(|\bar{\mathbf{r}} - \bar{\mathbf{r}}'|)$.
The value of the rescaled coupling is fixed by requiring that the energy density of the coarse grained model is approximately the same as in the original one. Let us consider a square $\sigma_{\bar{\mathbf{r}}}$ and denote by θ_1 and θ_2 the angles between the z and the spins, respectively, at one of its border and at the border of the next square [see Fig. 5.3]. The spins inside the square rotate uniformly by the angle $\theta = (\theta_2 - \theta_2)/l$. In the

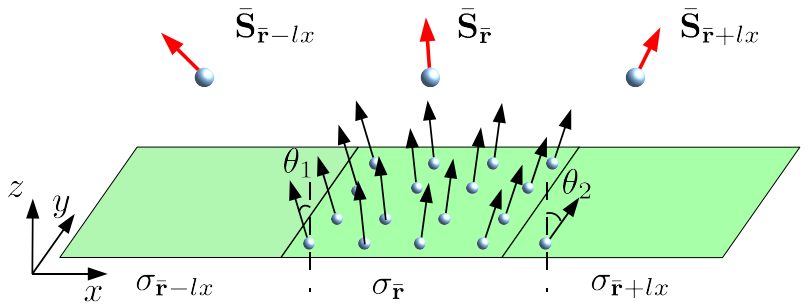

Figure 5.3: Sketch showing the coarse graining of the model. The spins (black thin arrows) are assumed to rotate uniformly inside a square $\sigma_{\bar{\mathbf{r}}}$. An approximation to the Hamiltonian Eq.(5.14) and Eq.(5.15) is obtained by considering as variables only the spins $\bar{\mathbf{S}}_{\bar{\mathbf{r}}}$ at the center of each square. The coarse grained Hamiltonian has the same form as in the microscopic model but with rescaled couplings $J_x \to \bar{J}_x$, $J_y \to \bar{J}_y$, $\Delta \to \bar{\Delta}$ and $g^{\alpha\beta}(|\mathbf{r}-\mathbf{r}'|) \to \bar{g}^{\alpha\beta}(|\bar{\mathbf{r}}-\bar{\mathbf{r}}'|)$.

microscopic model this costs energy $\epsilon \approx C_1 + \frac{J_x S^2\theta^2}{2a^3}$, where C_1 is a constant. In the coarse grained Hamiltonian the energy density is given by

$$\epsilon = \frac{\bar{J}_x \mathbf{S}_{\bar{r}} \cdot \mathbf{S}_{\bar{r}+l\mathbf{x}}}{2a^3 l^2} \approx C_2 + \frac{\bar{J}_x S^2(\theta_2-\theta_1)^2}{2a^3 l^2} = C_2 + \frac{\bar{J}_x S^2\theta^2}{2a^3}, \tag{5.16}$$

where $\bar{J}_x$ is the effective exchange constant between neighboring squares. Comparing the θ-dependent part[2] of the two energy densities one gets $\bar{J}_x \approx J_x$. The same relation holds for the rescaled exchange constant along y, while a similar analysis of the anisotropy energy gives $\bar{\Delta} \approx l^2\Delta$. It is easy to see that the scaling preserves the width of the domain wall: $\omega \approx \pi\sqrt{J_x/\Delta} = \pi l\sqrt{\bar{J}_x/\bar{\Delta}}$. The dipolar interaction between two squares, $\sigma_{\bar{\mathbf{r}}}$ and $\sigma_{\bar{\mathbf{r}}'}$, is obtained by summing up the interaction Eq.(5.15) between all spins in $\sigma_{\bar{\mathbf{r}}}$ and all spins in $\sigma_{\bar{\mathbf{r}}'}$:

$$\bar{g}^{\alpha\beta}(|\bar{\mathbf{r}}-\bar{\mathbf{r}}'|) = \sum_{r\in\sigma_{\bar{\mathbf{r}}}} \sum_{r'\in\sigma_{\mathbf{r}'}} g^{\alpha\beta}(|\mathbf{r}-\mathbf{r}'|), \tag{5.17}$$

where the latter summation is done numerically at the beginning of the Monte Carlo algorithm. By simulating the coarse grained model we neglect the collective spin fluctuations occurring on length scales smaller than l. However, these short wave length fluctuations do contribute to free energy. A more accurate coarse graining, can be done by using renormalization analysis, but, as we shall see below, the coarse graining procedure is sufficient to describe the physics of the striped phase.
The Monte Carlo calculations have been performed with local updates according to the Metropolis algorithm. Since the most time-consuming operation is the calculation of the dipolar energy, instead of performing its calculation at every update trial, we store and update the potential $V(\bar{\mathbf{r}}) = \frac{1}{2}\sum_{\bar{\mathbf{r}}'\neq\bar{\mathbf{r}}} \bar{g}^{\alpha,\beta}(|\bar{\mathbf{r}}-\bar{\mathbf{r}}'|)\bar{\mathbf{S}}_{\bar{\mathbf{r}}'}$. This has the advantage

[2]The two constant C_1 and C_2 are irrelevant to the purpose of calculating thermal averages.

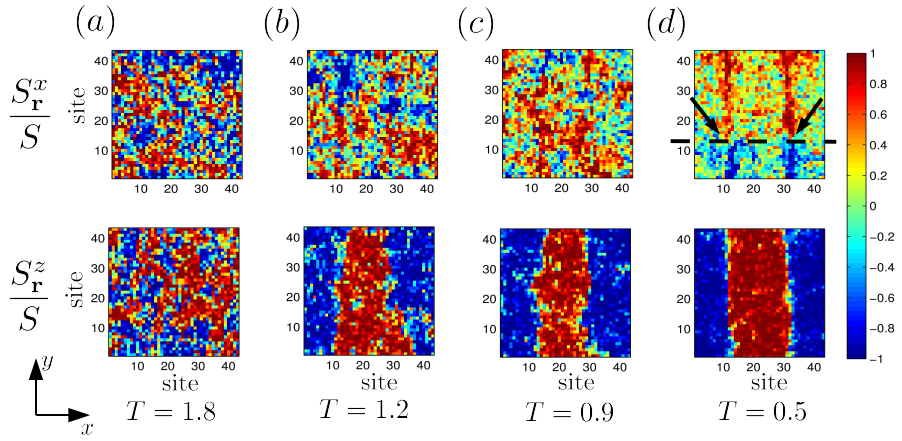

Figure 5.4: Snapshot of $S^x_{\mathbf{r}_\perp}$ (upper panels) and $S^z_{\mathbf{r}_\perp}$ (bottom panels) from the Monte Carlo simulation performed at various temperatures. At $T = 1.8S^2J_x$ (a) the film is in the paramagnetic state, while at T below $1.5S^2J_x$ (b) the striped phase, with magnetization out of planes, sets in. In the picture the domain walls between the stripes become visible in the $S^x_{\mathbf{r}}$ pattern below $T = 0.9S^2J_x$ (c and d) . The parameters used in the simulation are $J_y = 2J_x$, $\Delta = 2 \cdot 10^{-3}J_x$, $\gamma = 1.2 \cdot 10^{-4}J_x$, $h = 400$ and $l = 20$, corresponding to the width of the domain and of the domain wall, respectively, of 26 spins and 3 or 4 spins in the units of the coarse grained lattice constant (520 and 70 microscopic lattice constants). The arrows indicate the appearance of two Bloch lines.

that the update of the potential, which involves a sum all over the lattice, has to be done only for successful Monte Carlo updates.
Simulations of the coarse-grained Hamiltonian have been done for square lattices of spins with open boundary conditions. The number of spins, $L \times L$, in a lattice is drastically limited due to the long range nature of the dipolar interactions, which makes the simulation times already large for $L \approx 50$ sites. The choice of l is dictated by the following requirements. Since we want to take into account interactions between domain walls, the lattice has to contain at least a few of them; therefore, L should be larger than d/l. On the other hand, in order to observe the dielectric properties induced by Néel domain walls, the coarse graining scale l has to be smaller than the width ω of the domain wall: $l < \omega$.
The last remark about the model we used concerns its dimensionality. According to the Mermin-Wagner theorem, a long range order in two-dimensional systems with continuous symmetry is destroyed at any temperature by long wave length fluctuations [10]. However, in the model that we simulate, the strength of the easy axis anisotropy, $\bar{\Delta} = l^2\Delta$, is large. Therefore, the magnon dispersion of the coarse grained Hamiltonian has a gap of the size $\sqrt{\bar{J}_x\bar{\Delta}}$, which makes the spins, at temperatures smaller than the gap, effectively Ising-like.

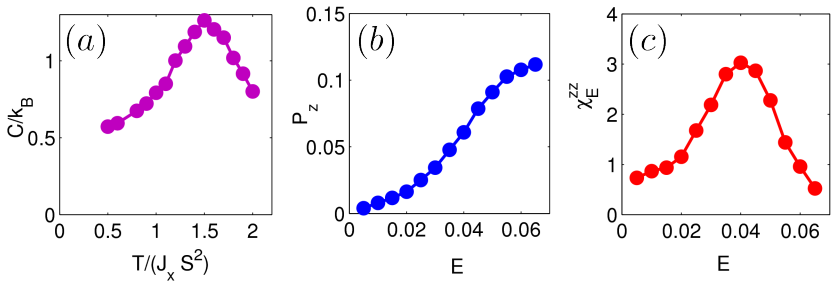

Figure 5.5: Monte Carlo results for the temperature dependence of the magnetic specific heat per spin (a) of the coarse grained Hamiltonian at $E = 0$. The transition to the stripe phase occurs at $T = 1.5S^2J_x$. Panel (b) shows the electric field dependence of the total polarization per spin, while panel (c) shows the electric field dependence of the dielectric susceptibility. The flip transition to the state where the electric polarizations all Néel domain walls are aligned, gives rise to a 300% increase in the dielectric susceptibility χ_E^{zz}.

5.3.2 Stripe domain phase in absence of electric field

To obtain transition temperatures similar to the one of ferrimagnetic iron garnets, we consider effective ferromagnetic exchange couplings of the order $J/k_B \sim 50$ K. For the lattice constant[3] $a \approx 5$ Å the strength of the dipolar interactions, $\gamma/k_B = \frac{(g\mu_B)^2}{k_B a^3}$, is of the order 10^{-2} K. For the film thickness $h = 400$ lattice constants and for $\gamma/J_x = 1.2 \cdot 10^{-4}$ one obtains the value $d \approx 520$ unit cells[4]. The minimal value of the strength of uniaxial anisotropy is given by the requirement $Q > 1$. Choosing $\Delta/J_x = 2 \cdot 10^{-3}$, one gets $Q = 1.33$ and $\omega \approx 70$ unit cells. Therefore, simulation of rather small lattices ($L \approx 50$ unit cells) can be achieved considering a coarse graining with $l = 20$.
Figure 5.4 shows snapshots from the Monte Carlo simulation at different temperatures for these parameters and for $L = 43$. The transition temperature can be estimated from the temperature dependence of the magnetic specific heat per particle, C, shown in Fig.5.5 (a). Considering the magnetic lattice formed by Fe^{3+} ions ($S = 5/2$) and $J_x/k_B = 50$ K, the transition temperature, $T_c = 1.5S^2J_x$, is 469 K. At temperatures above T_c the system is in a paramagnetic state [see Fig.5.4 (a)], while at temperatures slightly below T_c the stripe pattern is formed but the domain walls are not clearly distinguishable [see Fig.5.4 (b)]. As the temperature is further decreased, the domain walls become visible and the stripes become more straight [see Fig.5.4 (c) and (d)]. Moreover, in Fig. 5.4 (d) one can see two Bloch lines occurring in both domain walls.

[3]This lattice constant is smaller than the linear size of the cubic unit cell of garnets, ~ 12Å, which contains 16 iron ions but gives a reasonable estimate of the distance between neighboring Fe ions

[4]Note that in this regime the approximation $q_{min} \approx \frac{\pi\gamma h}{J_x}$ does not hold.

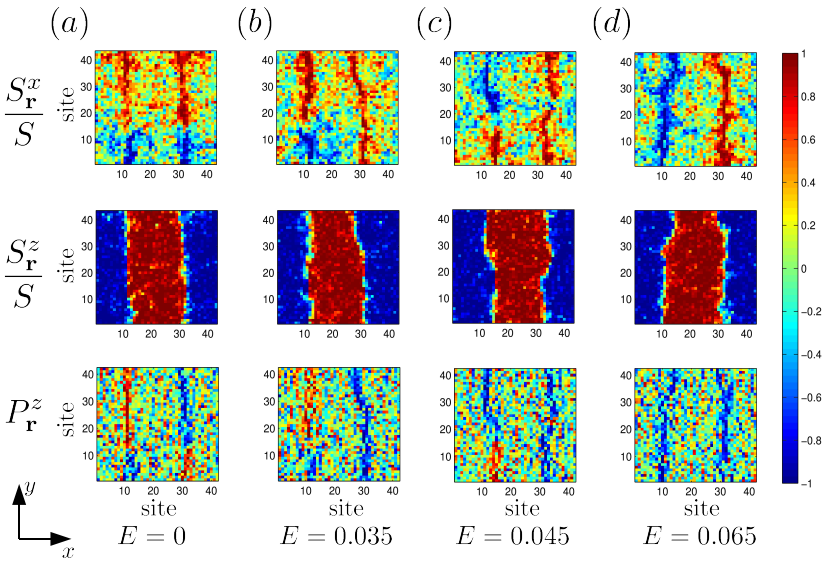

Figure 5.6: The top panels show the snapshot of spin configurations during the Monte Carlo evolution at $T = 0.5S^2J_x$ for different values of the applied electric field E. The bottom panels show the electric polarization, $P^z_{\mathbf{r}+x/2} = \varrho\,[\mathbf{S}_{\mathbf{r}} \times \mathbf{S}_{\mathbf{r}+\mathbf{x}}]_y$, induced by the magnetic configurations. At $E = 0$ the magnetostatic interaction favors the alignment of the in-plane magnetization of neighboring Néel domain walls. This gives rise to the alternation of the direction of the induced electric polarization. As the electric field is increased, the electric polarization flips together with the relative orientation of neighboring domain walls. The values of spins and electric polarization are normalized to unity.

5.4 Polarization flip

We now switch to the discussion of the electric properties of the magnetic stripe domain phase. The electric polarization induced by neighboring spins in the lattice is given by $P^z_{\mathbf{r}+x/2} = \varrho\,[\mathbf{S}_{\mathbf{r}} \times \mathbf{S}_{\mathbf{r}+\mathbf{x}}]_y$, where ϱ is a constant. The polarization pattern induced by the spins at, $T = 0.5S^2J_x$, is shown in Fig. 5.6 (a). Since the in-plane magnetizations of neighboring Néel domain walls are alligned in the lowest energy state and since Bloch lines in neighboring walls have approximately the same y coordinates, the total electric polarization in the film, $P^z = \sum_{\mathbf{r}} P^z_{\mathbf{r}+x/2}$, vanishes.
To consider the effect of an applied electric field we add to the microscopic Hamiltonian Eq.(5.14) and Eq.(5.15) the coupling between the field and the magnetically induced electric polarization,

$$H_E = -\varrho E \sum_{\mathbf{r}} [\mathbf{S}_{\mathbf{r}} \times \mathbf{S}_{\mathbf{r}+\mathbf{x}}]_y\,, \tag{5.18}$$

where, again, H_E is the Hamiltonian divided by h.

According to the procedure described in the previous section, in the coarse grained Hamiltonian this term has the same form but with E replaced by $\bar{E} = lE$[5].
Monte Carlo simulations of the coarse grained lattice have been performed for various values of the applied electric field. The competition between the dipolar interaction Eq.(5.15) of the in-plane magnetization of the Néel walls and the coupling Eq.(5.18) defines a critical value E_c for the electric field to flip the antialigned polarization pattern. As shown in Fig. 5.6 (a), at $E = 0$, $\bar{S}^x_{\mathbf{r}}$ and $P^z_{\mathbf{r}}$ are, respectively, aligned and antialigned in neighboring walls. At $E = 0.065 J_x/\varrho$ [see Fig. 5.6 (d)], the relative orientation of the magnetizations of neighboring walls is reversed and the film acquires a macroscopic electric polarization. Moreover, the Bloch lines disappear. Figures 5.5 (b) and (c) show, respectively, the dependence of the electric polarization per spin, P^z/L^2, and the electric susceptibility, χ^{zz}_E, on the electric field. At $E_c \approx 0.04 J_x S^2/\varrho$, the electric polarization jumps and χ^{zz}_E shows a relatively sharp peak at which it is enhanced by $\sim 300\%$ compared to the zero-field value.
A rough estimate for the size of E_c can be given considering the value of ϱ for some known multiferroic with spiral magnetic ordering. Considering the electric polarization of $TbMnO_3$ ($P \sim 600 \mu C/m^2$) [11], its unit cell volume similar to that of $EuMnO_3$ [12], $v \approx 225 Å^3$, and the wave vector of its spiral state $\frac{2\pi q}{b} = 0.29$, one gets $\frac{\varrho}{a^3} = 97 \mu C/m^2$. Using this value and considering microscopic cells with $a = 5$ Å, we estimate E_c to be $6 \cdot 10^5$ V/cm.

5.5 Conclusions

In conclusion, we studied ferroelectric properties of Néel domain walls separating stripe domains in a ferromagnetic thin film. By performing Monte Carlo calculations for an effective spin model, we obtain the striped phase and show that the polarizations induced by neighboring walls are antialigned. Although the film does not posses a spontaneous ferroelectric moment, an applied electric field can flip the electric polarization pattern in the film. We found a dramatic enhancement of the dielectric susceptibility at this transition.
The strength of the electric field necessary to flip the magnetic domain walls is rather high but still realistic. Recently Pyatakov *et al.* [9] confirmed experimentally the ferroelectricity of Néel domain walls. By applying a strong local electric field close to the walls, they observed a displacement of the micromagnetic structure for a thin film of iron garnet $(BiLu)_3(FeGa)_5O_{12}$. They showed that two neighboring walls are, respectively, attracted and repelled by the local electric field and when the electric field is inverted their displacements change sign.
These results underline the importance of the physics of domain walls for the analysis and design of materials displaying magnetoelectric effects. In particular, magnetic domain walls not only provide a coupling between magnetization and induced electric polarization [see Chapter 2], but they can also carry electric polarization themselves.

[5] Following the notation of sec. 5.3.1 the energy density associate with the term Eq.(5.18) in the microscopic model is: $\epsilon \approx \frac{\varrho E \theta}{a^3}$. In the coarse grained Hamiltonian the same therm gives: $\epsilon \approx \frac{\varrho \bar{E}(\theta_2 - \theta_1)}{a^3 l^2} = \frac{\varrho \bar{E} \theta}{a^3 l}$. The comparison between the two expressions gives $\bar{E} = lE$

5.A Appendix A: Magnetostatic interaction in ferromagnetic thin-films

In this appendix we obtain the expression of the magnetostatic energy Eq.(5.8) and Eq.(5.15) for a thin film with thickness h [8]. We assume that the magnetization,

$$\mathbf{M}(\mathbf{r}) = \theta(\frac{h}{2} - |z|)\mathbf{M}(\mathbf{r}_\perp), \tag{5.19}$$

is independent on the coordinate $\mathbf{z}$ inside the film but is allowed to vary in the coordinates $\mathbf{r}_\perp$ of the film plane.
Considering the Fourier transform of $\mathbf{M}(\mathbf{r})$, $\tilde{\mathbf{M}}(\mathbf{Q}) = \int d\mathbf{r} M(\mathbf{r}) \exp(i\mathbf{Q}\cdot\mathbf{r})$, and replacing it in Eq.(5.4), one gets

$$\Phi_{MS} = 4\pi\gamma \int \frac{d\mathbf{q}}{(2\pi)^3} \frac{\left(\mathbf{q}\cdot\tilde{\mathbf{M}}(\mathbf{q})\right)^2}{q^2}. \tag{5.20}$$

In the Fourier space Eq.(5.19) reads $\mathbf{M}(\mathbf{Q}) = 2\tilde{\mathbf{M}}(\mathbf{q}_\perp)\sin(q_z h/2)/q_z$, where q_z and $\mathbf{q}_\perp$ are, respectively, the out-of-plane and in-plane components of the wave vector. By replacing this expression in Eq.(5.20) and noticing that the terms odd in q_z vanish in the integration, the magnetostatic energy reads

$$\begin{aligned}
\Phi_{MS} &= 4\pi\gamma \int \frac{d\mathbf{q}}{(2\pi)^3} \frac{1}{q^2} \left[\frac{(\mathbf{q}_\perp\cdot\tilde{\mathbf{M}}_\perp)^2}{q_z^2} + (\tilde{M}^z)^2\right] \sin^2\left(\frac{q_z h}{2}\right) \\
&= 2\pi\gamma \int \frac{d\mathbf{q}}{(2\pi)^3} \left[\frac{(\mathbf{q}_\perp\cdot\tilde{\mathbf{M}}_\perp)}{q_z^2} + \tilde{M}_z^2\right] \frac{(1-e^{-iq_z h})}{q_\perp^2 + q_z^2},
\end{aligned} \tag{5.21}$$

where in the last step we performed the change of variable $q_z \to -q_z$ for the term related to e^{ihq_z} coming from $\sin^2(iq_z h)$.
Replacing Eq.(5.19) in Eq.(5.3) and considering $\mathbf{M}$ oriented in the xz plane, one gets

$$\Phi_{MS} = \frac{1}{2}\int d\mathbf{r}_\perp \int d\mathbf{r}'_\perp \sum_{\alpha,\beta} \left[M^\alpha(\mathbf{r}) g^{\alpha\beta}(|\mathbf{r}-\mathbf{r}'|) M^\beta(\mathbf{r}')\right], \tag{5.22}$$

where

$$\begin{aligned}
g^{xx}(|\mathbf{r}_\perp|) &= \gamma \int_{-\frac{h}{2}}^{\frac{h}{2}} dz \int_{-\frac{h}{2}}^{\frac{h}{2}} dz' \left[\frac{1}{(r_\perp^2 + (z-z'))^{\frac{3}{2}}} - 3\frac{(x)^2}{(r_\perp^2 + (z-z'))^{\frac{5}{2}}}\right] \\
&= \gamma \left[\frac{\sqrt{r_\perp^2 + h^2} - r_\perp}{r_\perp^2} - \frac{x^2\left(2h^2 + r_\perp^2 - \sqrt{r_\perp^2 + h^2}\right)}{r_\perp^4\sqrt{r_\perp^2 + h^2}}\right],
\end{aligned} \tag{5.23}$$

$$
\begin{aligned}
g^{zz}(|\mathbf{r}_\perp|) &= \gamma \int_{-\frac{h}{2}}^{\frac{h}{2}} dz \int_{-\frac{h}{2}}^{\frac{h}{2}} dz' \left[\frac{1}{(r_\perp^2 + (z-z'))^{\frac{3}{2}}} - 3\frac{(z-z')^2}{(r_\perp^2 + (z-z'))^{\frac{5}{2}}} \right] \\
&= \gamma \left[\frac{1}{r_\perp} - \frac{1}{\sqrt{r_\perp^2 + h^2}} \right] \qquad (5.24)
\end{aligned}
$$

and $g^{zx}(|\mathbf{r}_\perp|) = g^{xz}(|\mathbf{r}_\perp|) = 0$.

Bibliography

[1] Kimura, T., Lawes, G., and Ramirez, A. P. *Phys. Rev. Lett.* **94**(13), 137201 Apr (2005).

[2] Ishiwata, S., Taguchi, Y., Murakawa, H., Onose, Y., and Tokura, Y. *Science* **319**(5870), 1643–1646 (2008).

[3] Kimura, T., Sekio, Y., Nakamura, H., Siegrist, T., and Ramirez, A. P. *Nat Mater* **7**(4), 291–294 Apr (2008). 10.1038/nmat2125.

[4] Cheong, S.-W. and Mostovoy, M. *Nat Mater* **6**(1), 13–20 Jan (2007). 10.1038/nmat1804.

[5] Mostovoy, M. *Phys. Rev. Lett.* **96**(6), 067601 Feb (2006).

[6] Bobeck, A. and Della Torre, E. *Magnetic Bubbles*. North-Holland — American Elsevier, (1975).

[7] Malozemoff, A. and Slonczwski, J. *Magnetic Domain Walls in Bubble Materials*. Academic Press, (1979).

[8] Garel, T. and Doniach, S. *Phys. Rev. B* **26**(1), 325–329 Jul (1982).

[9] Pyatakov, A., Sechin, D., Nikolaev, A., Nikolaeva, E., and Logginov, A. arXiv:1001.0672, (2010).

[10] Mermin, N. D. and Wagner, H. *Phys. Rev. Lett.* **17**(22), 1133–1136 Nov (1966).

[11] Kimura, T., Lawes, G., Goto, T., Tokura, Y., and Ramirez, A. P. *Phys. Rev. B* **71**(22), 224425 Jun (2005).

[12] Mochizuki, M. and Furukawa, N. *Phys. Rev. B* **80**(13), 134416 Oct (2009).

6

Magnetic Polarons

The solid solution series of ilmenite and hematite, $(1-x)FeTiO_3$-xFe_2O_3, exhibit an unusual insulating ferromagnetic state appearing around room temperature. We show that Fe^{3+} dopants in the non magnetic Ti^{4+} layers induce large non-collinear modulations of spins in neighboring magnetic layers to which we refer as magnetic polarons[1]. We study the features of these polarons and their effect on magnetic properties. Polarons carry a large magnetic moment which leads to superparamagnetic response at low x. Furthermore, the long-range interactions between spin polarons suppress antiferromagnetic order of ilmenite and lead to a ferromagnetic state at relatively low x.

6.1 Introduction

Solid solutions of $FeTiO_3$ and Fe_2O_3 exhibit a rich magnetic phase diagram as the concentration of Fe ions and temperature are varied. Interestingly, although both the end members of the solid solution series are antiferromagnetic, a transition to a ferrimagnetic state occurs at a small but non-zero value of the concentration of α-hematite [1]. The sudden appearance of such a ferrimagnetic state cannot be explained by an imbalance of opposite magnetizations of different sublattices. In this chapter we propose a mechanism that gives rise to the ferrimagnetic state and explains the experimentally observed phase diagram.

[1]Throughout this chapter we refer, with a little abuse of terminology, to magnetic polarons as static deformations of the spin ordering from the antiferromagnetic state induced by the presence of a magnetic impurity. Therefore, the magnetic polarons described in the text should not be confused with the magnetic polarons induced by charge carriers, for instance, in magnetic semiconductors. Moreover, they should not be confused with usual polarons caused by the interaction of charge carriers with the lattice.

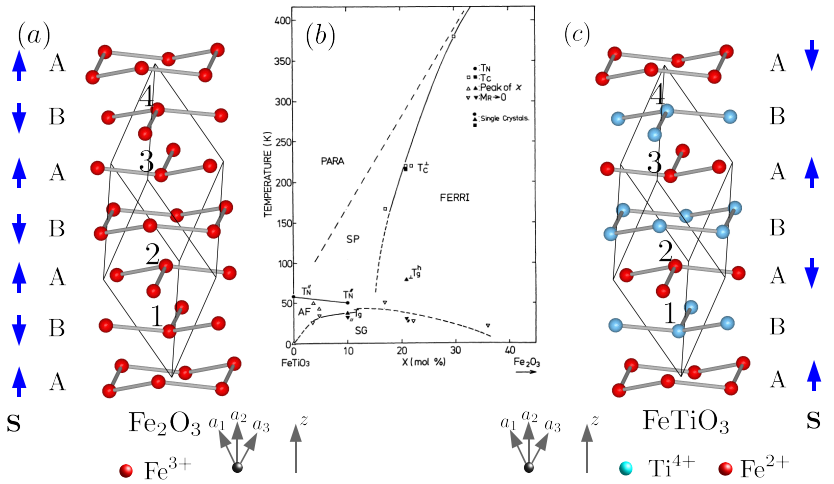

Figure 6.1: Crystal structure of α-hematite (a) and ilmenite (c). In both cases the positive ions arrange in the approximately hexagonal planes A and B stacked along the z direction. In Ilmenite the Ti^{4+} and Fe^{2+} ions alternate in neighboring planes. The blue arrows on the sides represent the magnetic ordering at temperature below the Morin transition (a) and the Néel temperature of ilmenite (c). The magnetic phase diagram (b) obtained experimentally by Ishikawa [1] for the solid solution series of the two minerals. The phases are: antiferromagnetic (AF), ferrimagnetic (FERRI), spin glass (SG), superparamagnetic (SP) and paramagnetic (PARA).

First we briefly discuss the crystal structure and the magnetic ordering of Fe_2O_3 and $FeTiO_3$. As shown in Fig. 6.1 (a), α-hematite has a corundum structure with the so-called Bernal stacking of hexagonal layers of Fe ions along the z axis. Its rhombohedral unit cell contains four aligned iron ions and has the same structure and space group ($R\bar{3}c$) as Cr_2O_3 [see Fig. 1.1 (a)]. Below $T = 950$ K, α-hematite shows the C-type ($\uparrow\downarrow\downarrow\uparrow$) antiferromagnetic ordering [see Eq.(4.8)] with spins parallel to the Fe layers and a small ferromagnetic component along the c axis. At $T = 260$ K, the so-called Morin transition to the purely C-type antiferromagnetic state with spins oriented along the c axis [see Fig. 6.1 (a)] takes place [2; 3]. In this phase spins of Fe ions are parallel within the same layer and antiparallel to spins in neighboring layer [see Fig. 6.1 (a)].
Ilmenite has a similar crystal structure in which Ti^{4+} ions (S=0) occupy the positions 1 and 4 in the rhomboehedral unit cell, while Fe^{2+} ions (S=2) occupy the positions 2 and 3 [see Fig.6.1(c)]. This corresponds to the alternate stacking[2] of Ti and Fe hexagonal layers. Ilmenite undergoes a transition into an antiferromagnetic phase at $T = 68$ K [4; 5]. In the antiferromagnetic state the spins of Fe^{2+} are aligned along the z direction, they are parallel within one hexagonal plane and antiparallel to spins in neighboring layers [see Fig.6.1(c)].

[2]Note that ions in consecutive hexagonal layers do not always correspond to consecutive ions in a single rhombohedral unit cell.

We now discuss the crystal structure and the magnetic phase diagram of the solid solution series. Magnetic properties of solid solutions $(1-x)FeTi_3 - xFe_2O_3$ have been widely studied experimentally [1; 5; 6; 7; 8]. At temperatures higher than the magnetic transition temperature, a structural transition from a state where the cations are disordered in the A and B layers [see Figs.6.1 (a) and (c)] to the one where Ti^{4+} is present only in the B layers occurs[3] [11; 12; 13; 14]. In the latter state, the crystal has a structure similar to ilmenite where some non-magnetic Ti ions have been replaced by magnetic Fe ions. The spin of Fe ions in the A layers strongly couples antiferromagnetically to those of Fe impurities in the neighboring B layers. This interaction results in a local effective ferromagnetic coupling between the magnetic moment in the B layers and frustrates the anti-alignment of magnetic moments of neighboring A hexagonal planes.
The experimental phase diagram is shown in Fig. 6.1(b). For $x \lesssim 0.15$, the solid solution undergoes a phase transition to an antiferromagnetic state at approximately the same transition temperature as $FeTiO_3$. At lower temperatures a transition to a spin glass state occurs. Above the antiferromagnetic transition, in the disordered phase, there are two distinct regions: a paramagnetic region and a superparamagnetic one, where the magnetic susceptibility has the same feature as in the paramagnetic state but is much larger in size. For concentrations $0.15 \lesssim x \lesssim 0.5$ there is a transition from the high-temperature superparamagnetic state into a ferrimagnetic state, in which the saturation magnetization decreases linearly with increasing concentration. At much lower temperatures the spin glass state sets in.
In this chapter we study how magnetic Fe ions inserted in the Ti layers affect the ilmenite magnetic order, restricting ourselves to the low-x limit. We consider a simplified model in which spins are arranged in a square lattice instead of in hexagonal layers. In the first section we introduce the model and discuss the changes in the spin ordering in the A-layers from the spin alignment within the A planes caused by frustration induced by the spin of a single impurity inserted in the B layer. In particular, we characterize the size and the geometry of this deformation to which we refer as magnetic polaron. Then we study the effective interaction between two magnetic polarons. In the third section we discuss the Monte Carlo simulations performed for a large set of concentrations and temperatures. Finally, we discuss the Monte Carlo results, the obtained phase diagram and the superparamagnetic behavior. Our results show that the picture of interacting magnetic polarons explains magnetic properties of ilmenite-hematite solid solutions.

6.2 Size and geometry of a single magnetic polaron[4]

In the first part of this section we introduce our model describing spin interactions in a solid solution and then we discuss the structure of a single magnetic polaron.

[3] This makes the magnetic properties of the sample very sensitive to the heat treatment [9] and allows for the existence of nanoscale antiphase domains upon rapid cooling through the transition temperature [10].

[4] The work presented in this sections was done in collaboration with S. Artyukhin and A.C. Berceanu. The results shown in Fig. 6.3 were obtained by S. Artyukhin.

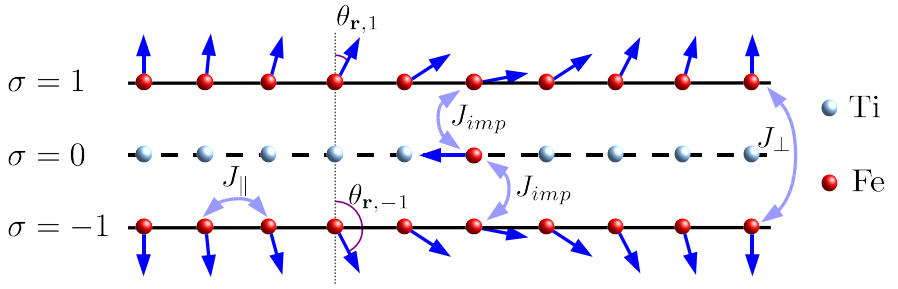

Figure 6.2: Sketch of the model Eq.(6.1) for the case of a single Fe impurity in the Ti layer ($\sigma = 0$) sandwiched between two Fe layers ($\sigma = \pm 1$). The arrows represent the spin arrangement in the polaron configuration.

In the case of $FeTiO_3$ we consider a cubic lattice of spins consisting of alternating magnetic (A) and non-magnetic (B) square layers. We label these layers with the index σ, which takes odd and even values for, respectively, A and B layers. The spins of nearest-neighbor ions within the same (A) layer are coupled ferromagnetically with an exchange constant $J_\parallel$, while spins of neighboring magnetic layers are coupled antiferromagnetically with a coupling constant $J_\perp$. For the case of a solid solution with a concentration x we consider the same model with xN_L spins, where N_L is the number of ions randomly positioned in B layers. As shown in Fig. 6.2, those spins couple antiferromagnetically to the spins of nearest-neighbor ions with an exchange coupling J_{imp}.
The Hamiltonian of the model reads

$$H = \sum_{\langle \mathbf{r},\mathbf{r}'\rangle,\sigma} J_\parallel \mathbf{S}_{\mathbf{r},\sigma} \cdot \mathbf{S}_{\mathbf{r}',\sigma} + \sum_{\mathbf{r},\langle\langle\sigma,\sigma'\rangle\rangle} J_\perp \mathbf{S}_{\mathbf{r},\sigma} \cdot \mathbf{S}_{\mathbf{r}',\sigma'} + \sum_{i,k=\pm 1} J_{imp} \mathbf{s}_i \cdot \mathbf{S}_{\mathbf{r}_i,\sigma_i+k}, \tag{6.1}$$

where $\mathbf{S}_{\mathbf{r},\sigma}$ is the spin in the σ layer at the position $\mathbf{r}$ in the plane, σ and σ' take only odd values, $\mathbf{s}_i$ is the spin of the i-th impurity which has the position $\mathbf{r_i}$ and is located in the layer σ_i and $\langle \dots \rangle$ and $\langle\langle \dots \rangle\rangle$ indicates, respectively, that the sum is performed over nearest and next-nearest-neighbors. The large difference between the Néel temperatures of hematite and ilmenite suggests that J_{imp} is the largest energy scale in the model, whereas $J_\perp$ is the smallest energy scale, since it couples spins between next-nearest-neighbor layers. Therefore, we assume $J_{imp} > |J_\parallel| > J_\perp$.

Next we discuss the shape of the magnetic polaron induced by a single impurity between the layers in the ground state. To calculate the shape of the polaron we consider a magnetic impurity at $\mathbf{r} = 0$ and $\sigma = 0$ sandwiched between two magnetic layers at $\sigma = \pm 1$. Spins at arbitrary large distances from the impurity are affected negligibly by its presence, they order in the same way as in ilmenite and are oriented along the z direction[5]. Since the in-plane coupling is ferromagnetic and $|J_{||}| > J_\perp$,

[5]The Hamiltonian Eq.(6.1) is invariant under global rotations of the spins $\mathbf{S}_{\mathbf{r},\sigma}$ and $\mathbf{s}_{\mathbf{r}_i}$. Therefore, the

we assume that in the lowest-energy state all spins lie in the same plane, $\mathbf{S}_{\mathbf{r},\sigma} = (\sin\theta_{\mathbf{r},\sigma}, 0, \cos\theta_{\mathbf{r},\sigma})$ [see Fig. 6.2]. This assumption has been checked numerically using the parallel tempering method. Furthermore, the symmetry argument of Appendix 6.A proves that in the ground state $\theta_{\mathbf{r},-1} = \pi - \theta_{\mathbf{r},1}$, while the spin of the dopant is orthogonal to the z axis. This observation drastically simplifies finding the polaron configuration and allows us to write Eq.(6.1) for the spins of the magnetic layer $\sigma = 1$ as follows,

$$H_{2D} = 2J_{\parallel} \sum_{\langle \mathbf{r}\mathbf{r}' \rangle} \cos(\theta_{\mathbf{r}} - \theta_{\mathbf{r}'}) - J_{\perp} \sum_{\mathbf{r}} \cos(2\theta_{\mathbf{r}}). \tag{6.2}$$

At large distances from the impurity, the ferromagnetic exchange between Fe ions within the same plane forces $\theta_{\mathbf{r}}$ to vary smoothly and, therefore, the continuum approximation holds. The way to obtain the minimal value, $\tilde{r}_{min}$, of separation from the impurity above which this approximation holds will be discussed below. Assuming the continuum limit to be a good approximation for the discrete model for $r > \tilde{r}$, Eq.(6.2) can be written as

$$H_{2D} \approx E_D(\theta_{\tilde{r}}) + 4\pi J_{\parallel} a^2 \int_{\tilde{r}}^{\infty} d\varrho\varrho \left[(\partial_{\varrho}\theta)^2 - \frac{1}{4}\cos(2\theta) \right], \tag{6.3}$$

where $\varrho = \frac{r}{r_0} = \frac{r}{a}\sqrt{\frac{J_{\perp}}{J_{\parallel}}}$, a is the lattice constant and $E_D(\theta_{\tilde{r}})$ is a the energy for the discrete lattice for $r < \tilde{r}$ and $\theta = \theta_{\tilde{r}}$ at its boundary. The profile of $\theta(r)$ at $r > \tilde{r}$ can be found by minimizing the functional Eq.(6.3) with respect to θ. For distance $r \gg r_0$, the spins within one layer are approximately aligned along z and the expansion $\sin(2\theta) \approx 2\theta$ allows us to write the Euler-Lagrange equation for the functional Eq.(6.3) as

$$\partial_{\varrho}^2\theta + \frac{1}{\varrho}\partial_{\varrho}\theta = \theta. \tag{6.4}$$

The solution to the above equation is given by $\theta_{\varrho} = C_B K_0(\varrho)$, where $K_0(\varrho)$ is the so-called Mac Donald function [15], which, in the limit $\varrho \gg 1$, decays as $\theta(\varrho) \sim \frac{e^{-\varrho}}{\sqrt{\varrho}}$. Using this solution, one gets $H_{2D} \approx E_D(\theta_{\tilde{r}}) + 4\pi J_{\parallel} a^2 C_B^2 f(\tilde{r}/r_0)$, where $\theta(\tilde{r}) = C_B K_0(\tilde{r}/r_0)$ and $f(\tilde{r})$ is obtained substituting $\theta(\varrho)$ by $K_0(\varrho)$ in the integral Eq.(6.3). At the core of the polaron, the continuum limit is not valid and the energy $E_D(\theta_{\tilde{r}})$ of the spin lattice has to be minimized numerically with respect to the variables $\theta_{\mathbf{r}}$ where $|\mathbf{r}| < \tilde{r}$. After matching the solution of the discrete and continuum model at the boundary, we obtain the profile of the polaron by minimizing the total energy with respect to the variables $\theta_{\mathbf{r}}$ for $r < \tilde{r}$ and C_B. Then, we check the independence of the solutions on $\tilde{r}$ by increasing its value. For the case $J_{imp} \gg J_{\parallel}$, the solution θ_r is plotted in Fig. 6.3 for different ratios $J_{\perp}/J_{\parallel}$. This figure shows that even for small

direction of the spins at the boundaries with respect to the crystalline axis is non relevant if no other anisotropic term in considered.

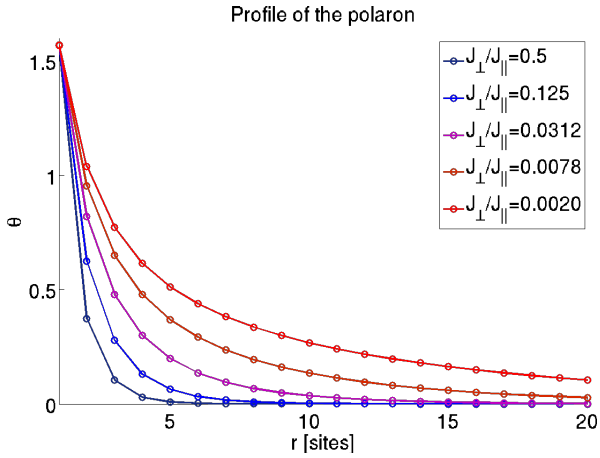

Figure 6.3: Dependence of angle θ of the spin distortion on the distance from the impurity for different values of the ration $J_\perp / J_\parallel$. The results were obtained by minimizing the energy of an hybrid system consisting of the lattice Hamiltonian Eq.(6.2) on the core of the polaron and the continuum mode Eq.(6.3) outside the core as described in the text.

ratios $J_\perp / J_\parallel \approx 2 \cdot 10^{-3}$ a minimal value $\tilde{r}_{min} \approx 15a$ justifies Eq.(6.3).
Since $\theta_{\mathbf{r},-1} = \pi - \theta_{\mathbf{r},1}$, the z component of the magnetization carried by the polaron vanishes. However, the polaron carries a large magnetization $\boldsymbol{\mu}$ oriented along the x direction and, even at ratios $J_\parallel / J_\perp \sim 0.1$, this magnetization is large compared to the one carried by a single spin, $\mu \gg g\mu_B S$. Moreover, since no anisotropy is considered in our model, states with different directions of $\boldsymbol{\mu}$ within the xy plane are degenerate.
It is important to notice that our model we do not take into account the different valence of the iron ions in the ilmenite layers (Fe^{2+}) and in Ti layers (Fe^{3+}). Indeed, the hole present in the $3d$ electronic structure of the dopant can hop to the layers and effectively change the exchange couplings of the core spins by the double exchange mechanism. Throughout this chapter we neglect this effect by assuming all holes to be localized and we leave the investigations in the presence of hopping holes for future studies.

6.3 Interaction between polarons

So far we assumed that all magnetic impurities are separated by distances large compared to r_0 and at temperatures $k_B T \ll J_\perp$. We now consider the case of two impurities with spins, $\mathbf{s}_1$ and $\mathbf{s}_2$, located in the same Ti layer at distance r_{12}.
When the distance r_{12} between the two impurities is comparable with r_0, the polarons, which they induce, overlap. The ferromagnetic exchange stiffness within the two planes favors parallel magnetizations of impurities. The energy of the configuration with two close impurities is lower than twice the energy of an isolated polaron. This results in an effective interaction J_{eff} between $\mathbf{s}_1$ and $\mathbf{s}_2$, which strongly depends on

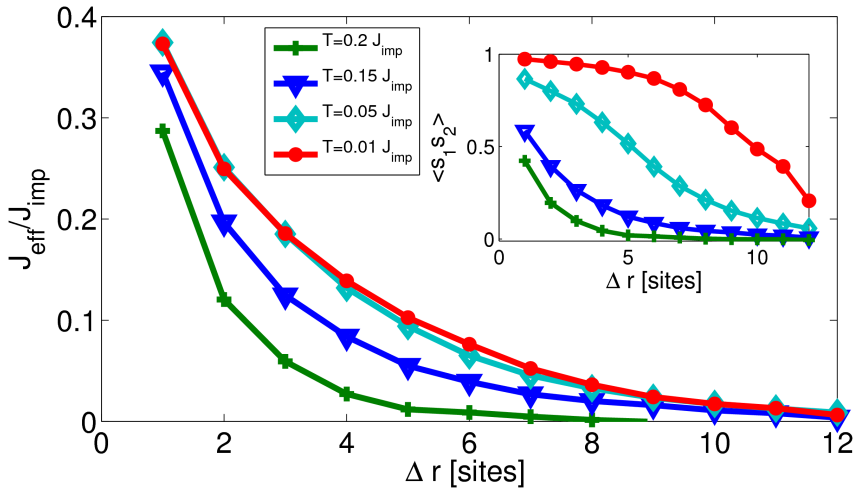

Figure 6.4: Distance dependence of the effective interaction between the spins of the two impurities at various temperatures. The values of the effective interaction were obtained by the correlation $\langle \mathbf{s}_1 \mathbf{s}_2 \rangle$ (in-set). The parameters used are: $J_{\parallel} = -0.2 J_{imp}$, $J_{\perp} = 0.01 J_{imp}$.

r_{12}. Furthermore, at non-zero temperatures, the interaction will be affected by spin fluctuation in the ferromagnetic layers.
We study the dependence of J_{eff} on the distance r_{12} and on the temperature T by Monte Carlo simulations. An effective exchange coupling, J_{eff}, between the spins of the two impurities can be obtained by calculating their correlation function $\langle \mathbf{s}_1 \cdot \mathbf{s}_2 \rangle$ and using:

$$\langle \mathbf{s}_1 \cdot \mathbf{s}_2 \rangle \equiv \int d\mathbf{s}_1 \int d\mathbf{s}_2 \, (\mathbf{s}_1 \cdot \mathbf{s}_2) \, e^{-\beta J_{eff} \mathbf{s}_1 \cdot \mathbf{s}_2} = \coth\left(\beta J_{eff}\right) - \frac{1}{\beta J_{eff}}, \tag{6.5}$$

where $\beta = 1/(k_B T)$. Monte Carlo simulations of the model Eq.(6.1) were performed for the case of two iron ions sandwiched between two layers, $\sigma = \pm 1$, of magnetic ions. Open boundary conditions were used.
Figure 6.4 shows the dependence of the effective interaction and of $\langle \mathbf{s}_1 \cdot \mathbf{s}_2 \rangle$ [see inset Fig. 6.4] on r_{12} obtained for the coupling constants $J_{\parallel} = -0.2 J_{imp}$ and $J_{\perp} = 0.01 J_{imp}$. The value of J_{eff} rapidly decreases with increasing the distance r_{12} and temperature. At temperatures slightly below $J_{\parallel}/k_B$ [see Fig. 6.4 for $T = 0.15 J_{imp}$], the interaction strong up to distances ~ 10 lattice sites.
The results above show that the spins of the two impurities and the magnetic moments carried by the two polarons, are coupled ferromagnetically through the long range interaction resulting from the polarons overlap. However, the interaction calculated by the method above is only meaningful for very low concentrations of impurities. There are two main reasons for this. First, by considering only two magnetic layers

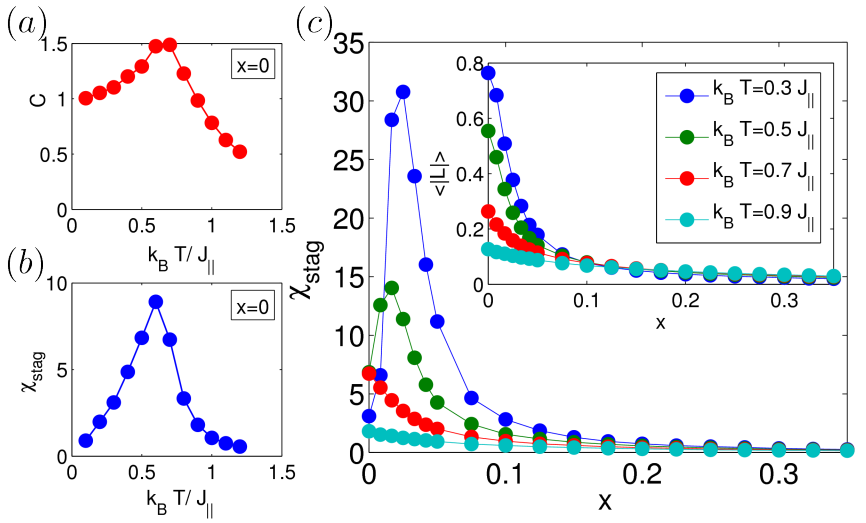

Figure 6.5: Temperature dependence of specific heat (a) and staggered susceptibility (b) for the case of no impurity between the magnetic layers ($x = 0$). Dependence of the staggered susceptibility and the antiferromagnetic order parameter (inset) on the dopant concentration (c) for various temperatures.

we do not take into account the overlap of polarons induced by dopants inserted in different Ti layers. Second, when three or more impurities are located in the same layer at distances comparable with r_0 within each other, their spins cannot be considered anymore coupled via an effective two-spin interaction.

6.4 Monte Carlo simulations

To take into account these effects, we performed Monte Carlo calculations for a three-dimensional lattice consisting of few Fe^{2+} layers. In this section we shortly describe some details of these calculations and discuss their results.
The numerical calculations are done for various values of x and the temperature T. Since the overlap between polarons created by iron impurities strongly depends on their separation, some attention should be paid to the way in which the impurities are positioned in the lattice. Indeed, it is important to avoid that the results of the simulation are biased by a single realization of the impurities' positions. To prevent this, we averaged over different realizations of the lattice by adopting the following strategy. At the beginning of the Monte Carlo algorithm a fixed number of impurities is placed in each Ti layer using a uniform random distribution for their positions. After thermalization and the collection of a sufficiently large number of measurements for every observable, the positions of the impurities in every layer are changed again. This process is iterated up to the convergence of the observables.

We perform Monte Carlo calculation on a lattice of eleven square layers with 10×10 sites per layer with open boundary conditions. We choose the exchange couplings $J_{imp} = 6J_{\parallel}$ and $J_{\perp} = 0.06J_{\parallel}$, we consider $S = 1$ for both the ions in the magnetic layers and the impurities[6].
For $x = 0$ the magnetic ions are only in the layers labeled by odd σ and the antiferromagnetic order parameter can be written as $\langle L \rangle = \langle \frac{1}{N} \sum_{\mathbf{r},\sigma=odd} (-1)^{\frac{\sigma+1}{2}} S_i \rangle$. Figures 6.5 (a) and (b) show, respectively, the numerical results for the magnetic specific heat, C, and the staggered susceptibility $\chi_{stag} = N \frac{\langle L^2 \rangle - \langle L \rangle^2}{T}$ at $x = 0$. The peaks of $C(T)$ and $\chi_{stag}(T)$ occurring at $T_N^0 \approx 0.6J_{\parallel}$ indicate the transition from the paramagnetic to the antiferromagnetic state. The value of the critical temperature ($T_N^0 \gg J_{\perp}$) suggests that the transition is governed by the spin coupling within the planes. This is explained as follows. Even if the spins of an isolated plane cannot have long-range order, their correlation length $\xi(T)$ diverges as $T \to 0$ [16] and it can be large for $T \sim J_{\parallel}$. Therefore, at sufficiently low temperatures the antiferromagnetic interaction acts between correlated spins in the area $\pi\xi^2(T)$ and gives rise to an effective coupling between next-nearest-neighbor planes, of the size $\sim \pi\xi^2(T)J_{\perp}$. This results in a transition temperatures $T_N^0 \gg J_{\perp}$.
Let us turn now to the case of $x \neq 0$. As shown in the inset Fig. 6.5 (c), the value of $\langle L \rangle$ order parameter rapidally decreases as the concentration of impurities increases. At the same time, χ_{stag} increases enormously and has a peak at a value of x which increases as the temperature decreases [see Fig 6.5(c)]. This indicates that, fixing the temperature T below T_N^0, a small concentration of impurities destroys the long range antiferromagnetic order or, in other words, for small concentration of impurities the Néel temperature decreases as the x increases. Using the polaron picture described in the previous section, this can be explained as follows. The effective antiferromagnetic interaction, acting between spins in the area $\pi\chi^2(T)$ and working between next-nearest-neighboring layers, is reduced by the polaron deformations induced by the impurities. Due to the relatively large size of the polarons ($J_{\perp} = 0.06J_{\parallel}$) low concentrations ($x \gtrsim 0.03$) are sufficient to destroy the long range antiferromagnetic order. At low temperatures, where the effective interaction between the next-nearest-neighbor planes is stronger, a higher concentration of impurities is required to destroy the antiferromagnetic ordering.
The above reasoning, which holds for non-interacting polarons, is no longer valid for strongly overlapping polarons, i.e. as the concentration is further increased. Figure 6.6 shows the concentration dependence of the magnetic susceptibility χ and the magnetization M per magnetic ion [see inset Fig. 6.6] at various temperatures. The magnetic susceptibility shows a rather broad peak at the concentration $x_c(T)$, which varies with the temperatures. At $x_c(T)$, the magnetization jumps to a non-zero value and, increasing the concentration, rapidally reaches a maximal value and then decreases linearly. Note that, as the temperature increases, the value of x_c increases. In other words, in this concentration regimes, the Curie temperature increase as the value of x increases and, in particular, it can reach values higher than T_N.

[6]Considering classical spins the different values of S for the magnetic species results in the rescaling of the exchange coupling constants.

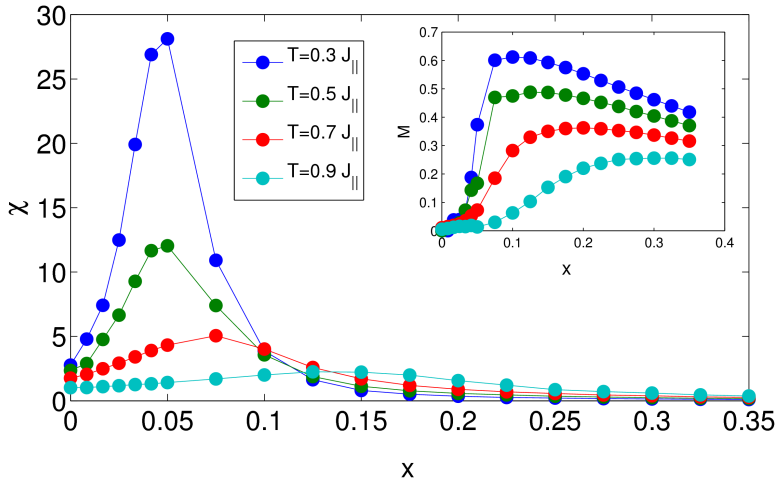

Figure 6.6: Concentration dependence of the magnetic susceptibility and magnetization (inset) per magnetic ion at various temperatures.

This transition is dominated by the effective interaction between magnetic polarons. At concentration $x < x_c(T)$ the iron impurities are, in average, far apart and the polaron-polaron interaction is extremely weak. At $x > x_c(T)$ their average distance is shorter and their interaction is sufficiently strong to favor the alignment of all their magnetic moments. To some extent, this can be pictured as the overcome of a percolation threshold of the large cluster of ferromagnetic moment created by overlapping polarons [1].
As the concentration is increased above x_c, two different effects compete and dictate the behavior of the magnetization. On the one hand, the insertion of impurities increases the strength of the ferromagnetic interaction between polarons and, therefore, increases the value of the magnetization. On the other hand, the magnetic moment of the added impurity is antialligned with respect to the magnetization, which results in a linear decrease of M as x is further increased. Increasing x, the trade off of this two effects results in the increase of M close to x_c and its linear decrease at higher concentrations.

6.5 Super-paramagnetism

We turn now to the discussion of the behavior of the magnetic susceptibility in the low concentration part of the phase diagram. In the regime of very low concentrations the overlap of the magnetic polarons is negligible and they can be considered as non-interacting. In this regime and at temperatures below T_N, one can picture the magnetic structure of the diluted solid solution as a set of magnetic distortions trapped in the ilmenite type antiferromagnetic texture. Since the polaron-polaron

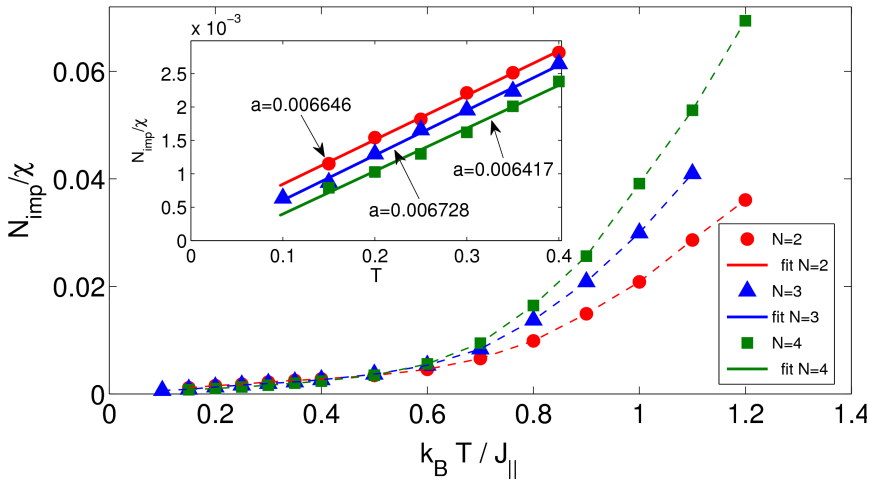

Figure 6.7: Temperature dependence of the inverse magnetic susceptibility multiplied by the impurity concentration for the values $x =$. The linear behavior at low T coincide with the superparamagnetic regime. For low x, the slopes obtained by the linear fit of the low temperature data (in-set) are nearly independent on the concentration and according to Eq.(6.6) correspond to a polaron size $\sim 17.5S$.

interaction is negligible, the magnetic moment, $\boldsymbol{\mu}_i$, which is carried by the polaron localized near the i-th impurity, is uncorrelated from the one induced by other impurities. Furthermore, the rotation of the magnetic moment of every polaron does not cost energy, i.e. it is a zero-mode. Indeed, as described in Sec. 6.2, all states obtained by rotations of the magnetization of a single polaron in the xy plane are degenerate. The presence of large weakly interacting in-plane magnetic moments gives rise to superparamagnetic behavior and explains the large values of the magnetic susceptibility [see Fig. 6.6] at low x.

At low temperatures, the magnetic fluctuations related to the rotations of $\boldsymbol{\mu}_i$ in the same planes are much large than the fluctuations in the collinear antiferromagnetic state. When the fluctuations of the size of the polarons are negligible, the magnetization is temperature-independent and $\mu_i = \mu$. Therefore, the temperature dependence of the magnetic susceptibility can be described by the Curie-Weiss law for the planar magnetic moments with magnitude μ:

$$\chi = \frac{x\mu^2}{2T}, \tag{6.6}$$

where χ is the magnetic susceptibility per spin.

Figure 6.7 shows the Monte Carlo results for the temperature dependence $\alpha(T) = \frac{N_{imp}}{N\chi(T)}$ of the inverse total magnetic susceptibility multiplied by the number of impu-

rities N_{imp} for $N_{imp} = 1, 2, 3$. At high temperatures $\alpha(T)$ reaches the linear regime correspondent to the Curie-Weiss law for the full spin lattice[7]. At low temperatures ($T \sim 0.5 J_{\|}$) $\alpha(T)$ reaches another linear regime where its slope is independent on x [see the inset in Fig. 6.7]. This proves that the non-interacting polaron picture is correct. Moreover, Eq.(6.6) allows to extract the values $\mu \sim 17.5 S g \mu_B$ by using the slopes obtained from the linear fit of low-temperature data.

6.6 Comments and conclusions

In conclusion, we study the magnetic properties of ilmenite when magnetic impurities are inserted in the Ti layers between antiferromagnetically coupled ferromagnetic Fe planes. We characterize the size and the shape of the magnetic deformation of the collinear antiferromagnetic state induced by the strong coupling between the spin of the impurity and the spins of the ions in neighboring layers. These magnetic polarons carry a large magnetic moment and their overlap induces an effective long-range ferromagnetic interaction between them. In Monte Carlo simulations, we obtain the antiferromagnetic, ferrimagnetic and superparamagnetic states observed experimentally. At low concentrations and low temperatures, the large magnetic moments carried by weakly-interacting polarons give rise to superparamagnetic behavior. The ferrimagnetic transition, which occurs as the concentration of polarons increases, results from ferromagnetic interactions between the polarons.
We note that our model does not take into account the effect induced by the different valences of Fe ions in ilmenite and hematite. The hopping of the holes from dopant ions to Fe layers induces double-exchange interactions which modify the geometry of the polaron and its symmetry, i.e. the hole hopping decreases the antiferromagnetic interaction of the impurity's spin with the spin of one of the neighbors layers making the magnetic deformation from the ferromagnetic state larger in the other one. Interestingly, this leads to an electric dipole induced by the charge of the hole that is coupled to the magnetic structure of a single polaron. For the case of a single polaron, this effect introduces a novel microscopic magnetoelectric coupling that has neither exchange-striction origins nor relativistic ones.

[7] Note that the different slopes are due to the multiplication by N_{imp}.

6.A Appendix A: Considerations on the shape of an isolated magnetic polaron

In this appendix we show that the minimal energy state for isolated distortion has the symmetry described in Sec. 6.2. Consider a magnetic impurity sandwiched between the two spin layers at $\sigma = \pm 1$. At arbitrary large distances from the impurity the spins of the two layers are anti-alligned and they can be assumed to be parallel to $\mathbf{z}$. For coplanar spins we parametrize $\mathbf{S}_{\mathbf{r},\pm 1} = \sin\theta_{\mathbf{r},\pm 1}\mathbf{x} + \cos\theta_{\mathbf{r},\pm 1}\mathbf{z}$ and $\mathbf{s} = \sin\psi\mathbf{x} + \cos\psi\mathbf{z}$. To show that the lowest energy state is such that

$$\theta_{\mathbf{r},-1} = \pi - \theta_{\mathbf{r},1}, \tag{6.7}$$

we adopt the following strategy. We consider a generic state $\{\{\theta_{\mathbf{r},1}\},\{\theta_{\mathbf{r},-1}\},\psi\}$ with the only assumption that for nearest-neighbors spins in $\mathbf{r}$ and $\mathbf{r}'$ the relation $|\theta_{\mathbf{r},1} - \theta_{\mathbf{r}',-1} + \theta_{\mathbf{r},1} - \theta_{\mathbf{r}',-1}| \leq \pi$ holds. This assumption is justified by the ferromagnetic interaction between spins in the same layer. From this state we construct a new state state that satisfies 6.7. Then, we show that the latter state has a lower energy. The energy Eq.(6.1) of the arbitrary spin state is

$$E_1 = J_{\parallel}\sum_{\langle \mathbf{r},\mathbf{r}'\rangle,\sigma=\pm 1}\cos\left(\theta_{\mathbf{r}',\sigma} - \theta_{\mathbf{r},\sigma}\right) + J_{\perp}\sum_{\mathbf{r}}\cos\left(\theta_{\mathbf{r},1} - \theta_{\mathbf{r},-1}\right) + J_{imp}\sum_{\sigma=\pm 1}\cos\left(\theta_{0,\sigma} - \psi\right). \tag{6.8}$$

Consider now the energy E_2 of the "symmetrized" state $\{\{\frac{\pi+\theta_{\mathbf{r},1}-\theta_{\mathbf{r},-1}}{2}\},\{\frac{\pi-\theta_{\mathbf{r},1}+\theta_{\mathbf{r},-1}}{2}\},-\frac{\pi}{2}\}$. The energy difference $\Delta_E = E_2 - E_1$ reads

$$\begin{aligned}
\Delta E &= J_{\parallel}\sum_{\langle \mathbf{r},\mathbf{r}'\rangle}\left[2\cos\left(\frac{\theta_{\mathbf{r},1}+\theta_{\mathbf{r},-1}}{2} - \frac{\theta_{\mathbf{r}',1}+\theta_{\mathbf{r}',-1}}{2}\right) - \sum_{\sigma=\pm 1}\cos(\theta_{\mathbf{r}\sigma} - \theta_{\mathbf{r}',\sigma})\right] + \\
&- J_{imp}\sum_{\sigma=\pm 1}\left[2\cos\left(\frac{\theta_{0,1}-\theta_{0,-1}}{2}\right) + \sum_{\sigma=\pm 1}\cos\left(\theta_{0,\sigma} - \psi\right)\right] \\
&= J_{\parallel}\sum_{\langle \mathbf{r},\mathbf{r}'\rangle}\left[2\cos\Phi^{+}_{\mathbf{r}\mathbf{r}'}\left(1 - \cos\Phi^{-}_{\mathbf{r},\mathbf{r}'}\right)\right] - J_{imp}\left[2\cos\Psi^{+}\left(1-\cos\Psi^{-}\right)\right],
\end{aligned} \tag{6.9}$$

where $\Phi^{\pm}_{\mathbf{r},\mathbf{r}'} = \frac{(\theta_{\mathbf{r},1}-\theta_{\mathbf{r},1})\pm(\theta_{\mathbf{r},-1}-\theta_{\mathbf{r},-1})}{2}$, $\Psi^{+} = \frac{\theta_{0,1}-\theta_{0,-1}}{2}$ and $\Psi^{-} = \frac{\theta_{0,1}+\theta_{0,-1}-2\psi}{2}$. Since $J_{\parallel} < 0$, $J_{imp} > 0$ and $|\Phi^{+}_{\mathbf{r}}|, |\Psi^{-}| \leq \pi/2$, the energy difference between the two states is always smaller then or equal to zero, $\Delta E \leq 0$.

Bibliography

[1] Ishikawa, Y., Saito, N., Arai, M., Watanabe, Y., and Takei, H. *Journal of the Physical Society of Japan* **54**(1), 312–325 (1985).

[2] Morin, F. J. *Phys. Rev.* **78**(6), 819–820 Jun (1950).

[3] S.A. Bashanov, K. D. and Zhetbaev, A. In *Applications of Mössbauer Effect*, Kagan, Y. and Lyubutin, I., editors, 425–428. Gordon and Breach Science Publisher, (1985).

[4] Shirane, G., Pickart, S., Nathans, R., and Ishikawa, Y. *Journal of Physics and Chemistry of Solids* **10**(1), 35 – 43 (1959).

[5] Ishikawa, Y. and iti Akimoto, S. *Journal of the Physical Society of Japan* **12**(10), 1083–1098 (1957).

[6] Arai, M., Ishikawa, Y., and Takei, H. *Journal of the Physical Society of Japan* **54**(6), 2279–2286 (1985).

[7] Arai, M., Ishikawa, Y., Saito, N., and Takei, H. *Journal of the Physical Society of Japan* **54**(2), 781–794 (1985).

[8] Navarrete, L., Dou, J., Allen, D. M., Schad, R., Padmini, P., Kale, P., and Pandey, R. *Journal of the American Ceramic Society* **89**, 1601–1604 (2006).

[9] Ishikawa, Y. *Journal of the Physical Society of Japan* **17**(12), 1835–1843 (1962).

[10] Hojo, H., Fujita, K., Mizoguchi, T., Hirao, K., Tanaka, I., Tanaka, K., and Ikuhara, Y. *Phys. Rev. B* **80**(7), 075414 Aug (2009).

[11] Harrison, R. J. and Redfern, S. A. T. *Physics and Chemistry of Minerals* **28**, 399–412 (2001). 10.1007/s002690100167.

[12] Harrison, R. J. *Geochem. Geophys. Geosyst.* **10**, Q02Z02 (2009).

[13] Ishikawa, Y. *Journal of the Physical Society of Japan* **13**(8), 828–837 (1958).

[14] Shirane, G., Cox, D. E., Takei, W. J., and Ruby, S. L. *Journal of the Physical Society of Japan* **17**(10), 1598–1611 (1962).

[15] Abramowitz, M. and Stegun, I. *Handbook of Mathematical Functions*. Dover Publications, Inc., New York, (1965).

[16] Takahashi, M. *Phys. Rev. Lett.* **58**(2), 168–170 Jan (1987).

7

Characterizing the low energy magnetic excitations of YMn_2O_5[1]

In this chapter we consider the non-collinear incommensurate magnetic state of YMn_2O_5 and study its magnetic excitations. By considering a minimal spin model we obtain the couplings that give rise to a magnetic structure similar to the one found experimentally and classify the low-energy magnetic modes. We calculate inelastic neutron scattering intensity and compare it with experiment values [2]. Furthermore, we identify the magnons which are strongly coupled to polar phonons (electromagnons), estimate the spectral weight of the lowest frequency one and compare it the experimental value.

7.1 Introduction

Many spectacular magnetoelectric phenomena were found in manganese oxides. In hexagonal $YMnO_3$ magnons strongly mix with acoustic phonons [1], magnetic domain walls are firmly clamped ferroelectric domain walls [2], which gives rise to unusual magnetoelectric vortices [3]. In orthorombic $AMnO_3$ compounds with A = Tb, Dy, (EuY), an incommensurate spiral spin ordering induces electric polarization through the relativistic "inverse Dzyaloshinskii-Moriya mechanism" [4; 5; 6; 7]. These

[1]This chapter is based on J.-H. Kim, M.A. van der Vegte, A. Scaramucci, S. Artyukhin, J.-H.Chung, S. Park, S.-W. Cheong, M. Mostovoy and S.-H. Lee, arXiv:1008.5354 (submitted to Physical Review Letters)

[2]The inelastic neutron scattering results were obtained by our coworkers S.-H. Lee and J.-H. Kim, respectively, at the Department of Physics, University of Virginia, Charlottesville and the Max-Plank-Institute for Solid State Research in Stuttgart. The work presented in this chapter it is a part of a work done in collaboration with M.A. van der Vegte and S. Artyukhin.

compounds show magnetically-induced polarization flops, giant magnetocapacitance and electromagnon peaks in optical absorption [8; 9; 10; 11]. Smaller-sized cations on A-sites, e.g. Ho, favor a commensurate collinear magnetic ordering, whose polarization, induced by the non-relativistic Heisenberg magnetoelectric coupling, is an order of magnitude larger than that of the spiral state [12].

Similar competition between collinear and non-collinear ferroelectric states is found in orthorombic AMn_2O_5 compounds. Also in this family electric polarization is larger in collinear states, while electromagnons and giant magnetocapacitance are observed in non-collinear states [13; 14; 15]. As we will describe below, YMn_2O_5, which is the subject of this chapter, exhibits a rather complex chain of magnetic phase transitions which leads below ~ 40 K to two phases where magnetic order induces ferroelectricity. Just below $T \sim 40$ K, spins order in a commensurate state (CM) and are approximately collinear, while, at lower temperatures, a transition to an incommensurate phase[3] (ICM), where spins are non-collinear, occurs. Together with this magnetic transition, also a ferroelectric phase transition occurs. The electric polarization, **P**, which is oriented along the b direction and is rather large in the CM phase ($P_{CM} \sim 900\ \mu C/m^2$), drops to a lower magnitude ($P_{ICM} \sim 250\ \mu C/m^2$) and has the opposite direction in the ICM state. The magnitude of of P in the CM phase suggests that the main magnetoelectric coupling giving rise to ferroelectricity originates from non-relativistic interactions.

Moreover, the low-energy optical spectra of these two phases look very different. As we will briefly discuss below, the third-order coupling between the antiferromagnetic order parameter and electric polarization, which was discussed in section 1.3.2, not only allows for a spontaneous electric polarization but also couples polar lattice vibrations to oscillation of the magnetic order, i.e. magnons. Therefore, some magnons can be coupled indirectly to the electric field of light via the magnetoelectric coupling to polar phonons. This gives rise to the so-called *electromagnon* excitations. Recent optical experiment [15; 16] carried by Sushkov *et al.* revealed the presence of three electromagnon peaks in the optical absorption spectrum of the ICM phase. In the CM phase the peak with the lowest frequency ($\omega = 7.2\ cm^{-1}$), which has the highest spectral weight, disappears while the other two strongly decrease in intensity and merge to form a single broad peak. This, together with the change in the electric polarization of the two phases, suggests that the magnetoelectric coupling giving rise to the electromagnon excitations and spontaneous polarization might be the same.

To understand the way in which electromagnons arise it is of fundamental importance to study magnetic excitations in this material and their properties. This was done experimentally by our collaborators by using inelastic neutron scattering techniques. In this chapter we study the electric and magnetic field excitation of magnons in YMn_2O_5 by considering a minimal spin model which reproduces the intensity scans obtained by inelastic neutron scattering and has the minimal energy state with approximately the same spin order as the ICM phase. In the first section we review the magnetic structure of the CM and the ICM phases of YMn_2O_5. Next we introduce our model describing interactions of spins and the coupling of spins to electric field. After a brief discussion of the methodology used, we calculate the inelastic neutron

[3] In the literature this phase is often called low temperature incommensurate (LTI) phase.

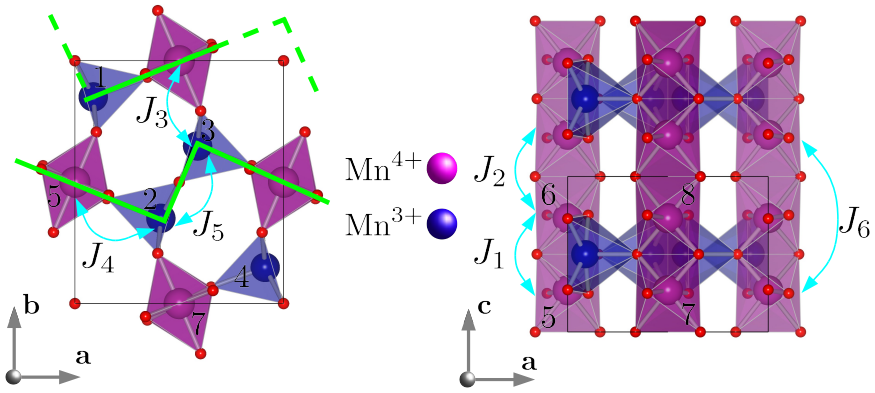

Figure 7.1: Crystal structure of YMn_2O_5 in the *ab* (left panel) and *bc* (right panel) plane. Blue spheres represent Mn^{3+} ions, which are coordinate in by five oxygens ions in a square pyramid geometry, while purple spheres represent $Mn^{4}+$ ions, which are in an octahedral environment. The blue arrows represent the different exchanges between the ions. The green lines represent the two Mn^{4+}-Mn^{3+}-Mn3+ (zigzag) chains along the *a* direction.

scattering intensities for the low energy magnetic excitations and compare our results with experimental data. We show that this low energy excitations can be classified as "acoustic" and "optical". Optical magnons can strongly couple with polar modes of the lattice, and give rise to the electromagnon excitations. In the last section of this chapter we discuss their origin and calculate the spectral weight of the electromagnon with the lowest frequency.

7.2 Crystal and magnetic structure

In this section we briefly describe the crystal structure of YMn_2O_5 and the magnetic ordering in the CM and ICM phase. YMn_2O_5 has an orthorhombic unit cell and *Pbam* space symmetry group [17; 18]. Figure 7.1 shows its crystallographic unit cell which contains four Mn^{3+} ($S = 2$) ions and four Mn^{4+} ($S = 3/2$). Mn^{3+} ions, which we label by $i = 1, 2, 3, 4$ [see Fig.7.1], are coordinated by five oxygens in a square pyramid geometry, while the Mn^{4+} ions, which we label by $i = 5, 6, 7, 8$, are coordinated by six oxygens in octahedral geometry MnO_6. In the *ab* plane, following the green line of Fig.7.1, pairs of neighboring MnO_6 octahedra along the *c* direction together share a corner with their neighboring MnO_5 square pyramid along the *a* direction. Along the same direction, this pyramid is followed by another MnO_5 with which it shares an edge. This coordination pattern gives rise to chains along the *a* direction which are composed by pairs of MnO_6 alternating with two consecutive MnO_5 [see Fig. 7.1]. Throughout this chapter we shall refer to these chains as zig-zag chains. A similar chain structure is also realized along the *b* direction with the only difference that, in this case, single MnO_6 shares a corner with MnO_5. To distinguish these chains from

those realized along a, we refer to them as Mn^{4+}-Mn^{3+}-Mn^{3+} chains. Along the c direction, MnO_6 octahedra are edge-sharing.
In the past ten years a lot of efforts have been spent in the experimental study of the magnetic and ferroelectric phase diagram of RMn_2O_5 [13; 19; 20; 21]. These phase diagrams share a lot of similarities and, apart from little details [4], they undergo the same chain of magnetic transitions. Let us consider the case of YMn_2O_5. At $T_N = 45$ K this compound undergoes a phase transition to a modulated antiferromagnetic state. In this state the spin ordering has a wave vector $\mathbf{q} = (q_a, 0, q_c)$ and is incommensurate with the lattice constant both along the a and c crystallographic directions[19; 22]. Lowering the temperature down to $T_{FE} = 40.8$ K, a first lock-in transition [19] to a modulated state with $\mathbf{q} = (\sim 0.492, 0, \frac{1}{4})$ occurs. At the same temperature a ferroelectric transition from the paraelectric phase to a state with electric polarization, $\mathbf{P}$, oriented along $\hat{\mathbf{b}}$, occurs. Decreasing the temperature by ≈ 0.8 K, YMn_2O_5 undergoes a second lock-in transition, to a fully commensurate (CM) magnetic state with $\mathbf{q} = (\frac{1}{2}, 0, \frac{1}{4})$. This state also possesses a spontaneous electric polarization which can reach values up to $P \sim 900\ \mu C/m^2$ [23]. At $T_I = 18.5$ K, another transition to an incommensurate (ICM) antiferromagnetic state with $\mathbf{q} \approx (0.48, 0, 0.288)$ occurs. As mentioned above, this state possesses an electric polarization oriented in the opposite direction with respect to the one of the CM state and much lower in magnitude.
As shown in Fig.7.2, the magnetic orderings of the latter two phases do not only differ on their wave vector but also on the relative orientation of the spins. In the CM phase the spins are approximately collinear and they form a state in which the b Mn^{4+}-Mn^{3+}-Mn^{3+} chains have approximately the magnetic order $\uparrow\uparrow\downarrow$ along the b direction [see dashed box in Fig. 7.2 (a)]. This magnetic state breaks inversion symmetry and induces an electric polarization oriented along the b direction through exchange-strictive coupling. The non-relativistic origin of the magnetoelectric coupling explains the rather large magnitude of $\mathbf{P}$. In the LTI phase, spins of neighboring ions in the b Mn^{4+}-Mn^{3+}-Mn^{3+} chains form approximately a ± 90 angle [see dashed box in Fig. 7.2 (b)]. This explains the strong decrease of the induced electric polarization, which, for the case of exchange-striction mechanism, is proportional to the scalar product of spins.

7.3 Spin model and magnetoelectric coupling

We now switch to the discussion of the minimal spin model necessary to obtain a spin ordering close to the one of YMn_2O_5 in the ICM phase which will be used below to calculate magnons properties. As noted by Radaelli *et al.* [24], the crystal structure of YMn_2O_5 allows for three in-equivalent exchange paths between nearest-neighbor Mn ions within the ab planes. Following their notation, we label the coupling constant relative to those exchange as J_3, J_4 and J_5 [see Fig. 7.1]. Figure 7.1 shows that the ions coupled by these three exchanges form pentagonal loops. This loop geometry, for the

[4] Y, Er and Tm have an intermediate transition to a phase which is incommensurate with the lattice only in one direction. Furthermore, RMn_2O_5 containing magnetic R ions displays another transition at very low temperatures.

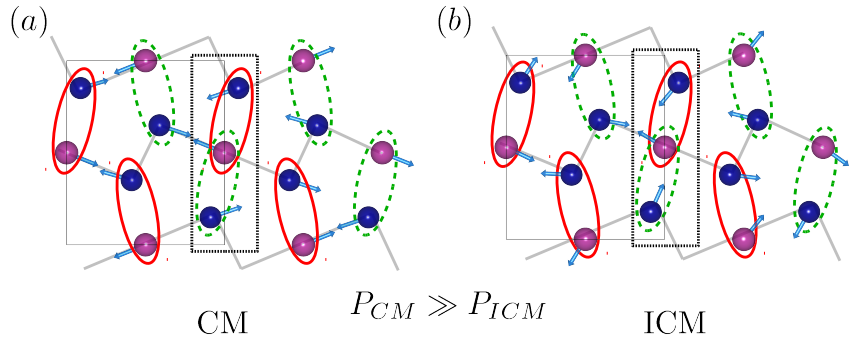

Figure 7.2: Sketch of the spin ordering in the *ab* plane in the commensurate (a) and incommensurate magnetic phase of YMn_2O_5. In the commensurate phase, spins of ions in neighboring zig-zag chains, which are represented by gray lines, are approximately collinear, whereas, in the incommensurate phase they are approximately perpendicular. The red solid (green dashed) ellipses represent bonds in which parallel (antiparallel) spins favors electric polarization along the positive *b* direction according to the coupling Eq. (7.2). The resulting electric polarization in the commensurate phase is larger in the CM phase.

case of antiferromagnetic exchanges, strongly frustrates the spin ordering, giving rise to a modulation of the spins. Moreover, in absence of anisotropies, the competition of these three different exchanges gives rise to the 90° arrangement of spins of Mn ions belonging to neighboring zig-zag chains along *b*.
The couplings along the *c* direction have a less clear origin. At the present time the mechanism which determines the spin modulation along the *c* is not fully understood. Although such a modulation might be the result of of spin-lattice interactions [25; 26], we follow Ref.[24] and we consider an exchange interaction acting between next-nearest-neighboring Mn^{4+} ions along c [see Fig. 7.1] which competes with the one occurring between nearest-neighboring ions. The spin Hamiltonian reads

$$H = \frac{1}{2}\sum_{\mathbf{r},\mathbf{r}',i,j} J^{ij}_{\mathbf{r},\mathbf{r}'}\mathbf{S}^i_{\mathbf{r}}\cdot\mathbf{S}^j_{\mathbf{r}'} - \Delta_a\sum_{\mathbf{r},i}(\mathbf{v_i}\cdot\mathbf{S}^i_{\mathbf{r}})^2 + \sum_{\mathbf{r},i}\Delta_{p,i}(S^c_{\mathbf{r}})^2, \tag{7.1}$$

where $\mathbf{r}$ is the position of the crystallographic unit cell, the indexes $i, j = 1, \dots 8$ labels the magnetic ions and the exchange couplings are listed in Tab. 7.1. In the model Eq.(7.1) we include easy axis magnetocrystalline anisotropies on the Mn^{3+} sites with strength $\Delta_a = 0.15$ meV and axes $v_i = (0.96, \pm 0.26, 0)$. Moreover, we include easy plane anisotropies for both Mn^{3+} and Mn^{4+} with strength, respectively, $\Delta_{p1} = 0.09$ meV and $\Delta_{p2} = 0.05$ meV.
Let us now discuss the form of the magnetoelectric coupling mentioned in the previous section. The expression of this coupling can be inferred by symmetry argument. The generators[5] of the *Pbam* symmetry group are the inversion $\mathcal{I}$, the two-fold rota-

[5]Here we omit the identity operator.

exchange	coupled ions	values
J_1	$5 \leftrightarrow 6, 7 \leftrightarrow 8$	-0.4 meV
J_2	$5 \leftrightarrow 6-c, 7 \leftrightarrow 8-c$	-1.8 meV
J_3	$5(6) \leftrightarrow 1, 5(6) \leftrightarrow 4-a, 7(8) \leftrightarrow 2, 7(8) \leftrightarrow 3-b$	0.2 meV
J_4	$5(6) \leftrightarrow 2, 5(6) \leftrightarrow 3-a, 7(8) \leftrightarrow 4, 7(8) \leftrightarrow 1-b$	3.0 meV
J_5	$1 \leftrightarrow 4-a+b, 2 \leftrightarrow 3$	4.1 meV
J_6	$5(6) \leftrightarrow 5+c(6+c), 7(8) \leftrightarrow 7+c(8+c)$	0.8355 meV

Table 7.1: Exchange coupling constants used in the model Eq.7.1. The numbers in brackets are the labels of ions which have the same coupling.

tion around the c axis, 2_c, and the two-fold rotation around the b direction followed by a translation of half unit cell along the same axis, $\tilde{2}_b$. The transformation of the lattice sites and the b component of the electric field under these generators are summarized in Tab. 7.2. The magnetoelectric coupling originated by non-relativistic mechanism has to be linear in the electric field and in the scalar product of spins. Furthermore, it has to be invariant under the transformations listed in Tab. 7.2. It is that easy to check that the term

$$H_{ME} = -gP_b \sum_{\mathbf{r}} \left[(\mathbf{S}^1_{\mathbf{r}} - \mathbf{S}^4_{\mathbf{r}-\mathbf{a}}) \cdot (\mathbf{S}^5_{\mathbf{r}} + \mathbf{S}^6_{\mathbf{r}}) + (\mathbf{S}^2_{\mathbf{r}} - \mathbf{S}^3_{\mathbf{r}-\mathbf{b}}) \cdot (\mathbf{S}^7_{\mathbf{r}} + \mathbf{S}^8_{\mathbf{r}}) \right], \tag{7.2}$$

where g is the coupling constant, satisfies these requirements. This coupling involves only scalar products of pair of spins in neighboring zig-zag chains. Therefore, the spontaneous induced electric polarization drops as the spins of neighboring chains become approximately perpendicular.

7.4 Magnetic excitations

Before discussing the results for the properties of the low energy excitation of the ICM magnetic phase of YMn_2O_5, we briefly explain the methodology used. To the purpose of calculating the magnetic excitations of the model Eq.(7.1) it is of fundamental importance to know its ground state. The calculation of such ground state is challenging because of the incommensurability of the magnetic ordering. Since the wave vector, $\mathbf{q}_{ICM} = (\frac{1}{2} - \epsilon_a, \frac{1}{4} - \epsilon_c)$, is close to a commensurate value and, more importantly, since the magnetoelectric properties are only related to the relative angle of spins of neighboring chains, to overcome this problem we use parameters of the model Eq.(7.1), which gives a ground state with wave vector $\mathbf{q}_{th} = (\frac{1}{2}, 0, \frac{1}{4})$. These parameters are obtained by the following procedure. We first consider model Eq.(7.1) in absence of anisotropies and numerically minimize the "spiral" Ansatz:

$$\mathbf{S}^i = S^i \left(\cos(\phi_i + \mathbf{k} \cdot \mathbf{r}) \hat{\mathbf{a}} + \sin(\phi_i + \mathbf{k} \cdot \mathbf{r}) \hat{\mathbf{b}} \right), \tag{7.3}$$

	1	2	$3-\mathbf{b}$	$4-\mathbf{a}$	5	6	7	8	$E_b(P_b)$
$\mathcal{I}$	4	3	$2+\mathbf{b}$	$1+\mathbf{a}$	$6+\mathbf{a}$	$5+\mathbf{a}$	$8+\mathbf{b}$	$7+\mathbf{b}$	$-E_b(-P_b)$
2_c	4	3	$2+\mathbf{b}$	$1+\mathbf{a}$	$5+\mathbf{a}$	$6+\mathbf{a}$	$7+\mathbf{b}$	$8+\mathbf{b}$	$-E_b(-P_b)$
$\tilde{2}_b$	$2+\mathbf{b}$	1	$4-\mathbf{a}$	3	$8+\mathbf{b}$	$7+\mathbf{b}$	6	5	$E_b(P_b)$

Table 7.2: Transformation of the site of YMn_2O_5 and the electric field (electric polarization) along b direction under generators of the space group $Pbam$. The generators are the inversion ($\mathcal{I}$), the 180° rotation around the c axis (2_c), and the 180° rotation around the b axis followed by a translation of half unit cell along the same axis ($\tilde{2}_b$). The sum Eq.(7.2) is invariant under these transformations.

where i labels the magnetic ions in the crystallographic unit cell, with respect to ϕ_i and $\mathbf{k}$. Then, we tune the exchange coupling constants to obtain $\mathbf{k} = \mathbf{q}_{th}$. The tuned couplings are used for minimizing the full Hamiltonian Eq.(7.1) (including anisotropy terms) for a lattice consisting of $2 \times 1 \times 4$ crystallographic unit cells with periodic boundary conditions. The stability of the resulting ground state configuration is proved by checking that the magnons have purely real frequencies for all the values of their wave vector.
By tuning the parameters and adopting this procedure we were able to obtain a set of couplings [see Tab. 7.1] which gives magnon dispersion and intensities for the inelastic neutron scattering close to the experimental one, a magnetic ground state similar to the ICM state and also allows us to explain the origin of the electromagnon peaks. It is important to note that the ground state of our model is fully coplanar, i.e. all the spins are in the ab plane, while, in the ICM state, the spins are not fully coplanar and posses a modulated component in the c direction.
Once the ground state configuration $\mathbf{S}^0_\mu$, where $\mu = 1, \ldots, 64$ labels the Mn ions in the magnetic unit cell, is known, we find the frequencies of the magnetic oscillation by solving the linearized equations of motion for spins' oscillations in the classical limit of large spins. To this purpose, it is convenient to consider these oscillations in the reference frame of spins in the ground state [see appendix 7.A]. Thus, we introduce the unit vectors $\hat{\mathbf{n}}_\mu = \mathbf{S}_\mu / S_\mu$, $\hat{\mathbf{e}}_\mu = \hat{\mathbf{c}} \times \hat{\mathbf{n}}_\mu$ which, together with the unit vector along the c direction $\hat{\mathbf{c}}$, form a orthogonal basis. Moreover, to discuss the magnon properties it is convenient to consider magnetic unit cells instead of crystallographic ones. We denote by $\mathbf{R}$ the position of the magnetic unit cell and by $\mathbf{r}_\mu$ the position of the μ-th ions inside it. To the linear approximation, the deformation of the μ-th spin $\mathbf{S}_{\mu,\mathbf{R}}$ from the ground state $\mathbf{S}^0_\mu$ is

$$\mathbf{S}_{\mu,\mathbf{R}} - \mathbf{S}^0_{\mu,\mathbf{R}} = s^{\parallel}_{\mu,\mathbf{R}} \hat{\mathbf{e}}_\mu + s^{\perp}_{\mu,\mathbf{R}} \hat{\mathbf{c}}, \tag{7.4}$$

where $s^{\parallel}_{\mu,\mathbf{R}}, s^{\perp}_{\mu,\mathbf{R}} \ll S_\mu$. The equations of motion for $s^{\parallel}_{\mu,\mathbf{R}}$ and $s^{\perp}_{\mu,\mathbf{R}}$ under this approximation are obtained in appendix 7.A and are conveniently written in the Fourier

representation $\tilde{s}_\nu^{\parallel(\perp)}(\mathbf{q},\omega) = \sum_{\mathbf{R}} s_{\nu,\mathbf{R}}^{\parallel(\perp)} e^{-i(\mathbf{q}\cdot\mathbf{R}-\omega t)}$. In this representation they read[6]

$$\begin{aligned} i\omega\tilde{s}_\mu^{\perp}(\mathbf{q}) &= \frac{\tilde{A}_{\mu\nu}(\mathbf{q})}{S_\nu}\tilde{s}_\nu^{\parallel} \\ i\omega\tilde{s}_\mu^{\parallel}(\mathbf{q}) &= \frac{\tilde{B}_{\mu\nu}(\mathbf{q})}{S_\nu}\tilde{s}_\nu^{\perp}, \end{aligned} \tag{7.5}$$

where the matrices $\tilde{A}_{\mu\nu}$ and $\tilde{B}_{\mu\nu}$ are described in appendix 7.A and the summation over the repeated indexes is implied. The solution of the above equations, which can be obtained by numerical diagonalization, gives the normal modes for the spin oscillations and their dispersion relations.

7.4.1 Acoustic and optical low energy magnons

We switch now to the description of the spin deformation from the ground state in lowest frequency magnon modes obtained by solving Eq.(7.5). There are in total six modes that give rise to the low energy magnon band the model Eq.(7.1) and they can be understood by analogy with the low energy excitation of a spin spiral.
Consider the case of a simple spin spiral state where spins lie in the *ab* plane. As Senff *et al.* [27] noticed, the low energy excitation of this state are, in the general case, three. The so-called "phason" or sliding mode involves rotations in the *ab* plane and in the same direction of all the spins, i.e. a change of the phase of the spiral state. This mode is a Goldstone mode of any incommensurate spiral state. It has zero energy irrespective to the magnitude of higher harmonics in the spiral. However, it becomes gaped for commensurate states in the presence of certain anisotropies, i.e. an easy axis anisotropy. The other two low-energy spiral modes are the rotation of the *ab* spiral plane around the *a* and the *b* axis. The presence of an anisotropy term makes these modes also gaped and, furthermore, it can split their energy. It is important to note that all these modes occur at a zero wave vector in the spiral reference frame.
The ICM magnetic state of YMn_2O_5 differs from the spin spiral case because of the presence of two zig-zag chains (each one with a spiral spin order) in the unit cell. The peculiar lattice geometry of AMn_2O_5 leads to and almost complete cancellation of exchange interactions between neighboring zig-zag chains [see Fig. 7.2], resulting in close energies of magnon branches of "acoustic" and "optical" analogues of the spiral modes. In the acoustic modes, the rotation of spins of neighboring zig-zag chains happens in the same direction [see Fig. 7.3 (a) and (c)], whereas in the optical modes it happens in opposite directions [see Fig.7.3 (b) and (d)]. The frequencies of this modes are shown by the peaks in Fig.7.4 (a). The frequency of the acoustic phason is determined by the strength of the easy axis anisotropy which also determines the energy splitting between the rotations around the *a* and *b* axes. The energy splittings occurring between the rotations and the phason are dependent on the easy plane anisotropies strengths. The frequency differences between acoustic and optical modes depend on the interchain coupling constant J_3.

[6]Here we consider the equation of motion in absence of an external magnetic field

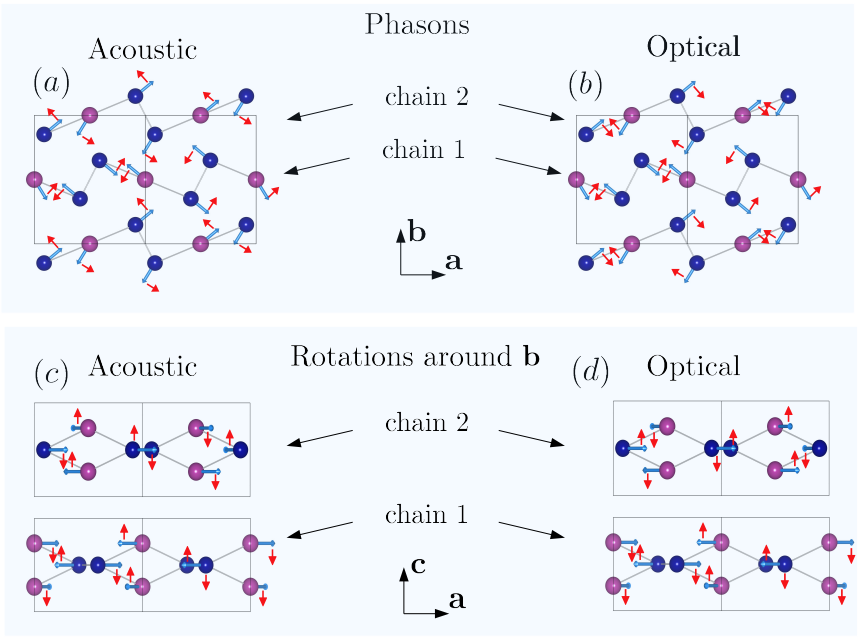

Figure 7.3: Sketch of four of the six lower energy magnetic modes with zero wave vector in the spins' co-rotating frame. Since the crystallographic unit cell contains two weakly coupled (due to frustration) zig-zag chains, to every magnetic mode of a chain correspond two magnetic modes for the spins in the crystallographic unit cell. Thus, magnons can be classified as "acoustic" and "optical". The panels show the deformations (red arrows) of the spins (blue arrows) of Mn ions in neighboring zig-zag chains (chain 1 and chain 2) along c for four of these spin modes. For the acoustic (a) and optical (b) phason the deformation are in the ab plane, whereas, for acoustic (c) and optical rotations (d) around b in the ac plane. The acoustic and optical rotation around the a axes are not shown.

7.4.2 Inelastic neutron scattering intensities

To compare our model with the experimental results we calculate the inelastic neutron scattering intensities. This is done by calculating the dynamic magnetic susceptibility [see appendix 7.A], $\chi(\mathbf{Q},\omega)$, to the oscillating magnetic field induced by the neutrons. This field is described by the transfer wave vector, $\mathbf{Q}$, in the lab frame. The scattering cross section can be calculated as [28]

$$\mathcal{I}(\mathbf{Q},\omega) \propto \coth\left(\frac{\hbar\omega}{2k_BT}\right) \sum_{i,j=a,b,c} (\delta_{i,j} - \hat{\mathbf{Q}}_i\hat{\mathbf{Q}}_j) Im(\chi_{ij}(\mathbf{Q},\omega)), \tag{7.6}$$

where the indexes i and j label the space directions, δ_{ij} is the Kroneker symbol and $Im(\chi(\mathbf{Q},\omega))$ is the imaginary part of $\chi(\mathbf{Q},\omega)$.
The acoustic modes correspond to global rotations of the spins in both the zig-zag

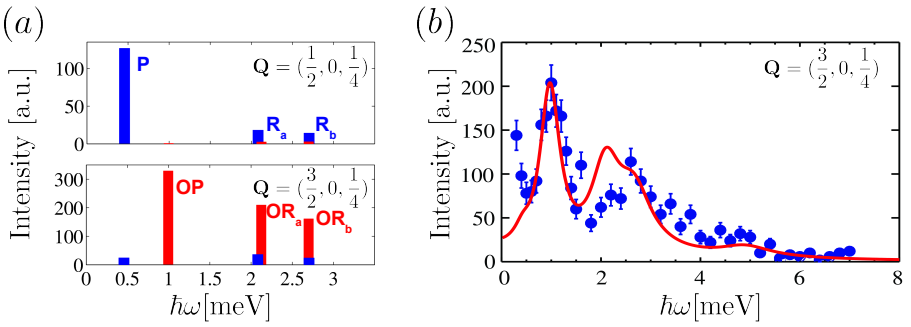

Figure 7.4: Intensities and frequencies (a) of the low energy magnons at $\mathbf{Q} = \left(\frac{1}{2}, 0, \frac{1}{4}\right)$ (top panel) and $\mathbf{Q} = \left(\frac{3}{2}, 0, \frac{1}{4}\right)$ (bottom panel). P, Ra and R$_b$ indicate, respectively, the phason and the rotation around a and b, whereas OP, OR$_a$ and OR$_b$ indicate their optical counterparts. The comparison between the calculated intensities and the experimental values (b) at $\mathbf{Q} = \left(\frac{3}{2}, 0, \frac{1}{4}\right)$.

chains and, in the spin co-rotating frame, they have a vanishing wave vector. The spin deformation in the acoustic phason and the acoustic rotations modes strongly overlap with, respectively, the in-plane and the out-of-plane component of an oscillating field with wave vector $\mathbf{Q} = \mathbf{q}_{ICM}$. This gives rise to intensity peaks at the frequencies corresponding to the energy of the acoustic modes at $\mathbf{q}_{ICM}$. The top panel of Fig. 7.4 (a) shows the energy and intensities of the calculated neutron scattering peaks corresponding to these six modes at $\mathbf{Q} = \left(\frac{1}{2}, 0, \frac{1}{4}\right)$ (the spiral wave vector). At this wave vector the intensities of the peaks corresponding to acoustic modes (blue color) are large, while the peaks corresponding to the optical modes are barely visible. At $\mathbf{Q} = \left(\frac{3}{2}, 0, \frac{1}{4}\right)$ [see fig. 7.4 (a) bottom panel] the situation is the opposite, which is related to the $\frac{a}{2}$ shift between neighboring zig-zag chains. The comparison of our results with the inelastic neutron scattering data is done by calculating the intensities at $\mathbf{Q} = \left(\frac{3}{2}, 0, \frac{1}{4}\right)$ once the broadenings of the peaks are taken into account. To this purpose, we calculate the intensity Eq.(7.6) when the frequency is shifted by a small imaginary part, $\omega \to \omega + i\frac{\gamma}{2}$. This gives rise to a Lorentzian broadening of the magnons' peaks. Figure 7.4 (b) shows the result of this calculation (red line) and the neutron scattering intensities (blue dots) at $\mathbf{Q} = (1, 0, 0) + \mathbf{q}_{ICM}$.

7.5 Electromagnons

The strong magnetoelectric coupling in YMn_2O_5 in addition to inducing a rather large spontaneous $\mathbf{P}$ in the CM phase also mixes magnon and phonon excitations. An oscillating electric field along the b direction causes polar vibrations of the lattice

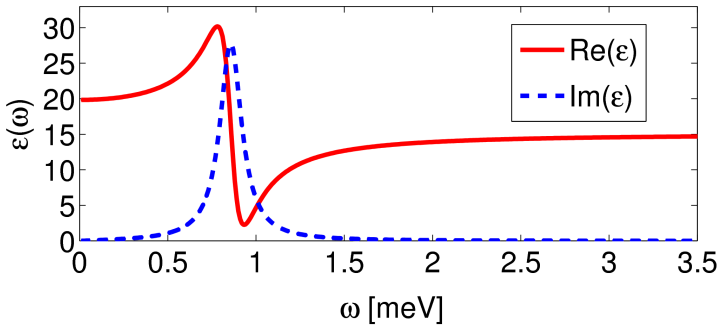

Figure 7.5: Frequency dependence of the dielectric function ϵ. The continuous red line is the real part of $\epsilon(\omega)$, while the dashed blue line is its imaginary part.

which, through the magnetoelectric coupling linear[7] in $\mathbf{P}$ can excite a magnon. This allows for the excitation of some of the magnons by the electric field of light and causes the transfer of the electric dipole spectral weight from phonon frequencies to magnon frequencies.

Consider the coupling Eq.(7.2). The electric field of light, $\mathbf{E}(\omega)$, applied along the positive b direction, induces polar oscillations of the lattice which result in a modulation of the coupling between neighboring zig-zag chains along the b direction, e.g. $J_{1,5(6)} \rightarrow J_{1,5(6)} + \Delta J$ (and equivalently $J_{2,7(8)} \rightarrow J_{2,7(8)} + \Delta J$) while $J_{4-\mathbf{a},5(6)} \rightarrow J_{4-\mathbf{a},5(6)} - \Delta J$ (and equivalently $J_{3-\mathbf{b},7(8)} \rightarrow J_{3-\mathbf{b},7(8)} + \Delta J$). This induces an increase (decrease) of the angle of pairs of spins surrounded by the red continuous (green dashed) ellipses in Fig. 7.2 (b) and results in the relative rotation of spins in neighboring zig-zag chains. Therefore, the magnetic excitations induced by the electric field of light through the coupling Eq.(7.2) are optical magnons.

To check this scenario, we calculate the spectral weight of the optical phason for the model Eq.(7.1) when the coupling Eq.(7.2) is present. As discussed by Sushkov and co-workers [16] for the case of $TbMn_2O_2$, the dynamic dielectric susceptibility of such a model can be written as

$$\chi_{el}^{-1}(\omega) = \chi_0^{-1}\left(1 - \frac{\omega^2}{\omega_0^2}\right) - \frac{1}{V}\sum_{i,j} I_i \left[(BA - \omega^2)^{-1} B\right] I_j, \tag{7.7}$$

where χ_0 is the dielectric susceptibility, ω_0 is the bare frequency of the polar distortion and the sum over i, j is done over all the magnetic lattice sites. Here $I_i = g\sum_j C_{ij}[\mathbf{S}_i \times \mathbf{S}_j]_c$, where the elements of the matrix C_{ij} are equal to one for the pairs of spins connected by the coupling Eq.(7.2) and equal to zero otherwise. The coupling constant g can be estimated by using the value of the electric polarization in the CM state and

[7] Photo-excitation of magnons by the electric field of light can also be induced by other couplings, i.e. the fourth order coupling P^2M^2. However, these couplings lead to the excitation of multiple magnons and are much weaker.

the spin configuration which was obtained by neutron scattering experiments by Kim *et al* [22].
Figure 7.5 shows the frequency dependence of the real and imaginary parts of the dielectric constant $\epsilon(\omega) = 1 + 4\pi\chi_{el}(\omega)$ obtained in our model. The broadening of the imaginary part of $\epsilon(\omega)$ has been obtained by a small shift of the frequency in the complex plane $\omega \rightarrow \omega + i\frac{\gamma}{2}$ (with $\gamma = 0.15$ meV). The large absorption peak at $\omega = 0.9$ meV (0.72 cm^{-1}) corresponds to the lowest frequency electromagnon observed in the optical experiment of Sushkov *et al.*[15]. Moreover, the calculated frequency dependence of the dielectric constant allows us to estimate the spectral weight, S, of this electromagnon excitation. This gives $S = 226$ cm^{-2}, which is in reasonable agreement with the experimental values 170 cm^{-2} found by Sushkov *et al.* [15].
Finally, we notice that, in the case of large deviation of the ICM state from the flat spiral state, the coupling Eq.(7.2) can also explain the excitation of the optical rotation modes by the electric field of light, which would be compatible with the presence of the other two electromagnon excitations.

7.6 Conclusions

In conclusion, we studied the low energy magnetic excitations in the ICM phase of YMn_2O_5 using a minimal spin model. We considered a planar commensurate ordering with wave vector close to the experimental incommensurate one. We find the values of parameters of the model that reproduce the magnon dispersion, which we used to characterize the low energy excitations. Due to the presence of two weakly coupled zig-zag chains in the crystallographic unit cell, the low energy magnons belong to acoustic and optical branches. In acoustic excitations spins in neighboring zig-zag chains rotate in the same direction, while in optical magnetic modes they rotate in opposite directions. Furthermore, using symmetry arguments we obtained the magnetoelectric coupling which is responsible for the large electric polarization in the *b* direction in the CM magnetic phase. The same coupling, mixes the optical magnons with polar phonons giving rise to the lowest-frequency electromagnon excitation. For this mode we estimate the optical spectral weight, finding a value close to the experimental one.

7.A Appendix A: Linearized equations of motion and generalized susceptibility

In this appendix we first obtain the linearized equation of motion for the spin waves of model Eq.(7.1) when a oscillating magnetic field, $\mathbf{h}(\mathbf{q},\omega) = \mathbf{h}e^{-i(\omega t - \mathbf{q}\cdot\mathbf{r})}$, is applied. Then we calculate the dynamic magnetic susceptibility function, $\chi_{ij}(\mathbf{Q},\omega)$. Since we consider a commensurate state for the non collinear ICM phase [see sec. 7.4], it is convenient to switch notation from Eq.(7.1) and introduce the Greek indexes which labels the ions inside the magnetic unit cell, i.e. $\mu = 1,\ldots,64$. Considering the applied field the total Hamiltonian reads

$$H = H_0 - g\mu_B \sum_{\mathbf{R},\mu} \mathbf{S}_{\mu,\mathbf{R}} \cdot \mathbf{h}(\mathbf{q},\omega), \tag{7.8}$$

where $\mathbf{R}$ is the position of the magnetic unit cell, g is the giromagnetic factor (which we assume to be the same for all the ions) and μ_B is the Bohr magneton.
The Landau-Lifshitz-Gilbert equations of motion[8] for the spins are

$$\dot{\mathbf{S}}_{\mu,\mathbf{R}} = \frac{\partial H}{\partial \mathbf{S}_{\mu,\mathbf{R}}} \times \mathbf{S}_{\mu,\mathbf{R}}, \tag{7.9}$$

where $\dot{\mathbf{S}}_{\mu,\mathbf{R}}$ is the derivative of $\mathbf{S}_{\mu,\mathbf{R}}$ with respect to the time and we neglect the Gilbert damping term. It is convenient to consider the spin oscillations in the reference frame of the spin configuration and adopt the basis set $\hat{\mathbf{n}}_\mu$, $\hat{\mathbf{e}}_\mu$, $\hat{\mathbf{c}}$ described in section 7.4. By inserting the expressions Eq.(7.4) and retaining only the terms linear in $s^{\parallel}_{\mu,\mathbf{R}}$ and $s^{\perp}_{\mu,\mathbf{R}}$ one gets the set of coupled equations

$$\begin{cases} \dot{s}^{\perp}_{\mu,\mathbf{R}} = \sum_{\nu,\mathbf{R}'} A_{\mu,\mathbf{R},\nu,\mathbf{R}'} \frac{s^{\parallel}_{\nu,\mathbf{R}'}}{S_\mu} + g\mu_B S_\mu \mathbf{h}(\mathbf{q},\omega)\cdot\hat{\mathbf{e}}_\mu \\ \dot{s}^{\parallel}_{\mu,\mathbf{R}} = -\sum_{\nu,\mathbf{R}'} B_{\mu,\mathbf{R},\nu,\mathbf{R}'} \frac{s^{\perp}_{\nu,\mathbf{R}'}}{S_\mu} - g\mu_B S_\mu \mathbf{h}(\mathbf{q},\omega)\cdot\hat{\mathbf{z}} \end{cases}, \tag{7.10}$$

where

$$A_{\mu,\mathbf{R},\nu,\mathbf{R}'} = \left(\sum_{\varrho,\tilde{\mathbf{R}}} J_{\nu,\mathbf{R},\varrho,\tilde{\mathbf{R}}} \mathbf{S}^0_\varrho \cdot \mathbf{S}^0_\nu\right)\delta_{\mu\nu}\delta_{\mathbf{R}\mathbf{R}'} - J_{\mu,\mathbf{R},\nu,\mathbf{R}'}\mathbf{S}^0_\mu\cdot\mathbf{S}^0_\nu - \Delta_\mu S^2_\mu\left[(\mathbf{v}_\mu\cdot\hat{\mathbf{n}}_\mu)^2 - (\mathbf{v}_\mu\cdot\hat{\mathbf{e}}_\mu)^2\right] \tag{7.11}$$

and

$$B_{\mu,\mathbf{R},\nu,\mathbf{R}'} = \left(\sum_{\varrho,\tilde{\mathbf{R}}} J_{\nu,\mathbf{R},\varrho,\tilde{\mathbf{R}}} \mathbf{S}^0_\varrho \cdot \mathbf{S}^0_\nu\right)\delta_{\mu\nu}\delta_{\mathbf{R}\mathbf{R}'} - J_{\mu,\mathbf{R},\nu,\mathbf{R}'}S_\mu S_\nu + S^2_\mu\left(\Delta^{\parallel}_\mu(\mathbf{v}_\mu\cdot\hat{\mathbf{n}}_\mu)^2 - \Delta^{\perp}\right).$$

[8] Here we consider the classical limit valid for large spins.

(7.12)

The set of coupled equations (7.10) can be partially decoupled by passing to the Fourier transform $\tilde{s}_{\mu}^{\parallel(\perp)}(\mathbf{q}) = \sum_{\mathbf{R}} \tilde{s}_{\mu,\mathbf{r}}^{\parallel(\perp)} e^{-i(\mathbf{q}\cdot\mathbf{R}-\omega t)}$ which leads to the equations

$$\sum_{\nu} \begin{pmatrix} \frac{\tilde{A}_{\mu,\nu}(\mathbf{q})}{S_\nu} & i\omega\delta_{\mu\nu} \\ -i\omega\delta_{\mu\nu} & \frac{\tilde{B}_{\mu\nu}(\mathbf{q})}{S_\nu} \end{pmatrix} \begin{pmatrix} \tilde{s}_\nu^{\parallel} \\ \tilde{s}_\nu^{\perp} \end{pmatrix} = - \begin{pmatrix} g\mu_B S_\mu (\mathbf{e}\cdot\mathbf{h}) e^{i\mathbf{q}\cdot\mathbf{r}_\mu} \\ g\mu_B S_\mu (\mathbf{z}\cdot\mathbf{h}) e^{i\mathbf{q}\cdot\mathbf{r}_\mu} \end{pmatrix}, \tag{7.13}$$

where $\mathbf{r}_\mu$ is the position of the μ-th magnetic ion in the unit cell.

It is convenient to introduce the matrix $\tilde{B}'_{\mu,\nu} = \tilde{B}_{\mu,\nu}/S_\mu$ and the vectors $K_\mu^{\parallel} = g\mu_B S_\mu (\mathbf{e}_\mu \cdot \hat{\mathbf{h}}) e^{i\mathbf{q}\mathbf{r}_\mu}$ and $K^{\perp} = g\mu_B S_\mu (\mathbf{z}\cdot\hat{\mathbf{h}})$. Using this notation the solution to Eqs.(7.13) is:

$$\begin{cases} \tilde{s}_\mu^{\perp} &= \frac{1}{\left(\omega^2\mathcal{I} - \tilde{A}\tilde{B}'\right)_{\mu\varrho}} \left(H^{\perp} \tilde{A}_{\varrho\nu} K_\nu^{\perp} + i\omega H^{\parallel} K_\varrho^{\parallel} \right) \\ \tilde{s}_\mu^{\parallel} &= \frac{S_\mu}{\left(\omega^2\mathcal{I} - \tilde{B}'\tilde{A}\right)_{\mu\varrho}} \left(H^{\parallel} \tilde{B}'_{\varrho\nu} K_\nu^{\parallel} - i\omega H^{\perp} K_\varrho^{\perp} \right) \end{cases}, \tag{7.14}$$

where $\mathcal{I}$ denotes the identity matrix, $H^{\parallel} = \mathbf{h}\cdot\mathbf{z}$ and $H^{\perp} = |\mathbf{h} - H^{\parallel}\mathbf{z}|$ are the strength, respectively, of the out-of-plane and in-plane components of the magnetic field and the summation over repeated indexes is implied. To obtain the generalized susceptibility, we first calculate the Fourier component of the magnetic moment $\mathbf{M}(\mathbf{q})$ with wave vector $\mathbf{q}$ induced by the oscillating magnetic field with the same wave vector. This can be easily obtained from the solutions Eq.(7.14) as

$$\begin{pmatrix} M^a(\mathbf{q}) \\ M^b(\mathbf{q}) \\ M^c(\mathbf{q}) \end{pmatrix} = g\mu_B \sum_{\mu} \begin{pmatrix} (\mathbf{e}_\mu \cdot \mathbf{a}) e^{-i(\mathbf{q}\cdot\mathbf{r}_a)} s_\mu^{\parallel} \\ (\mathbf{e}_\mu \cdot \mathbf{b}) e^{-i(\mathbf{q}\cdot\mathbf{r}_a)} s_\mu^{\parallel} \\ e^{-i(\mathbf{q}\cdot\mathbf{r}_a)} s_\mu^{\perp} \end{pmatrix} \equiv \sum_{\mu} \begin{pmatrix} (K_\mu^a)^* s^{\perp} \\ (K_\mu^b)^* s^{\perp} \\ (K_\mu^c)^* s^{\parallel} \end{pmatrix}, \tag{7.15}$$

where we introduced $K_\mu^{a(b)} = g\mu_B \mathbf{e}_\mu^{a(b)} e^{i\mathbf{q}\cdot\mathbf{r}_\mu}$ and $K_\mu^c = g\mu_B e^{i\mathbf{q}\cdot\mathbf{r}_\mu}$. Combining the Eq.(7.15) together with Eq.(7.14) it is easy to obtain the generalized susceptibility

$$\begin{aligned} \chi^{ij}(\mathbf{q},\omega) &= (K_\mu^i)^* \left[\omega^2\mathcal{I} - \tilde{B}'\tilde{A}|\right]^{-1}_{\mu,\varrho} \tilde{A}_{\varrho\nu} K_\nu^j \\ \chi^{cc}(\mathbf{q},\omega) &= (K_\mu^c)^* \left[\omega^2\mathcal{I} - \tilde{A}\tilde{B}'\right]^{-1}_{\mu,\varrho} \tilde{B}'_{\varrho\nu} K_\nu^c \\ \chi^{ic}(\mathbf{q},\omega) &= -i\omega (K_\mu^i)^* \left[\omega^2\mathcal{I} - \tilde{B}'\tilde{A}\right]^{-1}_{\mu,\nu} K_\nu^c, \end{aligned} \tag{7.16}$$

where $i,j = a,b$ and the summation over repeated indexes is implied.

Bibliography

[1] Petit, S., Moussa, F., Hennion, M., Pailhès, S., Pinsard-Gaudart, L., and Ivanov, A. *Phys. Rev. Lett.* **99**(26), 266604 Dec (2007).

[2] Fiebig, M., Lottermoser, T., Frohlich, D., Goltsev, A. V., and Pisarev, R. V. *Nature* **419**, 818–820.

[3] Choi, T., Horibe, Y., Yi, H. T., Choi, Y. J., Wu, W., and Cheong, S. W. *Nat Mater* **9**(3), 253–258 Mar (2010). 10.1038/nmat2632.

[4] Kenzelmann, M., Harris, A. B., Jonas, S., Broholm, C., Schefer, J., Kim, S. B., Zhang, C. L., Cheong, S.-W., Vajk, O. P., and Lynn, J. W. *Phys. Rev. Lett.* **95**(8), 087206 Aug (2005).

[5] Katsura, H., Nagaosa, N., and Balatsky, A. V. *Phys. Rev. Lett.* **95**(5), 057205 Jul (2005).

[6] Sergienko, I. A. and Dagotto, E. *Phys. Rev. B* **73**(9), 094434 Mar (2006).

[7] Mostovoy, M. *Phys. Rev. Lett.* **96**(6), 067601 Feb (2006).

[8] Kimura, T., Goto, T., Shintani, H., Ishizaka, K., Arima, T., and Tokura, Y. *Nature* **426**(6962), 55–58 Nov (2003). 10.1038/nature02018.

[9] Goto, T., Kimura, T., Lawes, G., Ramirez, A. P., and Tokura, Y. *Phys. Rev. Lett.* **92**(25), 257201 Jun (2004).

[10] Pimenov, A., Mukhin, A. A., Ivanov, V. Y., Travkin, V. D., Balbashov, A. M., and Loidl, A. *Nat Phys* **2**(2), 97–100 Feb (2006). 10.1038/nphys212.

[11] Valdés Aguilar, R., Mostovoy, M., Sushkov, A. B., Zhang, C. L., Choi, Y. J., Cheong, S.-W., and Drew, H. D. *Phys. Rev. Lett.* **102**(4), 047203 Jan (2009).

[12] Sergienko, I. A., Şen, C., and Dagotto, E. *Phys. Rev. Lett.* **97**(22), 227204 Nov (2006).

[13] Hur, N., Park, S., Sharma, P. A., Ahn, J. S., Guha, S., and Cheong, S.-W. *Nature* **429**(6990), 392–395 (2004).

[14] Hur, N., Park, S., Sharma, P. A., Guha, S., and Cheong, S.-W. *Phys. Rev. Lett.* **93**(10), 107207 Sep (2004).

[15] Sushkov, A. B., Aguilar, R. V., Park, S., Cheong, S.-W., and Drew, H. D. *Phys. Rev. Lett.* **98**(2), 027202 Jan (2007).

[16] Sushkov, A. B., Mostovoy, M., Aguilar, R. V., Cheong, S.-W., and Drew, H. D. *Journal of Physics: Condensed Matter* **20**(43), 434210 (2008).
[17] Alonso, J. A., Casais, M. T., Martínez-Lope, M. J., Martínez, J. L., and Fernández-Díaz, M. T. *Journal of Physics: Condensed Matter* **9**(40), 8515 (1997).
[18] Kagomiya, I., Matsumoto, S., Kohn, K., Fukuda, Y., Shoubu, T., Kimura, H., Noda, Y., and Ikeda, N. *Ferroelectrics* **286**, 167–174 (2003).
[19] Kobayashi, S., Osawa, T., Kimura, H., Noda, Y., Kagomiya, I., and Kohn, K. *Journal of the Physical Society of Japan* **73**(6), 1593–1596 (2004).
[20] Chapon, L. C., Blake, G. R., Gutmann, M. J., Park, S., Hur, N., Radaelli, P. G., and Cheong, S.-W. *Phys. Rev. Lett.* **93**(17), 177402 Oct (2004).
[21] Higashiyama, D., Miyasaka, S., and Tokura, Y. *Phys. Rev. B* **72**(6), 064421 Aug (2005).
[22] Kim, J.-H., Lee, S.-H., Park, S. I., Kenzelmann, M., Harris, A. B., Schefer, J., Chung, J.-H., Majkrzak, C. F., Takeda, M., Wakimoto, S., Park, S. Y., Cheong, S.-W., Matsuda, M., Kimura, H., Noda, Y., and Kakurai, K. *Phys. Rev. B* **78**(24), 245115 Dec (2008).
[23] Chapon, L. C., Radaelli, P. G., Blake, G. R., Park, S., and Cheong, S.-W. *Phys. Rev. Lett.* **96**(9), 097601 Mar (2006).
[24] Radaelli, P. G. and Chapon, L. C. *Journal of Physics: Condensed Matter* **20**(43), 434213 (2008).
[25] Noda, Y., Kimura, H., Kamada, Y., Ishikawa, Y., Kobayshi, S., Wakabayashi, Y., Sawa, H., Ikeda, N., and Kohn, N. *Journal of the Korean Physical Society* **51**(2), 828–831 (2007).
[26] Chaudhury, R. P., dela Cruz, C. R., Lorenz, B., Sun, Y., Chu, C.-W., Park, S., and Cheong, S.-W. *Phys. Rev. B* **77**(22), 220104 Jun (2008).
[27] Senff, D., Link, P., Hradil, K., Hiess, A., Regnault, L. P., Sidis, Y., Aliouane, N., Argyriou, D. N., and Braden, M. *Phys. Rev. Lett.* **98**(13), 137206 Mar (2007).
[28] White, R. M. *Quantum Theory of Magnetism*. Springer-Verlag, 3rd edition, (2007).

8

Samenvatting

In het dagelijks leven hebben we continu te maken met magnetische en ferroelektrische materialen. Iedere keer dat we onze computer opstarten of onze pinpas gebruiken wordt de informatie die is opgeslagen in de magnetische of ferroelektrische componenten van de opslagapparatuur gelezen en verwerkt. De mogelijkheid om te schakelen tussen twee stabiele, macroscopische toestanden stelt ons in staat om deze materialen als informatieopslag te gebruiken. Deze twee toestanden corresponderen met een bit.

In het geval van ferromagneten is de spontane magnetisatie de grootheid die omgeschakeld wordt. De spontane magnetisatie ontstaat door de ordening van de magnetische dipolen die gerelateerd zijn aan de spin van de elektronen van het materiaal. Er is een interactie tussen de spins van de elektronen; de zogenaamde exchange interaction, die ontstaat uit de Coulomb interactie en de kwantummechanica. In ferromagneten staan de spins dezelfde kant op en dit veroorzaakt een netto magnetisch moment. In antiferromagneten hebben naast elkaar gelegen spins een tegengestelde richting of vormen complexere structuren met een totaal magnetisch moment van nul. De spontane magnetisatie van de ferromagneten kan omgekeerd worden door een magnetisch veld toe te passen. De huidige technologie gebruikt ferromagnetische stoffen die onderverdeeld zijn in een reeks gebieden op sub-micrometerschaal om informatie op te slaan. De magnetisatie van deze gebieden kan dienen om een bit te bewaren dat door een magnetisch veld omgeschakeld kan worden.

In ferroelektrische materialen is er een spontane elektrische polarisatie. Deze polarisatie wordt veroorzaakt door een verplaatsing van de positieve en negatieve ionen en de polarisatie van de elektronwolk. Een elektrisch veld koppelt aan de elektrische polarisatie, waarvan de richting kan veranderen. Deze stoffen zijn ook toe te passen in geheugens, zoals bijvoorbeeld in FeRAM (ferroelectric random memories).

De coëxistentie en wisselwerking van magnetisme en ferroelektriciteit is uitermate wenselijk voor technologische doeleinden. Dit maakt het bijvoorbeeld mogelijk om magneto-elektrische geheugens (MERAM) te ontwerpen en te bouwen met willekeurige toegang, waarbij magnetische bits worden geschreven door een spanningsverschil in plaats van een magnetisch veld. Dit zou een technologische doorbraak betekenen omdat voor het gebruik van magnetische velden elektrische stroom nodig is, waarbij energie wordt gedissipeerd.

Een groot nadeel bij dit samenspel is dat ferroelektriciteit en magnetisme normaliter onverenigbaar zijn. De verplaatsing in het kristal van elektrische lading wordt namelijk doorgaans pas mogelijk als de ionen van het materiaal geen netto spin hebben. Gelukkig kan in sommige materialen ferroelektriciteit verschijnen als secundair effect.

Dit effect vindt plaats in de zogenaamde magnetische ferroelektrische materialen. Hier is het de structuur van de spinrangschikking zelf die voor het breken van de inversiesymmetrie zorgt; een proces dat ten grondslag ligt aan de elektrische polarisatie. Echter, deze coëxistentie garandeert het bestaan van koppeling tussen magnetisatie en elektrische polarisatie niet. Dit fenomeen vindt plaats in magneto-elektrische materialen, waar een elektrisch veld de magnetisatie kan sturen (of andersom). Deze twee groepen van materialen kennen een overlap, maar verschillen ook. Dit betekent dat niet alle magneto-elektrische stoffen magnetisch ferroelektrisch zijn en omgekeerd. Het onderwerp van dit proefschrift is de theoretische analyse van stoffen met deze eigenschappen.

Een bijzondere klasse van magnetische ferroelektrische materialen zijn magneten met cycloïdische spiraal-achtige spinorde. In deze stoffen draaien de spins van naburige magnetische ionen om een as die loodrecht staat op de propagatierichting van de spiraal. Deze rangschikking van de spins breekt de inversie symmetrie en leidt tot elelektrische polarisatie. De richting van deze polarisatie wordt gegeven door de draaias van de spinrotatie. De verandering van de rotatierichting, van met de klok mee naar tegen de klok in, keert de elektrische polarisatie om. Het derde hoofdstuk van dit proefschrift gaat over de analyse van het omkeren van de rotaties van de spin, en daarmee van de elektrische polarisatie, door een rotatie van het toegepaste magnetische veld. Hier wordt aangetoond dat de efficiëntie van dit proces afhankelijk is van de veldsterkte en de wijze waarop het veld omkeert.

Conische spiraal-achtige spinorde heeft zowel een uniforme als een spiraal-achtige component. Hierdoor komen uit deze magnetische rangschikking ferromagnetisme en ferroelektriciteit voort. Het uniforme deel van de conische spiraal-achtige spins veroorzaakt magnetisatie terwijl het draaiende deel elektrische polarisatie veroorzaakt. Deze twee grootheden zijn niet gekoppeld in een enkel magnetisatiedomein. Echter, in echte stoffen bestaan domeinen met tegenovergestelde magnetisatie naast elkaar. In het tweede hoofdstuk van dit proefschrift wordt aangetoond dat magnetisatie en elektrische polarisatie aan elkaar zijn gekoppeld op de grens tussen twee domeinen met tegenovergestelde magnetisatie.

De oorsprong van ferroelektriciteit in de cycloïdische spiraal-achtige spinorde is het draaien van de spins in het rooster. Een dergelijke rotatie vindt ook plaats op de grens die twee normale ferromagnetische domeinen scheidt. Een periodieke reeks

van domeinen met tegenovergestelde magnetisatie is stabiel bij kamertemperatuur in de zogenaamde "stripe phase" van ferromagnetische "thin films". In dit proefschrift wordt ook de elektrische polarisatie behandeld die ontstaat door de grens die twee domeinen scheidt. Er wordt aangetoond dat naburige domeingrenzen tegenovergestelde polarisatie genereren. Daarnaast wordt het effect van een elektrisch veld dat loodrecht is toegepast op de "film", behandeld. Een veld met voldoende sterkte lijnt de elektrische polarisatie uit die voortkomt uit alle domeingrenzen; dit resulteert in een grote versterking van de diëlektrische constante van de "film" zelf.

In bepaalde materialen is het magneto-elektrische effect lineair. Dit betekent dat de elektrische polarisatie evenredig groeit met het toegepaste magnetische veld. Het eerste materiaal waarbij dit effect voorspeld en vervolgens gemeten werd, is Cr_2O_3. In dit proefschrift wordt de microscopische origine van het lineaire magneto-elektrische effect in deze stoffen opgehelderd. De afhankelijkheid van de temperatuur van de magneto-elektrische susceptibiliteit wordt berekend door de koppeling te bekijken tussen de Heisenberg spin exchange sterkte en de elektrische polarisatie. De overeenstemming van de voorspellingen en de experimentele resultaten bewijzen dat dit soort koppelingen de grootste bijdrage levert aan het magneto-elektrische effect in Cr_2O_3.

De koppeling van spins met elektrische polarisatie veroorzaakt de vermenging van magnetische excitatie met trillingen van het rooster. Magnonen zijn kleine collectieve deformaties van de spins ten opzichte van de magnetische ordening. Fononen zijn collectieve trillingen van de ionen in het kristal. De magneto-elektrische koppeling vermengt magnonen met polaire fononen en resulteert in de zogeheten elektromagnonen, dat wil zeggen, magnonen die opgewekt kunnen worden door de elektrische veldcomponent van het licht. Dit gebeurt bijvoorbeeld in de non-collineaire incommensurat magnetische toestanden van YMn_2O_5. Voor deze complexe spintoestanden worden de eigenschappen van magnonen en elektromagnonen bestudeerd, met als resultaat de overeenstemming tussen inelastische neutronverstrooiing en optische metingen.

Concluderend, in dit proefschift wordt de studie van eigenschappen van materialen waarbij elektrische polarisatie wordt gegenereerd door magnetisatie gepresenteerd. Belicht worden onder andere de sterkste microscopische interactie lineaire magneto-elektrische effecten in sommige collineaire antiferromagneten genereert, mechanismen die de magnetische besturing van elektrische polarisatie in cycloïdische spirale magneten toestaan en het ontstaan van excitatie van elektromagnonen in non collineaire magneten met complexe magnetische ordeningen. De gepresenteerde resultaten dragen bij aan het bloeiende onderzoek naar stoffen waarbij elektrische polarisatie is gekoppeld aan magnetisme.

9

Acknowledgments

First of all I would like to express my gratitude to my first promotor Prof. Maxim Mostovoy. It would not have been possible to write this thesis and to perform the research work presented here without his help, his suggestions, his bright ideas and his corrections. Maxim, I am deeply indebted to you for all the efforts you had put to teach me the way to become a good physicist. I sincerely hope that there will be a point in my life where I will be able to prove that those efforts were not in vain. Moreover, I would like to thank you for the great of opportunities you gave me, for your patience and for your suggestions on personal matters.
I am also grateful to my second promotor Prof. Jasper Knoester. Jasper, thanks a lot for your support and encouragement. I strongly benefited from your comments and suggestions during group meetings and private discussions. The social events that you organized for our group made me feel at home.
I am thankful to the members of the reading committee Prof. Jeroen van den Brink, Prof. Naoto Nagaosa and Prof. Thomas Palstra for the time they spent on reading my thesis and for their corrections and comments.
The research presented in thesis deeply benefited of the experience and the knowledge of a number of collaborators. Among those I would like to express my gratitude to Prof. T. Kaplan, Prof. N. Spaldin, Dr. K. Delaney, Dr. J. Kim and Prof. S.-H. Lee.
During these years spent in the "Center for Theoretical Physics" I had the pleasure of sharing the office with three wonderful persons, who constantly helped me. Albert, Siebren and Sergey thanks a lot for everything. The numerous discussions together with my colleagues Sergey and Michiel, as well as their suggestions and our collaborations, strongly contributed to the development of this thesis. Sergey, thanks also for being my paranymph.
Discussions on my research topic with researchers of the Zernike Institute for Advanced Materials were very beneficial for my work and stimulated my curiosity. For

this, I would like to thank Prof. Palstra, Prof. Noeda, Umut, Johan, Christophe, Nandang and Anne.
There is a number of people that helped me in various ways during the rushing time precedent to the printing of this thesis. For this I sincerely thank: Thomas, Arend, Marrit, Olexander, Leonieke, Fabio, Carmen, Dennis and Frank, I would like to specially thank Marrit who also corrected the grammar of some of the chapters and continuously gave me moral support.
I am thankful to the present and former members of the condensed matter theory group for the useful scientific discussions and for the wonderful time spent together. Anna, Alina, Andrei, Bas, Bernhard, Bintoro, Chungwen, Christi, Dirk-Jan, Elena, Kasper, Niels, Javier, Joost, Roel, Rudolph, Santanu, Sander and Victor thanks a lot. I am also thankful to the secretaries of our department.

There is also a large number people who gave an indirect contribution to the development of this thesis. Although their help was on non-scientific-related aspects of my Ph.D time in Groningen, their support, their love and their friendship was extremely precious to me.
I thank my mother, to whom this thesis is dedicated, for her everlasting love. I thank my father for his continuous support and for giving me strength and motivation.
I would like to thank all my relatives and friends that have been close to me during the extremely hard period I had in the third year of my PhD. Particularly, I would like to express my deepest gratitude to my cousins Elisa and Emanuela, my uncle Luigi, their families and the nuns of the "Monastero Serve di Maria". Cisco, Pedo, Joseph (Yoghi) and Miriam I would like also to thank you for having been so close to me during that period.
I would like to thank Teresa for taking good care of my father and for her support.
My thanks also go to my friends from Bologna. My old housemates Andrea, Laura (Biondina), Ivana, David (Giancarlí), Emiliano, Antonio and my University mate Paolo continued to support me despite the large distance. Coggí, I also would like to thank you for being my paranymph.
Many people contributed to make this time in Groningen a wonderful experience. Fabio, Giulio, Tano (I recommend to go to his office if you get stuck with writing), Jesus, Gregorio (you will never learn), Alessio - thanks for the countless number of beers, the incredible adventures and the fun we had together. The same holds for "De Pintelier" and "L' Amigo" crew. Tatiana (thanks also for the parties), Nuria (thanks also for the "skeleton" jokes), Tom, Santi, Maria Jose, Maria Jesus, Manolo, Mauricio, Emi, Daniele, Filippo, Dorota, Pablo, Johanne, Alba, Clelia, Roberto, Luca, Kostas, Christophe, Katarina, Sebastiano, Primoz, Siva, Gaston and Julio - thanks to all of you for the great time. My previous and current housemates deserve a special thanks for their patience (especially on my continuous delays on washing the dishes) and their kindness. Johanne (a.k.a. Penny), Nop, Anthony, Lachlan, Eva - it was great living with you. The same holds for the Blekerslaan crew with whom I shared so many things during the first year in Groningen. I would like to thank Silvia, Ruth, Laura for all the Italian and international dinners at their place. Thanks also to the people that in various way entered in my Groningen life. These include: Sophie, Jennifer, Clelia,

Jorn, Anne, Yvonne, Katharina, Laura, Elena, Bruno, Giuseppe, Johan (I enjoyed our chess games a lot) and many others.
I also would like to thank all my friends from "Cooperativa Il Biancospino". The holiday with them extremely enriched my perspective on life.
As last but not least, I would like to thank the other friends from Urbino who where not mentioned above. Claudia, Angelantonio (Micio), Paola, Vittorio, Vale, Marco, Gabriela, Martina, Francesca - thanks a lot for your friendship.
I am sure, that, no matter how much time I will spend writing these acknowledgments, I will forget to mention somebody. I apologize to these people and I would like them to know that my gratitude goes beyond my failing memory.

Andrea, Groningen, 2010